DISSERTATIONES
PHYSICAE
UNIVERSITATIS
TARTUENSIS
132

NICO BENINCASA

Phase transitions and gravitational waves in models of dark matter

DISSERTATIONES PHYSICAE UNIVERSITATIS TARTUENSIS

132

DISSERTATIONES PHYSICAE UNIVERSITATIS TARTUENSIS

132

NICO BENINCASA

Phase transitions and gravitational waves in models of dark matter

UNIVERSITY OF TARTU
Press

This study was carried out at the National Institute of Chemical Physics and Biophysics, Tallinn, and the University of Tartu, Estonia.

The dissertation was admitted on September 13, 2023 in partial fulfilment of the requirements for the degree of Doctor of Philosophy in physics, and was allowed for defence by the Council of the Institute of Physics, University of Tartu.

Supervisors:	Dr. Kristjan Kannike, National Institute of Chemical Physics and Biophysics, Tallinn, Estonia
	Prof. Abdelhak Djouadi, University of Granada, Granada, Spain
	Assoc. Prof. Margus Saal, University of Tartu, Tartu, Estonia
Opponent:	Dr. Bogumiła Świeżewska, University of Warsaw, Warsaw, Poland
Defence:	October 11, 2023, University of Tartu, Estonia

ISSN 1406-0647 (print)
ISBN 978-9916-27-334-0 (print)
ISSN 2806-2523 (pdf)
ISBN 978-9916-27-335-7 (pdf)

University of Tartu Press
www.tyk.ee

Contents

List of original publications

This results of this thesis are compiled in the three following research publications:

I. T. Alanne, N. Benincasa, M. Heikinheimo, K. Kannike, V. Keus, N. Koivunen and K. Tuominen, "Pseudo-Goldstone dark matter: gravitational waves and direct-detection blind spots", JHEP **10** (2020) 080 [arXiv:2008.09605 [hep-ph]].

II. N. Benincasa, L. Delle Rose, K. Kannike and L. Marzola, "Multi-step phase transitions and gravitational waves in the inert doublet model", JCAP **12** (2022) 025 [arXiv:2205.06669 [hep-ph]].

III. G. Arcadi, N. Benincasa, A. Djouadi and K. Kannike, "Two-Higgs-doublet-plus-pseudoscalar model: Collider, dark matter, and gravitational wave signals", Phys. Rev. D **108** (2023) 055010 [arXiv:2212.14788 [hep-ph]].

Author's contribution

In publication I, the dissertant computed the perturbative unitarity constraints, wrote the corresponding part and cross-checked, with his own code, the results about phase transitions.

In publication II, the dissertant performed almost all the computations and cross-checked the rest. He also wrote the part about phase transitions.

In publication III, the dissertant performed all the computations related to phase transitions and wrote the corresponding part.

Acknowledgments

I would like to deeply express my gratitude for my thesis supervisor, Kristjan Kannike, who was constantly available and for his invaluable guidance for the whole PhD. I also thank my co-supervisors Abdelhak Djouadi and Margus Saal. A big thanks to Kristjan Kannike, Kristjan Müürsepp and Ville Vaskonen, whose proofreading and constructive comments about this manuscript necessarily improved its quality.

I would like to thank Kristjan Kannike, Luca Marzola, Niko Koivunen, Kristjan Müürsepp and Ruiwen Ouyang for helpful and interesting discussions. I more generally thank my colleagues of the theoretical particle physics research group for creating this wonderful work atmosphere. I will certainly miss it.

An eternal thanks to my family, without whom, nothing of this would have been possible. I also thank my friends in Tallinn for having made this experience even more enjoyable. Finally, a warm thank-you to Mégane, for the moral support and the joyful moments spent together throughout this adventure.

This work was supported by the Estonian Research Council grant PRG-434.

Chapter 1

Introduction

In Nature, there exist four known fundamental interactions. The electromagnetic interaction acts on charged particles and is, for instance, responsible for binding electrons to nucleus to form atoms. The weak interaction is responsible for the radioactive beta decay of atoms. The next one, the strong interaction, binds quarks together into nucleons. Finally, the gravitational interaction occurs between entities with non-vanishing mass or energy. While the latter interaction is very well described by General Relativity through the Einstein equation, the former three interactions are successfully described by the Standard Model (SM) of particle physics. This theory predicts the existence of the Higgs boson, a crucial particle giving mass to particles it interacts with, through the Brout-Englert-Higgs (BEH) mechanism. The discovery of this particle in 2012 at the LHC by the ATLAS [1] and CMS [2] experiment actually completed the set of particles predicted in the Standard Model.

Despite being a successful theory of the microscopic world, the Standard Model does not provide a full description of Nature, even by restricting it to three fundamental interactions by excluding gravity. Indeed, the Standard Model does not explain the origin of the masses of neutrinos, which have been confirmed through the observation of their oscillation [3]. Moreover, it does not predict the existence of dark matter (DM), a hypothetical matter composing the greater part of the matter content in the Universe. For sure, this cannot be neglected.

One believes DM to exist since it provides solutions to the otherwise unexplained observed phenomena, such as the unobserved Keplerian fall-off in galaxy rotation curves, the formation of the large-scale structures of today, etc. The Standard Model of Cosmology, the ΛCDM model, where Λ refers to the cosmological constant, while CDM stands for cold dark matter, is based on the Friedmann-Lemaître-Robertson-Walker (FLRW) metric. Within the framework of this model, it is observed that the homogeneous and isotropic Universe is almost flat, with an energy content made of 68% of dark energy, 27% of (cold) dark matter, while ordinary matter, made of SM particles, constitutes the remaining 5% [4].

So far, plenty of models have attempted to describe dark-matter features by predicting a potential detection signal. When confronted with experimental observations, the rejected models actually put constraints on dark matter: one learns more about which features DM cannot possess. There are different ways to probe this mysterious matter. It can be potentially detected through direct-detection experiments, based on DM scattering processes with atomic nuclei, or through indirect-detection experiments, where the process of interest is DM annihilation into SM particles in cosmic rays. Additionally, one can try to produce DM particles at collider. Note that these methods implicitly consider DM as a (new exotic) particle.

While the predictions of gravitational waves (GW) by General Relativity and their discovery by LIGO in 2015 [5, 6] once more confirmed the validity of Einstein's theory, they also opened a new channel to investigate dark matter. Indeed, it has been shown that if a cosmic phase transition (PT) of the first order occurred in the early Universe, one should be able to observe a stochastic gravitational-wave background today [7, 8].

The phase transition which is the object of this thesis happened during the electroweak (EW) spontaneous symmetry breaking (SSB), when the Brout-Englert-Higgs mechanism gave mass to known particles. It is a well known fact that in the Standard Model, this phase transition is actually a crossover [9], thus generating no stochastic gravitational-wave background signal. The idea of this thesis is to consider beyond-Standard-Model (BSM) theories in which additional scalar fields induce a first-order phase transition (FOPT) at the EW scale, instead of the SM crossover. The resulting signal from this generated stochastic gravitational-wave background could then be probed by future space-based GW detectors, such as LISA [10].

The structure of the thesis is the following. In Chapter 2, we review the concept of spontaneous symmetry breaking in the Standard Model and the need to consider BSM theories to, for instance, explain dark matter, which is reviewed in Chapter 3. In Chapter 4, we derive the one-loop thermally corrected effective potential needed for the study of cosmic phase transitions in the early Universe (Chapter 5) and the computation of the signal from the induced stochastic gravitational-wave background (Chapter 6). A summary is then provided both in English (Chapter 7) and in Estonian (Chapter 8). Finally, the publications, which contains the results of this thesis, can be found in the appendix.

Chapter 2

Spontaneous symmetry breaking in the Standard Model

The Standard Model aims to describe all known matter (made of leptons and quarks), interactions (mediated by gauge bosons) and the Higgs boson. Its Lagrangian density $\mathcal{L}_{\text{SM}}$ is invariant under transformations in the non-abelian $SU(3)_c \otimes SU(2)_L \otimes U(1)_Y$ gauge group, where $SU(3)_c$ is the gauge group of the strong interaction, while $SU(2)_L \otimes U(1)_Y$ is the gauge group corresponding to the electroweak symmetry. The $SU(3)_c$ group gives rise to eight gauge bosons G^a_μ $(a = 1 \dots 8)$, the gluons, and the $SU(2)_L \otimes U(1)_Y$ group provides three weak gauge bosons W^i_μ $(i = 1 \dots 3)$, as well as one hypercharge gauge boson B_μ. Since the symmetry of the strong interaction is not broken, we will only focus on the electroweak group $SU(2)_L \otimes U(1)_Y$ in the rest of this chapter.

As indicated by the subscript L of the $SU(2)_L$ group, weak gauge bosons W^i_μ only interact with left-handed particles (and right-handed anti-particles). This allows us to gather left-handed leptons ν^ℓ_L and e^ℓ_L into one doublet L^ℓ_L for each generation $(\ell \in \{e, \mu, \tau\})$. Likewise for left-handed quarks, u^q_L and d^q_L are embedded into one doublet Q^q_L for each generation ($q \in \{u, c, t\}$ for u^q_L and $q \in \{d, s, b\}$ for d^q_L). The discovery of the Higgs boson at the LHC in 2012 completed the Standard Model of particle physics. The Higgs field is described by a doublet with an upper part electrically charged, while the lower part is neutral. The set of particles described by the Standard Model is summarised in the Table 2.1.

In the Standard Model, particles are massless as mass terms in $\mathcal{L}_{\text{SM}}$ would violate the SM gauge symmetry. A dynamical way to generate mass of particles, without explicitely breaking the SM gauge symmetry is given via the Brout-Englert-Higgs mechanism, which is reviewed in Section 2.2.

2.1 Spontaneous breaking of global symmetries: an Abelian case

When a physical system possesses several degenerate minima or ground states, then during the phase transition from the initial state, the system arbitrarily chooses one direction, one of the degenerate ground states, as the final state. Spontaneous symmetry breaking occurs because the chosen

	$SU(3)_c$	$SU(2)_L$	T_3	$Y/2$	$Q = T_3 + Y/2$
Matter fields					
$L_L^\ell = \begin{pmatrix} \nu_L^\ell \\ e_L^\ell \end{pmatrix}$	1	2	$\begin{pmatrix} 1/2 \\ -1/2 \end{pmatrix}$	$-1/2$	$\begin{pmatrix} 0 \\ 1 \end{pmatrix}$
e_R^ℓ	1	1	0	-1	-1
$Q_L^q = \begin{pmatrix} u_L^q \\ d_L^q \end{pmatrix}$	3	2	$\begin{pmatrix} 1/2 \\ -1/2 \end{pmatrix}$	1/6	$\begin{pmatrix} 2/3 \\ -1/3 \end{pmatrix}$
u_R^q	3	1	0	2/3	2/3
d_R^q	3	1	0	-1/3	-1/3
Higgs field					
$H = \begin{pmatrix} G^+ \\ \frac{h+v+iG}{\sqrt{2}} \end{pmatrix}$	1	2	$\begin{pmatrix} 1/2 \\ -1/2 \end{pmatrix}$	1/2	$\begin{pmatrix} 1 \\ 0 \end{pmatrix}$

	Gauge group
Gauge fields	
G_μ^a, $a = 1 \dots 8$	$SU(3)_c$
W_μ^i, $i = 1 \dots 3$	$SU(2)_L$
B_μ	$U(1)_Y$

Table 2.1: Particle content of the Standard Model and their associated quantum numbers and charges.

ground state of the theory does not satisfy the symmetry of the Lagrangian. Although one mentions *breaking*, it would be more appropriate to talk about *hidden* symmetry because the Lagrangian never breaks that symmetry in any manner whatsoever via this mechanism; it is only hidden because of the way in which one rewrites the Lagrangian density.

The following is based on the excellent introduction to quantum field theory [11]. Let us first exemplify SSB with a simple Abelian case. One considers a complex scalar field ϕ, the Lagrangian density of which is

$$\mathcal{L}_\phi = |\partial_\mu \phi|^2 + m^2|\phi|^2 - \lambda|\phi|^4 = |\partial_\mu \phi|^2 - V(\phi). \tag{2.1}$$

This Lagrangian density is invariant under the global $U(1)$ transformation $\phi(x) \to e^{i\alpha}\phi(x)$. For the potential $V(\phi) = -m^2|\phi|^2 + \lambda|\phi|^4$ to be bounded from below, a positive λ is required. Then one has two cases depending on the sign of μ^2. If μ^2 is positive, then the vacuum expectation value[1] (VEV) that minimises the potential is unique: $\langle\Omega|\phi|\Omega\rangle \equiv \langle\phi\rangle = 0$, with $|\Omega\rangle$ the vacuum state of the theory. In this situation, one can safely apply perturbation theory around this stable minimum and no spontaneous symmetry breaking occurs. On the other hand, for the case $\mu^2 < 0$, the potential shapes like a Mexican hat. In this configuration the extremum at the origin is this time a maximum, and is thus unstable. Perturbation around this extremum would result in tachyonic modes with negative squared mass, making the theory

---

[1] No VEV is allowed for spinors or vector fields if one wants to preserve Lorentz invariance. Moreover, the VEV should be spatially constant if one requires it to be invariant under translation [12].

non-causal. The other extrema, which actually minimise the potential, are given by the condition $|\phi|^2 = m^2/(2\lambda)$. By the $U(1)$ symmetry, one has an infinite set of equivalent $\phi = m/\sqrt{2\lambda}e^{i\theta}$, with $\theta \in [0, 2\pi[$, that minimises the potential. It is convenient here to choose $\theta = 0$, so that the value of the field which minimises the potential is along the real direction.

One can then look at the theory around the minimum $\langle\phi\rangle = m/\sqrt{2\lambda} \equiv v$. One does it by expanding the field around the ground state v: $\phi(x) = v/\sqrt{2} + \tilde{\phi}(x)$, with the complex scalar field $\tilde{\phi}(x)$ which can be expressed in terms of real fields as $\tilde{\phi}(x) = (\sigma(x) + i\pi(x))/\sqrt{2}$. Another convenient parametrisation is when $\pi(x)$ is a phase:[2]

$$\phi(x) = e^{i\frac{\pi(x)}{F_\pi}} \frac{(v + \sigma(x))}{\sqrt{2}}. \tag{2.2}$$

Now if one rewrites the Lagrangian density (2.1) in terms of this new parametrisation, one obtains

$$\begin{aligned}
\mathcal{L}_\phi &= \frac{1}{2}(\partial_\mu\sigma)^2 + \frac{1}{F_\pi^2}\left(\frac{\sigma+v}{\sqrt{2}}\right)^2(\partial_\mu\pi)^2 + \frac{m^2}{2}(\sigma+v)^2 - \frac{\lambda}{4}(\sigma+v)^4 \\
&= \frac{1}{2}(\partial_\mu\sigma)^2 - \frac{1}{2}\left(\frac{m^2}{2}\right)\sigma^2 + \frac{1}{2}(\partial_\mu\pi)^2 + \frac{\sigma}{v}\left(1+\frac{\sigma}{2v}\right)(\partial_\mu\pi)^2 \\
&\quad - \left(\frac{\lambda}{4}\sigma^4 + \lambda v\sigma^3 + \frac{m^2 v}{2}\sigma - \frac{3m^4}{16\lambda}\right),
\end{aligned} \tag{2.3}$$

where in the second equality one chose $F_\pi = v$ to have the kinetic term $(\partial_\mu\pi)^2$ canonically normalised. This expression of $\mathcal{L}_\phi$ clearly shows that by taking the second derivative with respect to the fields, the field $\sigma(x)$ possesses a mass $m/\sqrt{2}$, while the field $\pi(x)$ is massless. The particle associated to this massless field is a Goldstone boson. An excitation at the minimum $\langle\phi\rangle$ along the radial direction leads to a positive second derivative in that same direction, and thus to a positive squared mass for $\sigma(x)$, while an excitation along the perpendicular (flat) direction yields a vanishing second derivative for $\pi(x)$, which is thus massless. This property of Goldstone bosons is due the fact that it respects a shift symmetry $\pi(x) \to \pi(x) + F_\pi\alpha$. When looking at the parametrisation in Eq. (2.2), one can note that this shift symmetry is actually equivalent to the global $U(1)$ transformation $\phi(x) \to e^{i\alpha}\phi(x)$ under which $\mathcal{L}_\phi$ is invariant: remember that $\mathcal{L}_\phi$ does not break this symmetry, only the ground state does. A mass term for $\pi(x)$ would break the shift symmetry and thus the $U(1)$ symmetry explains why such a mass term is forbidden for Goldstone fields. Another interesting property of Goldstone bosons that can be seen in Eq. (2.3) is that Goldstone interaction terms always involve the derivative of $\pi(x)$, which means that in the momentum space Goldstone interaction are proportional to four-momentum. This feature peculiar to Goldstone bosons plays an important role in direct-detection experiments, where tree-level processes of Goldstone boson scattering off a nucleus involve a vertex proportional to the momentum transfer and are thus suppressed in the limit of vanishing

---

[2] By expanding $e^{i\pi(x)/F_\pi}$ in terms of powers of $\pi(x)$ and keeping only the independent terms and the ones linear in the dynamical fields $\sigma(x)$ and $\pi(x)$ (since one considers small perturbations), one recovers the parametrisation $\phi(x) = (v + \sigma(x) + i\pi(x))/\sqrt{2}$, for $F_\pi = v$.

momentum transfer.[3] Direct detection will be explored in more details in Section 3.3.

In general, one obtains as many Goldstone bosons as there are generators of a continuous global symmetry group broken by the ground state. This fact is a consequence of the Goldstone theorem, which states the emergence of these massless Goldstone bosons each time a global symmetry is spontaneously broken. Following the Peskin & Schroeder book [14], we below provide a simple proof of this theorem for classical field theories.

Let us consider a Lagrangian density depending on N fields: $\mathcal{L} =$ kinetic terms $- V(\vec{\phi})$, with $\vec{\phi} = (\phi_1, \ldots, \phi_N)^T$. Consider then a VEV $\vec{\phi}_0$ which minimises the corresponding Hamiltonian density and thus V as the VEV $\vec{\phi}_0$ is constant: $\vec{\nabla} V(\vec{\phi})\Big|_{\vec{\phi}_0} = 0$, with $\vec{\nabla} \equiv \vec{\nabla}_{\vec{\phi}}$ a gradient with respect to the field $\vec{\phi}$.

Let us now suppose that $\mathcal{L}$ is invariant under the global *continuous* symmetry transformation $\vec{\phi} \to \vec{\phi} + \alpha\vec{\Delta}(\phi_1, \ldots, \phi_N)$, with α an infinitesimal parameter and $\vec{\Delta}$ a vector whose components are functions of $\phi_1, \ldots, \phi_N$. This form of the transformation is general and is due to the fact the α can be taken infinitesimally small, by definition of a continuous symmetry. As $\mathcal{L}$ is invariant under the above symmetry transformation, one has $\mathcal{L}(\vec{\phi}) = \mathcal{L}(\vec{\phi} + \alpha\vec{\Delta}(\phi_1, \ldots, \phi_N))$, which is equivalent to $\alpha\vec{\Delta}(\phi_1, \ldots, \phi_N)^T \cdot \vec{\nabla}\mathcal{L}(\vec{\phi}) = 0$, by definition of the derivative (which requires α to be infinitely small); considering continuous symmetries is thus crucial. Taking the gradient of the latter expression and evaluating the resulting expression in the vacuum $\vec{\phi}_0$, where one has $\mathcal{L}(\vec{\phi}_0) = -V(\vec{\phi}_0)$, one obtains

$$\begin{aligned} 0 &= \left[\vec{\nabla}\left(\vec{\Delta}^T \cdot \vec{\nabla} V(\vec{\phi})\right)\right]\Big|_{\vec{\phi}_0} \\ &= \left[\left(\partial_{\phi_j}\Delta_i\right)\partial_{\phi_i} V\right)\Big|_{\vec{\phi}_0} + \left[\Delta_i \partial_{\phi_j}\partial_{\phi_i} V\right]\Big|_{\vec{\phi}_0} \\ &= M^2(\vec{\phi}_0) \cdot \vec{\Delta}(\phi_1^0, \ldots, \phi_N^0), \end{aligned} \tag{2.4}$$

where the first term in the second line is zero as $\vec{\nabla} V$ vanishes at the minimum and where $(M^2)_{ij} \equiv \partial_{\phi_j}\partial_{\phi_i} V$ is the coefficient of the quadratic term in the expansion of V around the minimum $\vec{\phi}_0$. $M^2(\vec{\phi})$ is the mass matrix, a symmetric matrix, whose eigenvalues are the squared masses of the fields. Note that the eigenvalues of M^2, the Hessian matrix of the potential, evaluated at $\vec{\phi} = \vec{\phi}_0$ cannot be negative by definition, as $\vec{\phi}_0$ minimises the potential. If $\vec{\Delta}(\phi_1^0, \ldots, \phi_N^0) = 0$, that is if the ground state $\vec{\phi}_0$ respects the symmetry, then Eq. (2.4) is trivially satisfied. On the other hand, if the ground state breaks that symmetry, then the relation (2.4) shows that $\vec{\Delta}(\phi_1^0, \ldots, \phi_N^0)$ is a non-zero eigenvector associated with a zero eigenvalue, which means that the theory of the underlying Lagrangian density $\mathcal{L}$ contains a massless particle: the Goldstone boson. Therefore one can see that for any number of non-zero eigenvectors $\vec{\Delta}(\phi_1^0, \ldots, \phi_N^0)$ of the mass matrix $M^2(\vec{\phi}_0)$, thus for any number of global continuous symmetries broken by the ground state $\vec{\phi}_0$, one obtains as many as massless Goldstone bosons.

To conclude this part about spontaneous symmetry breaking of global continuous symmetries, let us note that if, in addition to be broken by

---

[3] This limit, commonly used in direct-detection processes, is acceptable only when the momentum transfer is negligible compared to the mass in the propagator [13].

the ground state, the symmetry is also explicity broken (by a term in the Lagrangian density), then the would-be massless Goldstone boson that one would obtain without this explicit symmetry breaking, will actually acquire a mass proportional to the coupling of this explicit breaking term; one then talks about pseudo-Goldstone bosons.

2.2 Brout-Englert-Higgs mechanism

Let us now consider the spontaneous breaking of (local) gauge symmetries through the so-called Brout-Englert-Higgs mechanism. We will show that, in that case, Goldstone bosons are not physical particles. They are absent because they are *eaten* by the gauge bosons associated to the spontaneously broken gauge symmetry, giving them a mass. Consider for instance the Glashow-Weinberg-Salam theory, which aims to unify electromagnetic and weak interaction. The gauge symmetry associated to this electroweak interaction is $SU(2)_L \otimes U(1)_Y$. The three generators of the $SU(2)_L$ group are $T_i \equiv \sigma_i/2$, with σ_i ($i \in \{1,2,3\}$) the Pauli matrices, while the one of $U(1)_Y$ is the weak hypercharge $Y/2$. Therefore this theory contains four (massless) gauge bosons. Observations show that in nature there are three massive gauge bosons W^+, W^-, Z, mediating the weak interaction, and one massless gauge boson, the photon γ, being the mediator of the electromagnetic interaction. To give mass to three of the four massless gauge bosons, let us consider the Higgs doublet $\phi(x)$, a complex scalar field. Its VEV should break three out of four generators and break the non-Abelian group $SU(2)_L \otimes U(1)_Y$ down to $U(1)_{\text{em}}$, the electromagnetic group, whose generator is $Q = T_3 + Y/2$. It is crucial that the VEV of $\phi(x)$ leaves $U(1)_{\text{em}}$ unbroken, as otherwise the electric charge would not be conserved and the photon would become massive, in clear contradiction with observations.

Under the electroweak gauge group, the Higgs doublet transforms as [14]

$$\phi(x) \to e^{i\left(\alpha_j(x)\frac{\sigma_j}{2} + \beta(x)\frac{Y}{2}\right)}\phi(x). \tag{2.5}$$

The most general gauge-invariant renormalisable Higgs potential associated to that field is

$$V(\phi) = -\mu^2|\phi|^2 + \lambda|\phi|^4. \tag{2.6}$$

A non-trivial value for the ground state satisfies $|\langle\phi\rangle| = \mu/\sqrt{2\lambda} \equiv v$. Then similarly to the previous case, one can express the field $\phi(x)$, expanded around its VEV, with a radial part and a phase containing the Goldstone bosons π_j:

$$\phi(x) = e^{i\frac{\pi_j(x)}{F_\pi}\frac{\sigma_j}{2}}\begin{pmatrix} 0 \\ \frac{v+h(x)}{\sqrt{2}} \end{pmatrix}, \tag{2.7}$$

with $h(x)$, the radial excitation known as the Higgs field with the associated Higgs boson.

For what follows, it is more convenient to work in a gauge which removes the phase in Eq. (2.7): the unitary gauge. This requires a $SU(2)_L$ transformation with $\alpha_j(x) = -\pi_j(x)/F_\pi$ for the gauge parameters in Eq. (2.5). This gauge-fixing thus imposes a *direction* for the VEV, which in the unitary gauge is then simply expressed as

$$\langle\phi\rangle = \frac{1}{\sqrt{2}}\begin{pmatrix}0\\ v\end{pmatrix}, \tag{2.8}$$

irrespective of the value of $\beta(x)$. Does this VEV break $SU(2)_L \otimes U(1)_Y$ to nothing? One hopes not, because one of the four gauge bosons, the photon, has to remain massless. Let us see how this VEV behaves under a gauge transformation in the unitary gauge. To obtain the expression (2.8), $\alpha_i(x)$ have already been fixed. For the specific choice $\beta(x) = \alpha_3(x)$, one obtains

$$\begin{aligned}\langle\phi\rangle \to e^{i\left(\alpha_j(x)\frac{\sigma_j}{2}+\beta(x)\frac{Y}{2}\right)}\langle\phi\rangle &= e^{i(\alpha_1(x)T_1+\alpha_2(x)T_2)}e^{i\beta(x)\left(T_3+\frac{Y}{2}\right)}\frac{1}{\sqrt{2}}\begin{pmatrix}0\\ v\end{pmatrix}\\ &= e^{i(\alpha_1(x)T_1+\alpha_2(x)T_2)}\frac{1}{\sqrt{2}}\begin{pmatrix}0\\ v\end{pmatrix}\\ &= e^{i(\alpha_1(x)T_1+\alpha_2(x)T_2)}\langle\phi\rangle\\ &\neq \langle\phi\rangle,\end{aligned} \tag{2.9}$$

where the second equality holds for $Y = 1$. Therefore, given that the Higgs doublet has a weak hypercharge $Y = 1$, its VEV will still be invariant under the $U(1)_{\text{em}}$ transformation $\langle\phi\rangle \to e^{i\beta(x)Q}\langle\phi\rangle$, with $Q = T_3 + Y/2$ a linear combination of the third generator of $SU(2)_L$ and the generator of $U(1)_Y$, thus preserving the electric charge. Note that $\langle\phi\rangle$ breaks three generators: T_1, T_2 and $T_3 - Y/2$.

Since one is interested in how the gauge bosons obtain their mass, let us look this time into the scalar kinetic term of the theory: $|D_\mu\phi|^2$, with $D_\mu = \partial_\mu - ig_2W^j_\mu T^j - ig_1B_\mu Y/2$ the covariant derivative necessarily introducing the gauge bosons $W^1_\mu, W^2_\mu, W^3_\mu$ and B_μ transforming in such a way under gauge transformations that the kinetic term remains gauge-invariant. The coupling constants g_2 and g_1 are, respectively, associated with $SU(2)_L$ and $U(1)_Y$. In the unitary gauge, where Goldstone bosons are *gauged away*, the contribution to $|D_\mu\phi|^2$ from the VEV is (with $Y = 1$) given by [11]:

$$\begin{aligned}|D_\mu\phi|^2 &= \left|-\frac{i}{2}\begin{pmatrix}g_1B_\mu + g_2W^3_\mu & g_2\left(W^1_\mu - iW^2_\mu\right)\\ g_2\left(W^1_\mu + iW^2_\mu\right) & g_1B_\mu - g_2W^3_\mu\end{pmatrix}\begin{pmatrix}0\\ \frac{v}{\sqrt{2}}\end{pmatrix}\right|^2\\ &= \frac{v^2}{8}\left(g_2^2\left[(W^1_\mu)^2 + (W^2_\mu)^2\right] + \left(g_1B_\mu - g_2W^3_\mu\right)^2\right),\end{aligned} \tag{2.10}$$

where the contribution involving spacetime derivatives is zero as the VEV is constant.

One can see that the mass matrix of the gauge eigenstates W^3_μ and B_μ is not diagonal. By diagonalising it, one finds the relation $g_2\sin\theta_W = g_1\cos\theta_W$, with θ_W the mixing angle known as the Weinberg angle, and expressions for the physical eigenstates in terms of the gauge eigenstates: $Z_\mu \equiv W^3_\mu\cos\theta_W - B_\mu\sin\theta_W$ and $A_\mu \equiv W^3_\mu\sin\theta_W + B_\mu\cos\theta_W$. To represent the $W^\pm$ bosons one also defines $W^\pm_\mu = (W^1_\mu \mp iW^2_\mu)/\sqrt{2}$, which have the correct electric charge.[4] With all these field redefinitions in terms of physical

---

[4] Pay attention to the $\mp$ sign, needed so that $T^1W^1_\mu + T^2W^2_\mu = T^+W^+_\mu + T^-W^-_\mu$, with $T^\pm \equiv (T^1 \pm iT^2)/\sqrt{2}$.

eigenstates and given that the relation $g_2 \sin\theta_W = g_1 \cos\theta_W$ implies

$$\cos\theta_W = \frac{g_2}{\sqrt{g_1^2 + g_2^2}}, \quad \sin\theta_W = \frac{g_1}{\sqrt{g_1^2 + g_2^2}}, \tag{2.11}$$

one can then rewrite Eq. (2.10) as

$$|D_\mu \phi|^2 = \frac{v^2}{8}\left(g_2^2\left[(W_\mu^+)^2 + (W_\mu^-)^2\right] + (g_1^2 + g_2^2)Z_\mu^2\right). \tag{2.12}$$

This provides a mass for the $W^\pm$ boson and the Z boson, respectively expressed as

$$m_{W^\pm} = \frac{g_2}{2}v \quad \text{and} \quad m_Z = \frac{1}{2}\sqrt{g_1^2 + g_2^2}v = \frac{m_{W^\pm}}{\cos\theta_W} > m_{W^\pm}. \tag{2.13}$$

As desired, a vanishing mass for the photon is obtained, since no mass term of the form $\frac{1}{2}m_A^2 A_\mu^2$ is present in Eq. (2.12).

As a final remark, one can notice that in the case of spontaneous breaking of *gauge* symmetries the existence of Goldstones bosons is gauge-dependent, thus making them unphysical, contrary to the case of physical Goldstones bosons arising from the spontaneous breaking of *global* symmetries. In the unitary gauge, gauge bosons acquire a mass by *eating* the Goldstone bosons, and then obtain three physical polarisations, two transverse modes and one longitudinal mode. Thus in this gauge, only physical modes propagate, as the unphysical Goldstone modes are absent. The number of internal degrees of freedom is nevertheless conserved as expected, since it should not be altered by a gauge transformation. Indeed, one originally had four degrees of freedom from the Higgs doublet and two for each of the four massless gauge bosons, thus having twelve degrees of freedom in total. Likewise, in the unitary gauge, one has twelve degrees of freedom: one from the Higgs doublet three for each of the three massive gauge bosons W^+, W^-, Z and two from the massless photon.

Regarding the fermion sector, and more specifically quarks, masses are generated through Yukawa couplings of the form [11]

$$\mathcal{L}_{\text{Yukawa}} = -Y_{ij}^d \bar{Q}_i H d_R^j - Y_{ij}^u \bar{Q}_i \tilde{H} u_R^j + \text{ h.c.}, \tag{2.14}$$

where Y^d and Y^u are, respectively, the down- and up-quark 3×3 Yukawa matrices, i, j run over the three quark generations and $\tilde{H} \equiv i\sigma_2 H^*$ is defined such that it selects the upper part of the doublet Q^i. After the electroweak spontaneous symmetry breaking, it becomes

$$\mathcal{L}_{\text{Yukawa}} = -v/\sqrt{2}Y_{ij}^d \bar{d}_L^i d_R^j - v/\sqrt{2}Y_{ij}^u \bar{u}_L^i u_R^j + \text{ h.c.} \tag{2.15}$$

in the unitary gauge. Going to the mass basis by diagonalising the mass matrices $v/\sqrt{2}Y^d$ and $v/\sqrt{2}Y^u$, one then obtains

$$\mathcal{L}_{\text{Yukawa}} = -v/\sqrt{2}y_i^d \bar{D}_L^i D_R^i - v/\sqrt{2}y_i^u \bar{U}_L^i U_R^i + \text{ h.c.}, \tag{2.16}$$

with the mass eigenstates D and U. In this base the mass matrices $M^d \equiv (v/\sqrt{2})y^d$ and $M^u \equiv (v/\sqrt{2})y^u$ are diagonal. For the top quark, for instance, one then has $\mathcal{L}_{\text{Yukawa}} \supset -m_t \bar{t}_L t_R$, with $m_t = (v/\sqrt{2})y_t$.

To conclude, although the Standard Model is a successful theory in, as we have just seen, explaining the origin of the mass of particles, it is not complete, hence the necessity of considering beyond-Standard-Model theories. For example, still within the frame of mass origin, the Standard Model does not explain the mass of neutrinos, which one knows should be massive as their oscillation has been observed. Furthermore this theory is unable to explain, for instance, the genesis of the observed baryon asymmetry of the Universe, nor to predict the existence of dark matter. The review of the latter is the object of the next chapter.

Chapter 3

Dark Matter

Dark matter is the subject of extensive searches since the past few decades. In this chapter we review several observations which can find an explanation by the presence of this hypothetical matter in our Universe. We then consider how this dark matter could be thermally produced as well as how it could be detected via direct-detection experiments.

3.1 Evidence for dark matter

As a first evidence of the existence of dark matter, one can mention the 1933 study by Fritz Zwicky on the Coma cluster [15]: he applied the virial theorem to the motion of galaxies within this galaxy cluster to infer its total mass. Using this mass and considering the cluster to be composed of sun-like stars, Zwicky found that the mass-to-light ratio of this cluster was significantly larger than the solar one, thus that the total mass of this cluster was much bigger than it would be if one only considers the visible constituents (sun-like stars) to compute it. He thus showed that there is some missing (invisible) matter, called dark matter.

At the scale of galaxies, Rubin, Ford and Thonnard [16] showed that galaxy rotation curves were not behaving as expected beyond the galaxy boundaries. Let us consider a spherical distribution of radius R. The circular motion of a star in it has a tangential velocity v_t given in terms of the centripetal acceleration a_c as $v_t^2 = a_c r = G_N M(r)/r$ for gravitational interactions, with G_N the Newton constant and $M(r)$ the mass in a sphere a radius r. For $r < R$, one has $M(r) \sim r^3$ and thus $v_t \sim r$. One observes a linear dependency of the circular velocity of stars inside galaxies with the distance, as predicted. However, for distances larger than R, one expects a Keplerian fall-off $v_t \sim r^{-1/2}$, while one actually observes a rather constant trend. This suggests that galaxies are embedded in a halo of dark matter which, by its gravitational effects, prevents a Keplerian fall-off.

Returning to galaxy clusters, the gravitational-lensing study of the Bullet cluster collision [17], shows the distribution of dark matter. The mass distribution of the hot ionised intra-cluster gas (detected by X-ray emission) of both clusters clearly shows that it underwent a collision. On the contrary, the galaxy clusters (optically observed) just pass through one another as it is very unlikely that collisions between stars occur; they are thus located at a different position than the intracluster gas. Since one observes that the dark matter distribution follows theses collisionless galaxy clusters, it implies the same feature for dark matter [18]. Note that dark matter being collisionless still allows a dark-matter self-interaction as large as the strong interaction for a DM mass of $\mathcal{O}(1)$ GeV [19].

Could dark matter simply be made of baryonic matter? Timely structure formation is a strong requirement for non-baryonic dark matter, since baryonic matter by itself could not succeed to create the currently observed large-scale structures on time. Indeed, as explained in [20], until recombination, photons and baryons are tightly coupled and share the same pattern of inhomogeneities. The study of the Cosmic Microwave Background (CMB) anisotropies at recombination thus provides information on matter inhomogeneities, which clearly indicate that the density perturbations are small enough to still be in a linear regime. In that regime density fluctuations grow linearly with the scale factor of the Universe. From recombination until today, the scale factor, and thus the inhomogenities, become 1000 times larger, which is still insufficient to obtain the structures with high overdensities as one observes nowadays. However, if one adds non-baryonic dark matter in the recipe, then since it is *dark* (interacts very feebly with light), it decoupled from the photons well before recombination, thus already allowing perturbations to grow much earlier.[1] Then at recombination, baryons can fall into the deep gravitational wells, previously induced by non-baryonic dark matter. With much higher density fluctuations than it would be with only baryonic dark matter, these inhomogeneities then have time to grow enough to yield the observed highly non-linear structures.

As a cosmological evidence of non-baryonic dark matter, the latest results of the CMB analysis from the Planck mission provide $\Omega_m = 0.3153 \pm 0.0073$ and $\Omega_b h^2 = 0.02237 \pm 0.00015$, with $h \equiv H_0/100$ km^{-1}s Mpc, where $H_0 = 67.36 \pm 0.54$ km s^{-1}Mpc^{-1} is the current value of the Hubble parameter given by Planck mission [4] . The density parameter $\Omega_i \equiv \rho_i/\rho_c$ is defined as the ratio of the present energy density ρ_i to the critical density $\rho_c \equiv \rho_{\text{rad}} + \rho_{\text{mat}} + \rho_\Lambda$, derived from the Friedmann equations (with the cosmological constant Λ absorbed into the energy density term ρ_Λ), defined as the energy density required to obtain a flat Universe: $\rho_c \equiv 3H_0^2/(8\pi G_N)$ [18]. Regarding DM abundance, it is found to be $\Omega_{\text{CDM}} h^2 = 0.1200 \pm 0.0012$.

Combined constraints from the mass function of the galaxy cluster and Lyman-α forest data analysis provide $\Omega_m = 0.34^{+0.13}_{-0.09}$ for a flat Universe [21]. Comparing the measured ratio of the abundance of hydrogen and deuterium to the BBN predictions, one obtains the baryonic matter density $\Omega_b h^2 \sim 0.0205 \pm 0.0018$ [22]. Then, taking $h^2 \sim 0.5$, one obtains $\Omega_{\text{CDM}} \sim \Omega_m - \Omega_b \sim 0.25$, more or less like from the Planck mission results.

As a final remark, non-baryonic particles, like SM neutrinos, thus non-exotic particles, could only make up a negligible portion of dark matter, as they would be hot relics (decouple from the thermal bath when still relativistic) and would thus erase small-scale inhomogeneities by free-streaming. This would result in a Universe with only large-scale structures and would suggest a top-down approach, where big structures fragment into smaller one, to explain the observed small-scale structure in the Universe. Observations tend to favor the opposite (bottom-up) approach of structure evolution [20]. For this reason one believes DM to be mainly made of cold DM particles.

---

[1] This also indicates that dark matter should be cold, thus non-relativistic when decoupling from the thermal bath, in order to not free-stream and erase their own perturbation seeds.

3.2 Thermal relic density of cold dark matter

Let us see now how to compute the relic abundance of a cold dark matter species produced thermally in order to match the observed result. Let us first define some important quantities in terms of the phase-space density $f(\vec{x},\vec{p},t)$, the evolution of which is described by the Boltzmann equation. The FLRW metric being homogeneous and isotropic, it is enough to consider $f(E,t)$ or $f(|\vec{p}|,t)$. One can then define the particle number density, energy density and pressure for a species i, respectively, as [23]

$$n_i = \frac{g_i}{(2\pi)^3}\int f(\vec{p})d^3p, \tag{3.1}$$

$$\rho_i = \frac{g_i}{(2\pi)^3}\int E f(\vec{p})d^3p, \tag{3.2}$$

$$p_i = \frac{g_i}{(2\pi)^3}\int \frac{|\vec{p}|^2}{3E} f(\vec{p})d^3p, \tag{3.3}$$

where g_i is the number of internal degrees of freedom for the species i.

For a species i in kinetic equilibrium with the thermal bath of temperature T, one has [23]

$$f^{\text{eq}}_{\pm}(E_i) = \frac{1}{e^{(E_i-\mu_i)/T}\pm 1}, \tag{3.4}$$

where μ_i is the chemical potential for a species i and where f^{eq}_{+} is the Fermi-Dirac distribution, while f^{eq}_{-} is the Bose-Einstein distribution. For relativistic species in equilibrium, one then obtains [23]

$$n_i^{\text{eq}} = \begin{cases} \frac{\zeta(3)}{\pi^2} g_i T^3 & \text{for bosons} \\ \frac{3}{4}\frac{\zeta(3)}{\pi^2} g_i T^3 & \text{for fermions,} \end{cases} \tag{3.5}$$

$$\rho_i^{\text{eq}} = \begin{cases} \frac{\pi^2}{30} g_i T^4 & \text{for bosons} \\ \frac{7}{8}\frac{\pi^2}{30} g_i T^4 & \text{for fermions,} \end{cases} \tag{3.6}$$

$$p_i^{\text{eq}} = \frac{\rho_i^{\text{eq}}}{3}, \tag{3.7}$$

with $\zeta(3) \simeq 1.20206$.

Since one is interested in the case of cold dark matter, which decouples from the thermal bath when it is non-relativistic, the equilibrium phase-space density for dark matter takes the form of the Maxwell-Boltzmann distribution [23]:

$$f^{\text{eq}}_{\text{NR}}(E_i) = e^{-(E_i-\mu_i)/T}. \tag{3.8}$$

For non-relativistic species in equilibrium, one then obtains [23]

$$n_i^{\text{eq}} = g_i\left(\frac{m_i T}{2\pi}\right)^{3/2} e^{-(m_i-\mu_i)/T}, \tag{3.9}$$

$$\rho_i^{\text{eq}} = m_i n_i^{\text{eq}}, \tag{3.10}$$

$$p_i^{\text{eq}} = n_i^{\text{eq}} T \ll \rho_i^{\text{eq}}. \tag{3.11}$$

In the rest of this section, one neglects the chemical potential μ, a justified assumption in the early Universe [24]. The energy density (3.10) being exponentially suppressed, one can in good approximation only consider relativistic species, the total contribution of which is given by [23]

$$\rho \simeq \rho_{\rm rad} = \frac{\pi^2}{30} g_* T^4, \tag{3.12}$$

$$\text{with } g_* \equiv \sum_b g_b \left(\frac{T_b}{T}\right)^4 + \frac{7}{8}\sum_f g_f \left(\frac{T_f}{T}\right)^4, \tag{3.13}$$

where g_* is the effective number of relativistic degrees of freedom and where b and f respectively stand for bosons and fermions species. Another useful quantity is the entropy density given by [23]

$$s = \sum_i \frac{\rho_i + p_i}{T_i} \simeq \frac{2\pi^2}{45} g_{*s} T^3 \tag{3.14}$$

$$\text{with } g_{*s} \equiv \sum_b g_b \left(\frac{T_b}{T}\right)^3 + \frac{7}{8}\sum_f g_f \left(\frac{T_f}{T}\right)^3, \tag{3.15}$$

with g_{*s} the effective number of degrees of freedom in entropy.

Initially, at a temperature T, DM is in local thermal equilibrium[2] with the SM plasma. Then, as the Universe expands and cools down, a smaller number of particles from the thermal bath can produce DM, thus making SM → DM slightly less efficient, implying that DM annihilates more into SM ($n_{\rm DM}$ decreases) until chemical equilibrium is reached again. This transition from an equilibrium at T to another equilibrium at a lower T is possible because the expansion rate of the Universe H (and thus the change of temperature) is slow enough compared to the interaction rate Γ, so that the system has time to reach a new equilibrium: having $\Gamma \gtrsim H$ implies that the change of the system occurs through successive equilibrium stages. Then, when the temperature of the thermal bath starts to be lower than the DM mass $m_{\rm DM}$, only particles in the right tail of the Maxwell-Boltzmann distribution can produce DM, favoring again DM → SM, thus diminishing the DM particle number density $n_{\rm DM}$ (therefore Γ as well, as shown below), but with Γ still larger than H, so that the equilibrium can be reached. As the Universe expands, at some point $n_{\rm DM}$ will be so low that Γ will become of the same order as H so that DM goes out of local thermal equilibrium again and decouples from the thermal bath: DM particles do not see each other anymore and freeze-out occurs. After that, the particle number density can only be redshifted by the Universe expansion. The evolution of the DM particle number density $n_{\rm DM}$ in this out-of-equilibrium situation, around the freeze-out, is given by the solution of the Boltzmann equation [25]

$$\frac{dn_{\rm DM}}{dt} + 3Hn_{\rm DM} = \langle \sigma v_{\rm Møl}\rangle (n_{\rm DM}^{\rm eq} - n_{\rm DM}), \tag{3.16}$$

where $\langle \sigma v_{\rm Møl}\rangle$ is the thermally averaged annihilation cross section, with $v_{\rm Møl}$ the Møller velocity defined in [25].

It is usually common to express Eq. (3.16) in terms of $Y \equiv n/s$ [23] to cancel out the Universe expansion through the scale factor a. Considering

---

[2] Thus DM is both in chemical (via annihilation processes) and in kinetic (via scattering processes) equilibrium with the SM plasma.

an isentropic expansion of the Universe, the entropy per comoving volume sa^3 is then constant, therefore one has $Y \sim na^3$, with na^3 the number of particles N per comoving volume V/a^3, with V the proper volume. Then the Boltzmann equation (3.16) becomes [23]

$$\frac{x}{Y_{\rm DM}^{\rm eq}}\frac{dY_{\rm DM}}{dx} = -\frac{\Gamma}{H}\left[\left(\frac{Y_{\rm DM}}{Y_{\rm DM}^{\rm eq}}\right)^2 - 1\right], \tag{3.17}$$

with $\Gamma \equiv n_{\rm DM}^{\rm eq}\langle\sigma v_{\rm Møl}\rangle$ and $x \equiv m_{\rm DM}/T$.

This form of the Boltzmann equation puts in evidence the role of the ratio Γ/H mentioned above. Indeed, when the expansion rate is negligible compared to the interaction rate ($\Gamma \gg H$), $Y_{\rm DM}$ follows its equilibrium value: $Y_{\rm DM} = Y_{\rm DM}^{\rm eq}$. This is because in the case $Y_{\rm DM} > Y_{\rm DM}^{\rm eq}$, then $dY_{\rm DM}/dx \sim -\Gamma/H$, thus $Y_{\rm DM}$ decreases until $Y_{\rm DM}$ stabilises at the equilibrium density $Y_{\rm DM}^{\rm eq}$ as the right-hand side vanishes. Similarly, when one has $Y_{\rm DM} < Y_{\rm DM}^{\rm eq}$, then $dY_{\rm DM}/dx \sim \Gamma/H$, thus $Y_{\rm DM}$ increases until $Y_{\rm DM} \simeq Y_{\rm DM}^{\rm eq}$. In the opposite case, $\Gamma \ll H$, then the right-hand side is approximately zero and $Y_{\rm DM}$ remains constant until today in an isentropically expanding Universe with no entropy injection. Indeed, if there is no entropy injection between the time of freeze-out and now, then the relation $Y \sim na^3$ holds and $Y_{\rm DM}$ remains constant: $Y_{\rm DM}(x_f) = Y_\infty \equiv Y_{\rm DM}(x \to \infty)$, with $x_f = m_{\rm DM}/T_f$, where T_f is the temperature at which the freeze-out occurs.

The DM relic density is defined similarly to the density parameters introduced in the previous section as

$$\Omega_{\rm DM}h^2 = \frac{\rho_{\rm DM}}{\rho_{\rm crit}}h^2 = \frac{m_{\rm DM}n_{\rm DM}^0}{\rho_{\rm crit}}h^2 = \frac{m_{\rm DM}s_0Y_\infty}{\rho_{\rm crit}}h^2 \simeq 2.78\times10^8\frac{m_{\rm DM}}{\rm GeV}Y_\infty, \tag{3.18}$$

where one has used the non-relativistic relation $\rho = mn$ in the second equality, where the superscript/subscript 0 denotes the present value of the parameters and where the value of the critical density $\rho_{\rm c}$ and the current entropy density s_0 are given by

$$\rho_{\rm c} \equiv \frac{3H_0^2}{8\pi G_N} \xrightarrow{\times\frac{1}{c^3\hbar}=1} 1.05\times10^{-5}h^2 \text{ GeV cm}^{-3} \tag{3.19}$$

$$\text{and } s_0 = \frac{2\pi^2}{45}g_{*s}^0T_0^3 \simeq 2926.44 \text{ cm}^{-3}, \tag{3.20}$$

$$\text{with } g_{*s}^0 = 2 + N_{\rm eff}\,\frac{7}{8}\times2\times\frac{4}{11} \simeq 3.94, \tag{3.21}$$

$$T_0 \simeq 2.73\text{K} \xrightarrow{\times\frac{k_B}{c\hbar}=1} 11.92 \text{ cm}^{-1} \tag{3.22}$$

where $N_{\rm eff} \simeq 3.044$ has been used [26].[3]

A very good analytical approximation, which fits the numerical solution of the Boltzmann equation best, can be found for x_f and $Y_\infty = Y(x_f)$ in [23]. In particular, one finds that Y_∞ goes as

$$Y_\infty \sim \frac{10^{-18}}{m_{\rm DM}\langle\sigma v_{\rm Møl}\rangle}\text{ GeV}^{-1} \tag{3.23}$$

---

[3] $N_{\rm eff}$ is used instead of 3 to account for the fact that the neutrino decoupling is not instantaneous (they thus also enjoy part of the entropy transfer from $e^\pm$ decoupling) and that finite-temperature QED corrections to the electromagnetic plasma ($e^\pm$ and γ) imply a reduced release of that entropy. [27]

for a typical value $x_f \sim 25$ [28].

For the particularly interesting case of Weakly Interacting Massive Particle (WIMP) dark matter, typical weak-scale mass and couplings lead to [29]

$$\langle \sigma v_{\text{Møl}} \rangle \sim 10^{-9}\ \text{GeV}^{-2} \sim 1\ \text{pb} \sim 3 \times 10^{-26} \text{cm}^3/\text{s}, \tag{3.24}$$

which, when combined with Eq. (3.18) and (3.23) (this gives $\Omega_{\text{DM}} h^2 \sim 0.1 \times 10^{-9} / \langle \sigma v_{\text{Møl}} \rangle$), roughly yields the observed DM abundance. This is known in the literature as the WIMP miracle. As shown in [30], this miracle is not peculiar to the electroweak scale. Indeed for other combination of DM mass and couplings one can still obtain a (WIMPless) miracle and find the right relic density.

To end this section, let us roughly identify the mass range for a WIMP particle. Expressing $\langle \sigma v_{\text{Møl}} \rangle$ in terms of a dimensionless coupling λ, then by dimensional analysis, an upper bound from the perturbative unitarity constraint [31] is found to be

$$10^{-9}\ \text{GeV}^{-2} \sim \langle \sigma v_{\text{Møl}} \rangle \sim \frac{\lambda}{m_{\text{DM}}^2} \leq \frac{4\pi}{m_{\text{DM}}^2}, \tag{3.25}$$

therefore leading to $m_{\text{DM}} \leq 110$ TeV.

A lower bound for WIMP mass can be found from the so-called Lee-Weinberg limit [32]. As one is interested in a lower bound, one can consider the case $m_{\text{DM}} \ll m_Z, m_W$. Then a typical electroweak interaction involves the Fermi coupling constant $G_F \simeq 1.17 \times 10^{-5}\ \text{GeV}^2$ [33] and m_{DM}, the mass scale of the problem: $\langle \sigma v_{\text{Møl}} \rangle \sim 0.1\, G_F^2 m_{\text{DM}}^2$ (taking $v_{\text{Møl}} \sim 0.1$). Since for WIMPs, one has $\langle \sigma v_{\text{Møl}} \rangle \sim 10^{-9}\ \text{GeV}^{-2}$, then one finds that to obtain the right abundance $\Omega_{\text{DM}} h^2 \sim 0.1$ or under-abundance, one approximately requires

$$1 \geq \frac{\Omega_{\text{DM}} h^2}{0.1} \sim \frac{10^{-9}\ \text{GeV}^{-2}}{\langle \sigma v_{\text{Møl}} \rangle} \sim \frac{10^{-8}\ \text{GeV}^{-2}}{G_F^2 m_{\text{DM}}^2} \sim \left(\frac{10\ \text{GeV}}{m_{\text{DM}}} \right)^2, \tag{3.26}$$

implying $m_{\text{DM}} \geq 10$ GeV.

Note that the way of computing the relic density of thermally produced DM particles demonstrated in this section suffers from three well-known caveats [34]. Indeed, a more appropriate expression for $\langle \sigma v_{\text{Møl}} \rangle$ should be used when one is in the resonance region, or in the case of co-annihilation or forbidden channels (which become allowed at some non-zero temperature).

3.3 Direct detection of WIMPs

The possibility of looking for dark matter via direct-detection experiments was first proposed in [35]. Constraints from DM direct detection can be very stringent for WIMP DM models. In the case of scalar DM, these constraints are put into the form of exclusion limits in the plane $(\sigma_{\text{SI}}, m_{\text{WIMP}})$, with σ_{SI} the spin-independent scattering cross section between the WIMP and the target nucleon in the experiment. The rules of the game for new DM models are then to be such that the predicted σ_{SI} remain below the exclusion limits from past direct-detection experiments, in order to not be ruled out.

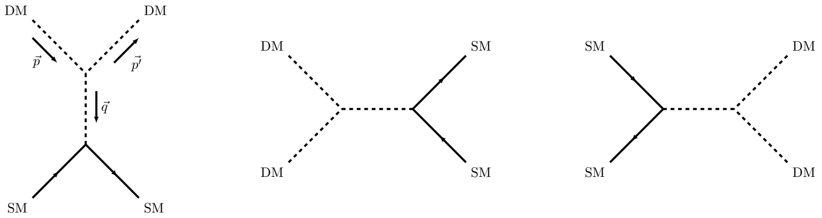

Figure 3.1: Left panel: scattering process studied in DM direct-detection experiments. Middle panel: annihilation process studied in DM indirect-detection experiments. Right panel: DM production process studied in collider searches.

In the centre-of-mass (CM) frame, one can express the relative velocity as

$$\vec{v}_{\rm rel} \equiv \vec{v}_{\rm WIMP} - \vec{v}_N = \frac{m_{\rm WIMP}}{\mu_N}\vec{v}_{\rm WIMP} \tag{3.27}$$

$$\text{with} \quad \mu_N \equiv \frac{m_{\rm WIMP} m_N}{(m_{\rm WIMP} + m_N)} \tag{3.28}$$

the WIMP-nucleus reduced mass (the typical mass scale in a two-body problem) and where the subscript N denotes the target nucleus. Moreover, for an elastic[4] scattering process (see left panel in Fig. 3.1), one has $|\vec{p}| = |\vec{p'}|$. Therefore, the recoil energy E_r of the target nucleus is given in term of the momentum transfer $\vec{q} \equiv \vec{p} - \vec{p'}$ as [37]

$$E_r = \frac{|\vec{q}|^2}{2m_N} = \frac{\mu_N^2}{m_N} v_{\rm rel}^2 (1 - \cos\theta), \tag{3.29}$$

with θ the angle between $\vec{p}$ and $\vec{p'}$.

By computing dE_r/dm_N and d^2E_r/dm_N^2, one finds that the recoil energy is maximised for $m_N = m_{\rm WIMP}$ [37]. If in addition one chooses the angle θ for which E_r is the largest, i.e. the backscattering angle $\theta = \pi$, one then obtains $E_r^{\rm max} = \frac{1}{2} m_{\rm WIMP} v_{\rm rel}^2$. Moreover, since $v_{\rm rel}$ should be below $v_{\rm esc} \simeq 600$ km/s $\simeq 2 \times 10^{-3}c$ [38], the velocity beyond which DM can escape the galaxy (and thus not reach our detector), one then obtains, for a typical WIMP mass $m_{\rm WIMP} \sim 100$ GeV, that the maximal energy recoil is $E_r < 200$ keV, implying, via Eq. (3.29), $q \equiv |\vec{q}| < 200$ MeV for the momentum transfer.

Given that the relative velocity of DM from galactic halo is $v_{\rm rel} \simeq 300$ km/s $\simeq 10^{-3}c$, one can safely consider the non-relativistic limit [38]. In that limit, the product of σ_0, the cross section at zero momentum transfer q, and the form factor[5] $F^2(q)$ appearing in [39]

$$\frac{d\sigma(q)}{dq^2} = \frac{1}{\pi v^2}|\mathcal{M}|^2 = \frac{\sigma_0 F^2(q)}{4\mu_N^2 v^2}, \tag{3.30}$$

with $\mathcal{M}$ the invariant amplitude of the process depicted in the left panel of Fig. 3.1, can be decomposed into a (scalar) spin-independent and an

---

[4] Inelastic scattering would require a non-minimal dark sector of at least two dark species (see for instance [36]), though not necessarily two DM candidates.

[5] This form factor takes into account the fact that at $q \neq 0$, one might not have $q \ll R_N^{-1}$ anymore and start to probe the inner structure of the nucleus of size R_N. In the case $q \ll R_N^{-1}$, DM interacts coherently with all the nucleons of the target nucleus [38].

(axial-vector) spin-dependent part [40, 41]:

$$\sigma_0 F^2(q) \simeq \sigma_0^{\rm SI} F_{\rm SI}^2(q) + \sigma_0^{\rm SD} F_{\rm SD}^2(q) \tag{3.31}$$

where the spin-independent and the spin-dependent cross sections are, respectively, given by [39, 42]

$$\sigma_0^{\rm SI} = \frac{4\mu_N^2}{\pi}[Zf_p + (A-Z)f_n]^2 = \frac{\mu_N^2}{\mu_p^2}A^2\sigma_p^{\rm SI}, \tag{3.32}$$

where $f_p \simeq f_n$ is assumed in the last equality, with μ_p the WIMP-proton reduced mass and with $\sigma_p^{\rm SI} = \frac{4}{\pi}\mu_p^2 f_p^2$, and

$$\sigma_0^{\rm SD} = \frac{32\mu_N^2 G_F^2}{\pi}\frac{J+1}{J}[a_p\langle S_p\rangle + a_n\langle S_n\rangle]^2, \tag{3.33}$$

where $f_{p/n}$ and $a_{p/n}$ are, respectively, the spin-independent and spin-dependent effective coupling of the WIMP to the proton/neutron, Z is the number of protons, A is the number of nucleons, J is the total nuclear spin and $\langle S_{p/n}\rangle$ is the expectation values of the total spin operator for protons/neutrons in the interacting nucleus [43].

For a massive mediator $m_{\rm med} \sim \mathcal{O}(100)$ GeV, then given the upper bound found above for q, this justifies the usually considered zero-momentum-transfer limit. In that limit, of course, $F^2(q \to 0) = 1$ and one is thus only interested in $\sigma_0^{\rm SI}$ in the case of scalar DM (no spin-dependent interactions) and thus in $\sigma_p^{\rm SI}$, given Eq. (3.32). Note that in the limit of zero momentum transfer or velocity suppression, pseudoscalar bilinear matrix elements are suppressed [44], thereby tree-level scattering amplitudes involving fermionic DM with a pseudoscalar mediator are suppressed. In that case, it is convenient to consider one-loop scattering processes to constrain the model via direct-detection experiments.

In the papers of this thesis (see Publications section), exclusion limit from XENON1T, PandaX-4T and LUX-ZEPLIN (LZ) [45–47], all using xenon as the target nucleus, have been considered,[6] where for $m_{\rm WIMP} \sim$ 100 GeV for instance, it requires $\sigma_p^{\rm SI} \lesssim 10^{-46} - 10^{-47}$ cm^2. As can be seen from Eq. (3.32), the spin-independent cross section is enhanced with the number of nucleon of the interacting nucleus. Moreover, as mentioned above, the recoil energy is maximised for $m_N = m_{\rm WIMP}$. This is the reason why among the liquefied noble gases (a suitable choice for direct-detection experiments [49]), xenon is an excellent choice.

---

[6] While writing this thesis, first results from DM search via XENONnT experiments have been released in [48]. The sensitivity curve is nevertheless weaker than the LZ one [47].

Chapter 4

Thermally-corrected effective potential

To compute the power spectrum of the stochastic gravitational-wave background from first-order phase transition in the early Universe one needs the thermally-corrected effective potential in terms of the classical background field ϕ_b:

$$V_{\text{eff}}(\phi_b) \equiv V_0(\phi_b) + V_{\text{CW}}(\phi_b) + V_{\text{CT}}(\phi_b) + V_T(\phi_b, T), \tag{4.1}$$

where V_0 is the tree-level potential. The quantum corrections are encapsulated in the Coleman-Weinberg effective potential V_{CW} and the counterterms V_{CT} which will be the subject of the Section 4.1. Last but not least, thermal corrections V_T of the effective potential are given in Section 4.2.

4.1 Quantum corrections

In the study of phase transitions, quantum corrections cannot be omitted, since it has been shown in [50] that they can destabilise the classical minimum of the theory and induce spontaneous symmetry breaking. The aim of this section is to build the effective potential in order to identify the real vacuum of the theory at zero temperature.

4.1.1 The effective potential

The generating functional $Z[J]$ is defined as [51]

$$Z[J] \equiv \langle J, +\infty | J, -\infty \rangle = \int \mathcal{D}\phi e^{iS[\phi] + i\int d^4x J(x)\phi(x)}, \tag{4.2}$$

where $J(x)$ is a classical current or external source coupled to $\phi(x)$ and $S[\phi]$ is the action. This corresponds to the transition amplitude to go from the ground state in the far past $|0, t \to -\infty\rangle$ to the vacuum in the far future $|0, t \to +\infty\rangle$ in the presence of J.

While $Z[J]$ generates all connected and disconnected diagrams, it can be shown that $W[J] \equiv e^{iZ[J]}$ only contains connected diagrams [11]. One can Taylor expand $Z[J]$ and express it in terms of the Green functions

$G^{(n)}(x_1,\ldots,x_n)$ as [11,51]

$$Z[J]=\sum_{n=0}^{\infty}\frac{i^n}{n!}\int d^4x_1\ldots d^4x_n G^{(n)}(x_1,\ldots,x_n)J(x_1)\ldots J(x_n)$$

$$\text{with } G^{(n)}(x_1,\ldots,x_n)\equiv\langle J|T\{\phi(x_1)\ldots\phi(x_n)\}|J\rangle$$
$$=(-i)^n\frac{1}{Z[J]}\frac{\delta^n Z}{\delta J(x_1)\ldots\delta J(x_n)}. \tag{4.3}$$

Similarly, one can Taylor expand $W[J]$ and express it in terms of the connected Green functions $G_c^{(n)}(x_1,\ldots,x_n)$ as [11,51]

$$W[J]=\sum_{n=0}^{\infty}\frac{i^n}{n!}\int d^4x_1\ldots d^4x_n(-i)G_c^{(n)}(x_1,\ldots,x_n)J(x_1)\ldots J(x_n)$$

$$\text{with } G_c^{(n)}(x_1,\ldots,x_n)\equiv\langle J|T\{\phi(x_1)\ldots\phi(x_n)\}|J\rangle_{\text{connected}}$$
$$=i(-i)^n\frac{\delta^n W}{\delta J(x_1)\ldots\delta J(x_n)}. \tag{4.4}$$

As demonstrated in [11], one can express the effective action $\Gamma[\phi_{\text{cl}}]$ as the Legendre transformation of $W[J]$:

$$\Gamma[\phi_{\text{cl}}]=W[J]-\int d^4xJ(x)\phi_{\text{cl}}(x) \tag{4.5}$$

$$\text{with } \phi_{\text{cl}}\equiv\frac{\delta W[J]}{\delta J}=\langle J|\phi|J\rangle. \tag{4.6}$$

From Eq. (4.5), one directly obtains the following important result:

$$\frac{\delta\Gamma[\phi_{\text{cl}}]}{\delta\phi_{\text{cl}}}=-J, \tag{4.7}$$

which indicates that $\phi_{\text{cl}}=\langle 0|\phi|0\rangle\equiv\langle\phi\rangle$ is the ground state of the theory in absence of external source ($J=0$). Note that the classical[1] background field ϕ_{cl} should not be confused with the classical configuration ϕ_{tree} which satisfies the classical equation of motion $\delta S/\delta\phi=-J$. It can be shown that $\phi_{\text{cl}}=\phi_{\text{tree}}+\mathcal{O}(\text{quantum corrections})$ [52].

In the same way, one can Taylor expand the effective action $\Gamma[\phi_{\text{cl}}]$ and express it in terms of the one-particle-irreducible (1PI) Green functions $\Gamma^{(n)}(x_1,\ldots,x_n)$ as [11,51]

$$\Gamma[\phi_{\text{cl}}]=\sum_{n=0}^{\infty}\frac{1}{n!}\int d^4x_1\ldots d^4x_n\Gamma^{(n)}(x_1,\ldots,x_n)\phi_{\text{cl}}(x_1)\ldots\phi_{\text{cl}}(x_n) \tag{4.8}$$

$$\text{with } \Gamma^{(n)}(x_1,\ldots,x_n)\equiv -i\langle J|T\{\phi(x_1)\ldots\phi(x_n)\}|J\rangle_{\text{1PI}}$$
$$=\frac{\delta^n\Gamma[\phi_{\text{cl}}]}{\delta\phi_{\text{cl}}(x_1)\ldots\delta\phi_{\text{cl}}(x_n)}. \tag{4.9}$$

Following the excellent review [51], after performing a Fourier transform of $\Gamma^{(n)}(x)$ and $\phi_{\text{cl}}(x)$, one obtains

$$\Gamma[\phi_{\text{cl}}]=\sum_{n=0}^{\infty}\int\prod_{j=1}^{n}\left[\frac{d^4p_j}{(2\pi)^4}\tilde{\phi}_{\text{cl}}(-p_j)\right](2\pi)^4\delta^{(4)}(p_1+\cdots+p_n)\Gamma^{(n)}(p_1,\ldots,p_n). \tag{4.10}$$

---

[1] It is classical in the sense that quantum fluctuations have been averaged over, as suggested by the expectation value $\langle\ \rangle$.

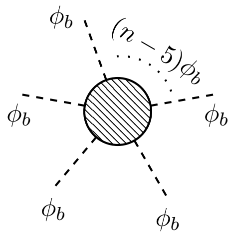

Figure 4.1: $i\Gamma^{(n)}(p=0)$.

Next, considering the theory to be invariant under translations ($\phi_{\rm cl}(x) = \phi_b$, with $\partial_\mu \phi_b = 0$), one finally obtains [51]

$$\Gamma[\phi_b] = \sum_{n=0}^{\infty} \frac{\phi_b^n}{n!} \Gamma^{(n)}(p_j = 0) \int d^4x. \tag{4.11}$$

Alternatively, one then can write the effective action for constant background fields ϕ_b as

$$\begin{aligned} \Gamma[\phi_b] &\equiv \int d^4x \mathcal{L}_{\rm eff} \\ &= -V_{\rm eff}(\phi_b) \int d^4x, \end{aligned} \tag{4.12}$$

where the kinetic part in $\mathcal{L}_{\rm eff}$ vanishes for constant fields. By comparing both expressions for $\Gamma[\phi_b]$, Eq. (4.12) and (4.11), one then finds that the effective potential can be written as

$$\begin{aligned} V_{\rm eff}(\phi_b) &= -\sum_{n=0}^{\infty} \frac{\phi_b^n}{n!} \Gamma^{(n)}(p_j = 0) \\ &= i \sum_{n=0}^{\infty} \frac{\phi_b^n}{n!} i\Gamma^{(n)}(p_j = 0), \end{aligned} \tag{4.13}$$

where $i\Gamma^{(n)}(p_j = 0)$ contains the 1PI diagrams of any loop order with n external legs $\phi_b = \langle \phi \rangle$ ($p_j = 0 \leftrightarrow \partial_{x_j} = 0$) as VEV insertions, as depicted in Fig. 4.1.

4.1.2 The Coleman-Weinberg potential

Let us compute the effective potential for the simple case of the ϕ^4 theory, with the tree-level potential given by

$$V_\phi(\phi \to \phi_b + \phi) = \frac{m^2}{2}(\phi_b + \phi)^2 + \frac{\lambda}{4!}(\phi_b + \phi)^4, \tag{4.14}$$

where ϕ is an excitation around the background field ϕ_b, with $\langle \phi \rangle = 0$.

The effective potential at the lowest loop order is obviously obtained by considering no loop in diagrams from Fig. 4.1. Since the potential (4.14) only admits two- and four-point vertices, the only allowed terms in the expansion (4.13) are $\Gamma_0^{(2)}(p = 0)$ and $\Gamma_0^{(4)}(p = 0)$, where the subscript

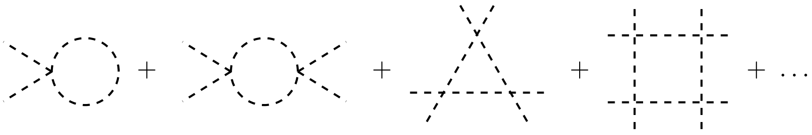

Figure 4.2: One-loop 1PI polygonal Feynman diagrams, with zero external momenta, in the ϕ^4 theory. The external lines correspond to the constant background field or VEV $\phi_b = \langle\phi\rangle$, while the internal lines or propagators correspond to the excitations ϕ around ϕ_b.

0 indicates that one is at 0th loop order (tree level). For the V_0 part in Eq. (4.1), one then obtains

$$\begin{aligned} V_0(\phi_b) \equiv V^0_{\text{eff}}(\phi_b) &= i\left[\frac{\phi_b^2}{2}(-im^2) + \frac{\phi_b^4}{4!}(-i\lambda)\right] \\ &= \frac{m^2}{2}\phi_b^2 + \frac{\lambda}{4!}\phi_b^4 \\ &= V_\phi(\phi+\phi_b)|_{\phi=0}, \end{aligned} \tag{4.15}$$

where the minus sign in the Feynman rule comes from the fact that the potential appears as $-V_{\text{eff}}$ in $\mathcal{L}_{\text{eff}}$ and where one has recovered the tree-level potential (4.14) in the vacuum as $V_\phi(\phi_b)$.

At next loop order, the only allowed one-loop PI diagrams are the infinite series of polygonal diagrams [50] shown in Fig. 4.2. Mathematically, the one-loop effective potential takes the form [50, 51]

$$\begin{aligned} V^1_{\text{eff}}(\phi_b) &= i\sum_{n=1}^{\infty}\int\frac{d^4p}{(2\pi)^4}\frac{1}{2n}\left[\frac{\lambda\phi_b^2/2}{p^2-m^2+i\epsilon}\right]^n \\ &= \frac{-i}{2}\int\frac{d^4p}{(2\pi)^4}\ln\left[1-\frac{\lambda\phi_b^2/2}{p^2-m^2+i\epsilon}\right], \end{aligned} \tag{4.16}$$

where one used $\ln(1-x) = -\sum_{n=1}^{\infty}x^n/n$ in the last equality. After performing a Wick rotation it becomes

$$V^1_{\text{eff}}(\phi_b) = \frac{1}{2}\int\frac{d^4p_E}{(2\pi)^4}\ln\left[p_E^2+m^2(\phi_b)\right] + \phi_b\text{-independent terms,} \tag{4.17}$$

where p_E is the Euclidean momentum and where

$$m^2(\phi_b) = m^2 + \frac{\lambda}{2}\phi_b^2 = \frac{d^2V^0_{\text{eff}}(\phi_b)}{d\phi_b^2} = \left.\frac{d^2V_\phi(\phi+\phi_b)}{d\phi^2}\right|_{\phi=0} \tag{4.18}$$

is the (background-)field-dependent mass. This last expression is obviously ultraviolet (UV) divergent. With the appropriate set of counterterms, then, using the dimensional regularisation (which introduces the renormalisation scale μ) followed by the $\overline{\text{MS}}$ scheme, one then obtains the Coleman-Weinberg part V_{CW} in Eq. (4.1), given by [51]

$$V_{\text{CW}}(\phi_b) \equiv V^1_{\text{eff}}(\phi_b) = \frac{1}{64\pi^2}m^4(\phi_b)\left(\ln\frac{m^2(\phi_b)}{\mu^2} - \frac{3}{2}\right). \tag{4.19}$$

In a similar way one can compute the one-loop contributions to the effective potential when fermions or gauge bosons are coupled to the background fields ϕ_b, through their field-dependent masses. The Standard Model is a perfect example to illustrate a theory with contributions from scalars, fermions and gauge bosons. The one-loop contributions to the SM effective potential are given in the Landau gauge[2] by [51]

$$V_{\text{CW}}^{\text{SM}}(\phi_b) \equiv V_{\text{eff, SM}}^{1}(\phi_b) = \frac{1}{64\pi^2}\sum_i n_i m_i^4(\phi_b)\left[\ln\frac{m_i^2(\phi_b)}{\mu^2} - C_i\right], \tag{4.20}$$

with $i \in \{W^\pm, Z, h, G_0, G^\pm, t\}$ and where one neglected Yukawa contributions except from the top quark t. The bosonic and fermionic degrees of freedom are encoded in n_i and C_i are constants peculiar to the renormalisation scheme. One has $n_{W^\pm} = 6$, $n_Z = 3$, $n_t = -12$, $n_h = n_{G^0}$ and $n_{G^\pm} = 2$, where the minus sign for t comes from fermion loops.[3] After using dimensional regularisation and applying the $\overline{\text{MS}}$ subtraction scheme, one is left with $C_i = \frac{3}{2}$ for scalars and fermions, as well as $C_i = \frac{5}{6}$ for vector bosons. When considering Parwani daisy resummation (see next section), it is more convenient to split the contributions from transverse and longitudinal modes of gauge bosons, in which case one has $n_{W_T^\pm} = 4$, $n_{W_L^\pm} = n_{Z_T} = 2$, $n_{Z_L} = 1$ and $C_i = \frac{1}{2}$ for transverse vector bosons, as well as $C_i = \frac{3}{2}$ for longitudinal vector bosons.[4] Finally, $m_i^2(\phi_b)$ correspond to the eigenvalues of the ϕ_b-dependent mass matrix.

The scalar part of the SM potential is given by

$$V_H = -\mu^2|H|^2 + \lambda|H|^4 \tag{4.21}$$

with the SM Higgs doublet defined as

$$H = \frac{1}{\sqrt{2}}\begin{pmatrix} G_1 + iG_2 \\ \phi_b + h + iG_0 \end{pmatrix}. \tag{4.22}$$

The field dependent mass of the Higgs field h and the Goldstone bosons G_0, G_1, G_2 are given by

$$m_h^2(\phi_b) = \left.\frac{\partial^2 V_H}{\partial h^2}\right|_{\phi_d=0} = -\mu^2 + 3\lambda\phi_b^2, \tag{4.23}$$

$$m_G^2(\phi_b) = \left.\frac{\partial^2 V_H}{\partial G_0^2}\right|_{\phi_d=0} = -\mu^2 + \lambda\phi_b^2, \tag{4.24}$$

where ϕ_d denotes all the dynamical fields. The specific value of ϕ_b which minimises the potential (4.21) along the h direction is

$$\left.\frac{\partial V_H}{\partial h}\right|_{\phi_d=0} = 0 \Longleftrightarrow \phi_b = v \equiv \sqrt{\frac{\mu^2}{\lambda}}, \tag{4.25}$$

---

[2] This gauge allows us to get rid of ghosts. Indeed, in Landau gauge and at one-loop order, ghosts decouple from scalars [50], which are the only background fields one considers here.

[3] To understand why, in Landau gauge, one has the degree of freedom of massive gauge bosons together with Goldstones, see the appendix in [53]. In particular it is shown that talking about degree of freedom n_W, n_Z for the massive gauge bosons is a abuse of notation; the fortuitous correspondence between the value of n_W, n_Z and the number of polarisation states is not true in every gauge.

[4] It both cases the number of degrees of freedom is the same: $(6+3)\times\frac{5}{6} = (4+2)\times\frac{1}{2} + (2+1)\times\frac{3}{2} = \frac{45}{6}$.

which yields $m_G^2(v) = 0$ as expected. Finally, the masses of $W^\pm, Z$ and t were obtained in the electroweak vacuum in Eq. (2.13) and below Eq. (2.16), thus for the specific value $\phi_b = v$. The field-dependent masses are then simply given by replacing v with ϕ_b:

$$m_{W^\pm}^2 = \frac{g_2^2}{4}\phi_b^2, \quad m_Z^2 = \frac{g_1^2 + g_2^2}{4}\phi_b^2, \quad m_t^2 = \frac{y_t^2}{2}\phi_b^2. \tag{4.26}$$

To conclude this section on the zero-temperature one-loop effective potential, let us describe the *finite*-counterterm part $V_{\rm CT}$ present in Eq. (4.1). The idea of adding this term is to make the effective potential more convenient to use for numerical purpose. It is indeed easier to directly use the one-loop renormalised values in the parameter from the tree-level potential V_0 in Eq. (4.1). Then to compensate further modifications from the Coleman-Weinberg potential $V_{\rm CW}$, one introduces finite counterterms encoded in $V_{\rm CT}$ in order to keep these modified parameters at their *tree-level* values. $V_{\rm CT}$ is finite as the infinities have already been removed when building $V_{\rm CW}$ [54]. In practice, if one wants for instance to keep the value of the VEV and mass unchanged in the present vacuum v, $V_{\rm CT}$ has to satisfy the following conditions, respectively:

$$\frac{\partial}{\partial \phi_b}(V_{\rm CW} + V_{\rm CT})\bigg|_{\phi_b = v} = 0 \quad \text{and} \quad \frac{\partial^2}{\partial \phi_b^2}(V_{\rm CW} + V_{\rm CT})\bigg|_{\phi_b = v} = 0. \tag{4.27}$$

4.2 Thermal corrections

When studying the phase transitions in the early Universe, the temperature of the ambient plasma is such that it cannot be neglected as this thermal medium will impact the physics of the studied processes. The paradigm used to incorporate such thermal effects is thermal quantum field theory (TQFT).

4.2.1 The thermal effective potential

In relativistic quantum systems, the number of particles is not fixed because annihilation and creation of particles are possible. It is thus suitable to work in the *grand canonical ensemble*, in which the system can exchange particles and energy while keeping the temperature T, volume and chemical potential μ fixed [55]. In quantum statistical physics, the density matrix in the grand canonical ensemble is defined as [55]

$$\rho = e^{-\beta\left(H - \sum_i \mu_i N_i\right)}, \tag{4.28}$$

where i runs over the different species and $\beta \equiv 1/T$. In the following, one will consider for simplicity the case of real scalar fields ϕ, which thus have no conserved charge ($\mu = 0$).

The partition function Z_β is given as the trace of ρ [55]:

$$Z_\beta = \mathrm{Tr}[\rho] = \mathrm{Tr}\left[e^{-\beta H}\right] = \sum_a \int d\phi_a \langle \phi_a | e^{-\beta H} | \phi_a \rangle, \tag{4.29}$$

where one sums over all the states ϕ_a and where $|\phi\rangle$ is the eigenvalue of the field operator $\hat{\phi}$: $\hat{\phi}|\phi\rangle = \phi|\phi\rangle$. This last expression should remind us quantum field theory, where a typical transition amplitude from an initial state $|\phi_a\rangle$ to a final state $|\phi_b\rangle$, with a time-independent Hamiltonian $H = \int d^3x\mathcal{H}$ can be expressed as [14]

$$\begin{aligned}\langle\phi_b|e^{-iHt_f}|\phi_a\rangle &= C\int\mathcal{D}\phi\ e^{iS}\\ &= C\int\mathcal{D}\phi\ e^{i\int_0^{t_f}dt\int d^3x\ \mathcal{L}[\phi,\partial_t\phi]}\\ &= \int\mathcal{D}\pi\int_{\phi(0,\vec{x})=\phi_a(\vec{x})}^{\phi(t_f,\vec{x})=\phi_b(\vec{x})}\mathcal{D}\phi\ e^{i\int_0^{t_f}dt\int d^3x\ (\pi\partial_t\phi-\mathcal{H}[\phi,\pi])},\end{aligned} \tag{4.30}$$

where C is a constant coming from the Gaussian integral over π and where one integrates over all path ϕ with end points $\phi(0,\vec{x}) = \phi_a(\vec{x})$ and $\phi(t_f,\vec{x}) = \phi_b(\vec{x})$. Taking the lower and upper boundaries in the time integral as $-\infty$ and $+\infty$, respectively, one recovers the generating functional $Z[0]$ from Eq. (4.2).

Therefore there is a way to express the partition function (4.29) only in terms of fields by using Eq. (4.30) with the following changes:

$$\left.\begin{matrix}\phi_a(\vec{x}) = \phi_b(\vec{x})\\ it = \tau \quad (it_f = \beta)\end{matrix}\right\} \Rightarrow \phi(0,\vec{x}) = \phi(\beta,\vec{x}). \tag{4.31}$$

One thus obtains a path integral formulation for the quantum-statistical-physics partition function:

$$\begin{aligned}Z_\beta &= \int\mathcal{D}\pi\int_{\text{periodic}}\mathcal{D}\phi\ e^{\int_0^\beta d\tau\int d^3x\ (\pi\partial_\tau\phi-\mathcal{H}[\phi,\pi])}\\ &= C\int_{\text{periodic}}\mathcal{D}\phi\ e^{-\int_0^\beta d\tau\int d^3x\ \mathcal{L}_E[\phi,\partial_\tau\phi]}\\ &= C\int_{\text{periodic}}\mathcal{D}\phi\ e^{-S_E},\end{aligned} \tag{4.32}$$

where *periodic* indicates that the integration path should satisfy $\phi(0,\vec{x}) = \phi(\beta,\vec{x})$. This comes from the fact that the initial and final states are identical ($\phi_a = \phi_b$), which is a consequence of the trace. This last expression looks like the generating functional $Z[0]$ (see Eq. (4.2)) in QFT in the Euclidean spacetime (after a Wick rotation) and with the imaginary time $\tau = it$ compactified along a circle of circumference β.

The fact that the bosonic fields are periodic allows us to express them as a Fourier series [56]:

$$\phi(\tau,\vec{x}) = \frac{1}{\beta}\sum_{a=-\infty}^{+\infty}\tilde{\phi}(\omega_a,\vec{x})e^{i\omega_a\tau} \quad \text{with} \quad \omega_a = 2a\frac{\pi}{\beta},\ a\in\mathbb{Z}, \tag{4.33}$$

introducing the Matsubara frequencies ω_a defined such that $\phi(\tau,\vec{x}) = \phi(\tau+\beta,\vec{x})$.

The bosonic thermal Green functions are defined as [55]:

$$\begin{aligned}G_B(\vec{x},\vec{y};\tau_1,\tau_2) &\equiv \frac{1}{Z_\beta}\mathrm{Tr}\left[\rho\mathcal{T}_\tau\left\{\phi(\tau_1,\vec{x})\phi(\tau_2,\vec{y})\right\}\right]\\ &= \frac{\mathrm{Tr}\left[e^{-\beta H}\mathcal{T}_\tau\left\{\phi(\tau_1,\vec{x})\phi(\tau_2,\vec{y})\right\}\right]}{\mathrm{Tr}\left[e^{-\beta H}\right]}\end{aligned} \tag{4.34}$$

with $\mathcal{T}_\tau\{\dots\}$ the imaginary time-ordered product. Since $\mathcal{T}_\tau$ commutes with $e^{-\beta H}$ and one has $e^{\beta H}\phi(0,\vec{y})e^{-\beta H} = \phi(\beta,\vec{y})$, one can show that bosonic thermal Green functions are periodic in τ with period β [55]:

$$\begin{aligned} G_B(\vec{x},\vec{y};\tau,0) &= \frac{1}{Z_\beta}\mathcal{T}_\tau\left\{\mathrm{Tr}\left[e^{-\beta H}\phi(\tau,\vec{x})\phi(0,\vec{y})\right]\right\} \\ &= \frac{1}{Z_\beta}\mathcal{T}_\tau\left\{\mathrm{Tr}\left[e^{-\beta H}e^{\beta H}\phi(0,\vec{y})e^{-\beta H}\phi(\tau,\vec{x})\right]\right\} \\ &= \frac{1}{Z_\beta}\mathcal{T}_\tau\left\{\mathrm{Tr}\left[e^{-\beta H}\phi(\beta,\vec{y})\phi(\tau,\vec{x})\right]\right\} \\ &= \frac{1}{Z_\beta}\mathcal{T}_\tau\left\{\mathrm{Tr}\left[e^{-\beta H}\phi(\tau,\vec{x})\phi(\beta,\vec{y})\right]\right\} \\ &= G_B(\vec{x},\vec{y};\tau,\beta), \end{aligned} \tag{4.35}$$

where one used to cyclic property of the trace in the second line and the freedom of commuting scalar fields within $\mathcal{T}_\tau\{\dots\}$ in the fourth line.

The periodicity of G_B imposes the same periodicity for the bosonic fields, confirming the result previously obtained: $\phi(0,\vec{x}) = \phi(\beta,\vec{x})$. Similarly it can be shown that fermionic thermal Green function are anti-periodic in τ with period β, thus imposing anti-periodicity for fermion fields [55]: $\psi(0,\vec{x}) = -\psi(\beta,\vec{x})$. The latter can then be expressed similarly to boson fields as a Fourier series but with the Matsubara frequency $\omega_a = (2a+1)\pi/\beta$.

The one-loop effective potential from TQFT for the ϕ^4 theory, is obtained in the same way as for Eq. (4.16), that is by summing the same diagrams as in Fig. 4.2, but by using thermal Green functions defined above instead. In practice, in the imaginary-time formalism, it amounts to consider the following substitution [57]

$$\int \frac{dp^0}{2\pi} f(p^0) \longrightarrow \frac{i}{\beta}\sum_{a=-\infty}^{+\infty} f(p^0 = i\omega_a) \text{ with } \omega_a = \begin{cases} 2a\frac{\pi}{\beta} & \text{for bosons} \\ (2a+1)\frac{\pi}{\beta} & \text{for fermions} \end{cases}, \tag{4.36}$$

with $p = (p^0,\vec{p}) \to p_E = (i\omega_a,\vec{p})$. This then leads to

$$\begin{aligned} V_{\text{eff}}^{\beta,1}(\phi_b) &= i\sum_{n=1}^{\infty}\frac{i}{\beta}\sum_{a=-\infty}^{\infty}\int\frac{d^3p}{(2\pi)^3}\frac{1}{2n}\left[\frac{\lambda\phi_b^2/2}{-\omega_a^2-|\vec{p}|^2-m^2+i\epsilon}\right]^n \\ &= \frac{1}{2\beta}\sum_{a=-\infty}^{\infty}\int\frac{d^3p}{(2\pi)^3}\ln\left[\omega^2+\omega_a^2\right] + \phi_b\text{-independent terms} \end{aligned} \tag{4.37}$$

with $\omega^2 = |\vec{p}|^2 + m^2(\phi_b)$. Computing the infinite sum and keeping only the ϕ_b-dependent terms, one obtains [51]

$$V_{\text{eff}}^{\beta,1}(\phi_b) = \int\frac{d^3p}{(2\pi)^3}\left(\frac{\omega}{2}+\frac{1}{\beta}\ln\left[1-e^{-\beta\omega}\right]\right), \tag{4.38}$$

where it can be shown [51], via the residue theorem and a Wick rotation, that the β-independent part is nothing but the effective potential $V_{\text{eff}}^1(\phi_b)$ that one found in Eq. (4.17):

$$\int\frac{d^3p}{(2\pi)^3}\frac{\omega}{2} = \frac{1}{2}\int\frac{d^4p_E}{(2\pi)^4}\ln\left[p_E^2+m^2(\phi_b)\right] \tag{4.39}$$

$\Pi_1 = -12$ 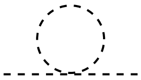

Figure 4.3: One-loop self-energy diagram.

Regarding the β-dependent part of Eq. (4.38), one can massage it using spherical coordinates and the change of variable $x = \beta|\vec{p}|$, to obtain the thermal part V_T in Eq. (4.1):

$$V_T(\phi_b) \equiv \int \frac{d^3p}{(2\pi)^3} \frac{1}{\beta} \ln\left[1 - e^{-\beta\omega}\right] = \frac{1}{2\pi^2\beta^4} J_B[\beta^2 m^2(\phi_b)] \tag{4.40}$$

$$\text{with } J_B\left[\beta^2 m^2(\phi_b)\right] \equiv \int_0^\infty dx\, x^2 \ln\left[1 - e^{-\sqrt{x^2+\beta^2 m^2(\phi_b)}}\right]. \tag{4.41}$$

More generally, for the Standard Model, the one-loop β-dependent part is

$$V^{\beta,1}_{\text{eff, SM}} \supset V_T^{\text{SM}}(\phi_b) \equiv \frac{1}{2\pi^2\beta^4} \sum_i n_i J_{B/F}[\beta^2 m_i^2(\phi_b)] \tag{4.42}$$

$$\text{with } J_{B/F}\left[\beta^2 m_i^2(\phi_b)\right] \equiv \int_0^\infty dx\, x^2 \ln\left[1 \mp e^{-\sqrt{x^2+\beta^2 m_i^2(\phi_b)}}\right], \tag{4.43}$$

with $i \in \{W, Z, h, G_0, G^\pm, t\}$, $m_i^2(\phi_b)$ the eigenvalues of the field-dependent mass matrix and $J_{B/F}\left[\beta^2 m_i^2(\phi_b)\right]$, respectively, the thermal function for bosons ($-$) and fermions ($+$). It is common to expand these thermal functions in the limit of high temperature $\left|\frac{m^2(\phi_b)}{T^2}\right| \ll 1$, thus obtaining [58]

$$\begin{aligned} J_B^{\text{high-}T}\left(\frac{m^2(\phi_b)}{T^2}\right) &\simeq -\frac{\pi^4}{45} + \frac{\pi^2}{12}\frac{m^2(\phi_b)}{T^2} - \frac{\pi}{6}\left(\frac{m^2(\phi_b)}{T^2}\right)^{3/2} \\ &\quad - \frac{1}{32}\left(\frac{m^2(\phi_b)}{T^2}\right)^2 \ln\left[\frac{m^2(\phi_b)/T^2}{a_b}\right], \end{aligned} \tag{4.44}$$

$$J_F^{\text{high-}T}\left(\frac{m^2(\phi_b)}{T^2}\right) \simeq \frac{7\pi^4}{360} - \frac{\pi^2}{24}\frac{m^2(\phi_b)}{T^2} - \frac{1}{32}\left(\frac{m^2(\phi_b)}{T^2}\right)^2 \ln\left[\frac{m^2(\phi_b)/T^2}{a_f}\right], \tag{4.45}$$

where a_b and a_f are constants defined in [58]. Note that these two expressions mainly differ by the presence of a cubic term in ϕ_b for bosons while such a term is absent for fermions. We will look at this cubic term more closely in the coming subsection.

4.2.2 Daisy resummation

Returning to the ϕ^4 theory, the one-loop correction to the two-point function is diagrammatically defined by the one-loop self-energy diagram depicted in Fig. 4.3 [55]. Using TQFT Feynman rules (4.36), this translates into

$$\begin{aligned} \Pi_1 &= -12\left(-i\frac{\lambda}{4!}\right) iT \sum_{a=-\infty}^{+\infty} \int \frac{d^3p}{(2\pi)^3} \frac{1}{-\omega_a^2 - |\vec{p}|^2 - m^2} \\ &= \frac{\lambda}{2} T \sum_{a=-\infty}^{+\infty} \int \frac{d^3p}{(2\pi)^3} \frac{1}{\omega_a^2 + \omega^2}. \end{aligned} \tag{4.46}$$

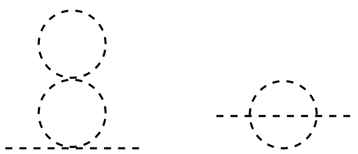

Figure 4.4: Two-loop corrections to the mass. The left diagram is the figure-eight diagram while the right one is the sunset diagram.

Again, by computing the infinite sum, one eventually obtains a T-independent and a T-dependent part. The former gives rise to UV divergences which were already taken care of by a mass counterterm (when constructing the Coleman-Weinberg potential in the previous section), such that the renormalised part vanishes, thus leaving the $T = 0$ mass m unchanged [55, 59]. The renormalised Π_1 is thus only given by its T-dependent part [55]:

$$\Pi_1^{\text{ren}} = \frac{\lambda}{2}\int \frac{d^3p}{(2\pi)^3}\frac{1}{\omega}\frac{1}{e^{\omega/T}-1}. \tag{4.47}$$

Working in the high temperature regime $m/T \ll 1$, one can consider the massless limit $m \to 0$ ($\omega \to |\vec{p}|$) in (4.47), and obtain, using spherical coordinates,

$$\begin{aligned}\Pi_1^{\text{ren}} &= \frac{\lambda}{4\pi^2}\int_0^\infty d|\vec{p}|\frac{|\vec{p}|}{e^{|\vec{p}|/T}-1}\\ &= \frac{\lambda T^2}{24},\end{aligned} \tag{4.48}$$

where one used the change of variable $x = |\vec{p}|/T$ and the relation between the Riemann zeta function $\zeta(s)$ and the gamma function $\Gamma(s)$ for $\text{Re}(s) > 1$ [56]:

$$\begin{aligned}&\int_0^\infty dx\frac{x^{s-1}}{e^x-1} = \zeta(s)\Gamma(s)\\ \Longleftrightarrow &\int_0^\infty dx\frac{x}{e^x-1} = \frac{\pi^2}{6} \qquad \text{for } s=2.\end{aligned} \tag{4.49}$$

At next-loop order one obtains two diagrams depicted in Fig. 4.4: the figure-eight (or one-petal-daisy) and sunset diagram. The former scales as λ^2T^3/m, while the latter scales as λ^2T^2 [58]. Therefore the first diagram is more important by a factor T/m, which is large in the high-temperature limit. At each loop order, it can be shown by dimensional analysis that the dominant contribution originates from daisy diagrams (also called ring diagrams) [58]. This is why one only considers them in the below analysis.

A N-loop daisy diagram with $N-1$ petals translates into [55]

$$-(2\times 3!)^N$$

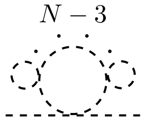

$$= 12\frac{\lambda}{4!}T\sum_{a=-\infty}^{+\infty}\int\frac{d^3p}{(2\pi)^3}[-\Pi_1]^{N-1}\mathcal{D}_0(\omega_a,\vec{p})^N \tag{4.50}$$

$$\text{with } \mathcal{D}_0(\omega_a,\vec{p}) \equiv \frac{1}{\omega_a^2+\omega^2} = \frac{1}{\omega_a^2+|\vec{p}|^2+m^2}, \tag{4.51}$$

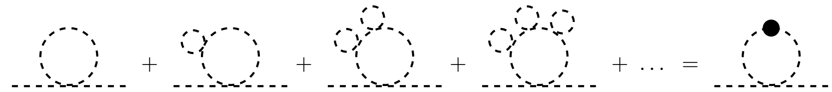

Figure 4.5: Daisy resummation. Parwani resummation methods considers any Matsubara mode in the central loop of the daisy, while Arnold-Espinosa methods resums only daisy diagrams with the central loop being the $a = 0$ Matsubara bosonic mode.

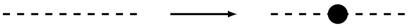

Figure 4.6: Daisy resummation. Replacement of the free finite-temperature two-point function by the dressed one.

where the combination $C_4^2 = 3!$ comes from choosing two legs among the four legs from the four-point vertex and connecting them to make a petal. The factor 2 comes from the two ways to connect the two remaining legs to the adjacent vertices on both sides. Note that for $N = 1$ (no petals), one recovers the one-loop self-energy diagram from Fig. 4.3, as expected.

In the massless limit, while each petal Π_1 is IR safe, the contribution from the main loop yields an IR divergence for the bosonic mode $\omega_a = 0$:

$$\int d^3p\, \mathcal{D}_0^N \sim \int d|\vec{p}|\frac{1}{|\vec{p}|^{2(N-1)}}. \tag{4.52}$$

This IR divergence from the $a = 0$ bosonic Matsubara mode in the main loop arises for $N > 1$, that is for the presence of at least one petal. The perturbative expansion breaks down as the IR divergence becomes worse as one goes to higher-loop order, that is when one adds more petals. One can solve this problem by considering all these daisy diagrams and resumming them (see Fig. 4.5); one then obtains a finite result as can be shown in the following:

$$\begin{aligned}\sum_{N=1}^{\infty}[-\Pi_1]^{N-1}\mathcal{D}_0^N &= \sum_{N=0}^{\infty}[-\Pi_1]^N\mathcal{D}_0^{N+1}\\ &= \mathcal{D}_0\sum_{N=0}^{\infty}[-\Pi_1\mathcal{D}_0]^N\\ &= \mathcal{D}_0\frac{1}{1+\Pi_1\mathcal{D}_0}\\ &= \frac{1}{\mathcal{D}_0^{-1}+\Pi_1}.\end{aligned} \tag{4.53}$$

The result of the daisy resummation depicted in Fig. 4.5 is then

$$\Pi = -12$$

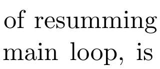

$$= \frac{\lambda}{2}T\sum_{a=-\infty}^{+\infty}\int\frac{d^3p}{(2\pi)^3}\frac{1}{\omega_a^2+\omega^2+\Pi_1}. \tag{4.54}$$

This way of resumming daisy diagrams, irrespective of the Matsubara mode in the main loop, is known as Parwani resummation method [60]. Then, comparing Eq. (4.54) with Eq. (4.46), one clearly sees that daisy resummation simply amounts to shift to mass $m^2 \to m^2 + \Pi_1$, that is to replace the propagator with the dressed one (see Fig. 4.6). The so-called

Debye mass or thermal mass Π_1 regularises the IR divergence occurring in the massless limit $m = 0$ for the zero Matsubara bosonic mode $\omega_a = 0$. Regarding fermions, the $a = 0$ Matsubara mode is non-zero (see Eq. (4.36)) and acts as an IR regulator, thereby there is no need to consider the Debye mass of fermions.

The value of Π_1 found in Eq. (4.48) can also be easily obtained for scalars by taking the second derivative of V_T (see Eq. (4.42)) in the high-temperature expansion, using Eqs. (4.44) and (4.45). In that limit the thermal part of the effective potential is

$$\begin{aligned} V^B_{\text{high-}T} &\simeq \frac{T^4}{2\pi^2}\sum_i n_i \left[-\frac{\pi^4}{45} + \frac{\pi^2}{12}\frac{m_i^2(\phi_b)}{T^2}\right], \\ &= \sum_i n_i \left[-\frac{\pi^4}{90}T^4 + \frac{T^2}{24}m_i^2(\phi_b)\right] \qquad (4.55) \\ V^F_{\text{high-}T} &\simeq \frac{T^4}{2\pi^2}\sum_i n_i \left[\frac{7\pi^4}{360} - \frac{\pi^2}{24}\frac{m_i^2(\phi_b)}{T^2}\right] \\ &= \sum_i n_i \left[\frac{7\pi^4}{720}T^4 - \frac{T^2}{48}m_i^2(\phi_b)\right], \qquad (4.56) \end{aligned}$$

for bosons and fermions, respectively. The thermal mass for scalars can then be found by computing the second derivative of $V_{\text{high}T} \equiv V^B_{\text{high-}T} + V^F_{\text{high-}T}$, keeping only the ϕ_b-independent part:

$$\begin{aligned} \Pi_1^{\text{ren}} &= \left.\frac{\partial^2 V_{\text{high-}T}}{\partial \phi_b^2}\right|_{\phi_b=0} \\ &= \frac{T^2}{24}\sum_B n_B \left.\frac{\partial^2 m_B^2(\phi_b)}{\partial\phi_b^2}\right|_{\phi_b=0} - \frac{T^2}{48}\sum_F n_F \left.\frac{\partial^2 m_F^2(\phi_b)}{\partial\phi_b^2}\right|_{\phi_b=0}. \qquad (4.57) \end{aligned}$$

Applying Eq. (4.57) to the field-dependent mass $m^2(\phi_b) = m^2 + \lambda\phi_b^2/2$ from the ϕ^4 theory (see Eq. (4.18)), one obtains $\Pi_1^{\text{ren}} = \lambda T^2/24$ as in Eq. (4.48).

The same technique can be applied in the Standard Model to compute the Debye mass of the Higgs and Goldstone fields:

$$\begin{aligned} \Pi_\mu^{\text{SM}} &= \frac{T^2}{24}\frac{\partial^2}{\partial\phi_b^2}\left[6m^2_{W^\pm}(\phi_b) + 3m_Z^2(\phi_b) + m_h^2(\phi_b) + 3m_G^2(\phi_b)\right. \\ &\qquad \left.\left. -\frac{1}{2}\times(-12)m_t^2(\phi_b)\right]\right|_{\phi_b=0} \\ &= \frac{T^2}{16}\left(3g_2^2 + g_1^2 + 8\lambda + 4y_t^2\right). \qquad (4.58) \end{aligned}$$

Therefore the daisy resummation applied to the Higgs and Goldstone fields consists in shifting the mass parameter from Eq. (4.21) as $-\mu^2 \to -\mu^2 + \Pi_\mu^{\text{SM}}$. This yields the following thermal masses:

$$m_h^2(\phi_b, T) = -\mu^2 + \frac{T^2}{16}\left(3g_2^2 + g_1^2 + 8\lambda + 4y_t^2\right) + 3\lambda\phi_b^2, \qquad (4.59)$$

$$m_G^2(\phi_b, T) = -\mu^2 + \frac{T^2}{16}\left(3g_2^2 + g_1^2 + 8\lambda + 4y_t^2\right) + \lambda\phi_b^2. \qquad (4.60)$$

The Debye masses for the *longitudinal* mode of electroweak gauge bosons is given by the eigenvalues of the following field-and-temperature-dependent mass matrix in the gauge basis [59, 61]

$$m_L^2(\phi_b, T) = \begin{pmatrix} g_2^2 & 0 & 0 & 0 \\ 0 & g_2^2 & 0 & 0 \\ 0 & 0 & g_2^2 & -g_1 g_2 \\ 0 & 0 & -g_1 g_2 & g_1^2 \end{pmatrix} \frac{\phi_b^2}{4} + \begin{pmatrix} g_2^2 & 0 & 0 & 0 \\ 0 & g_2^2 & 0 & 0 \\ 0 & 0 & g_2^2 & 0 \\ 0 & 0 & 0 & g_1^2 \end{pmatrix} \frac{11}{6} T^2. \tag{4.61}$$

The thermal mass of $W_L^\pm$ is thus

$$m_{W_L^\pm}^2 = \frac{g_2^2}{4}\phi_b^2 + \frac{11}{6} g_2^2 T^2, \tag{4.62}$$

while the thermal masses of Z_L and γ_L are given by

$$\begin{aligned} \left.\begin{array}{l} m_{Z_L}^2(\phi_b, T) \\ m_{\gamma_L}^2(\phi_b, T) \end{array}\right\} &= \frac{1}{2}\left[\left(\frac{\phi_b^2}{4} + \frac{11}{6}T^2\right)(g_1^2 + g_2^2)\right. \\ &\qquad \left. \pm \sqrt{\frac{g_1^2 g_2^2}{4}\phi_b^2 + \left(\frac{\phi_b^2}{4} + \frac{11}{6}T^2\right)^2 (g_1^2 - g_2^2)^2}\right] \\ &= \frac{1}{2}\left[m_Z^2(\phi_b) + \Xi_Z T^2 \pm \sqrt{\Delta^2(\phi_b, T)}\right], \end{aligned} \tag{4.63}$$

$$\text{with } \Delta^2(\phi_b, T) \equiv \frac{4 g_1^2 g_2^2}{(g_1^2 + g_2^2)^2} m_Z^4(\phi_b) + (m_Z^2(\phi_b) + \Xi_Z T^2)^2 \left(\frac{g_1^2 - g_2^2}{g_1^2 + g_2^2}\right)^2 \tag{4.64}$$

$$\text{and } \Xi_Z \equiv \frac{11}{6}(g_1^2 + g_2^2), \tag{4.65}$$

where $m_{Z_L}^2(\phi_b, T)$ is given by the "+" solution, while $m_{\gamma_L}^2(\phi_b, T)$ is given by the "−" one. One directly sees that in the limit of zero temperature one recovers $m_{Z_L}^2(\phi_b, T = 0) = m_Z^2(\phi_b)$ and $m_{\gamma_L}^2(\phi_b, T = 0) = m_\gamma^2(\phi_b) = 0$, given that this limit yields $\Delta^2(\phi_b, T = 0) = m_Z^4(\phi_b)$. As explained above, one does not consider the thermal mass of fermions because the antiperiodicity of their thermal Green functions provides a non-vanishing Matsubara mode $a = 0$. As for transverse gauge bosons, they do not obtain a thermal mass at one-loop order [62, 63].[5]

Finally, let us mention another resummation method, in addition to Parwani one: the Arnold-Espinosa thermal resummation method. It consists in resumming daisy diagrams with the main loop being only the zero bosonic Matsubara mode. When applying the mass shift, depicted in Fig. 4.6, in

---

[5] Transverse modes of the photon never obtain a thermal mass by gauge invariance [64, 65].

$V_{\text{eff}}^{\beta,1}$ only for the $a = 0$ bosonic Matsubara mode, one obtains

$$\begin{aligned}
V_{\text{eff}}^{\beta,1}(m^2(\phi_b), T) &= \frac{T}{2}\sum_{a=-\infty}^{+\infty}\int \frac{d^3p}{(2\pi)^3}\ln\left[\omega_a^2+\omega^2\right] \\
&\longrightarrow \frac{T}{2}\sum_{a\neq 0}\int \frac{d^3p}{(2\pi)^3}\ln\left[\omega_a^2+\omega^2\right] + \frac{T}{2}\int \frac{d^3p}{(2\pi)^3}\ln\left[\omega^2+\Pi_1\right] \\
&= \frac{T}{2}\sum_{a=-\infty}^{+\infty}\int \frac{d^3p}{(2\pi)^3}\ln\left[\omega_a^2+\omega^2\right] \\
&\quad + \frac{T}{2}\int \frac{d^3p}{(2\pi)^3}\left(\ln\left[\omega^2+\Pi_1\right]-\ln\left[\omega^2\right]\right) \\
&= V_{\text{eff}}^{\beta,1}(m^2(\phi_b), T) \\
&\quad + \frac{T}{4\pi^2}\int d|\vec{p}|\ |\vec{p}|^2\left(\ln\left[|\vec{p}|^2+m^2(\phi_b)+\Pi_1\right]\right. \\
&\qquad\qquad \left. -\ln\left[|\vec{p}|^2+m^2(\phi_b)\right]\right) \\
&= V_{\text{eff}}^{\beta,1}(m^2(\phi_b), T) + V_{\text{ring}}(m^2(\phi_b), T),
\end{aligned} \tag{4.66}$$

$$\text{with } V_{\text{ring}}(m^2(\phi_b), T) \equiv -\frac{T}{12\pi}\left(\left[m^2(\phi_b)+\Pi_1\right]^{3/2}-\left[m^2(\phi_b)\right]^{3/2}\right), \tag{4.67}$$

where the next-to-last equality is obtained via

$$\int_0^\infty dx\ x^2\ln\left[x^2+c\right] = -\frac{\pi}{3}c^{3/2}, \tag{4.68}$$

where one dropped the infinite contributions as well as the imaginary part[6] in the case of $c < 0$.

Eq. (4.68) puts in evidence that the cubic term $[m^2(\phi_b)]^{3/2}$ arises from the zero bosonic Matsubara mode and explains why such a term is absent in the high-temperature expansion of the fermionic thermal function (4.45), since the zero fermionic mode does not vanish: $\omega_0^F = T/\pi \neq 0$. Indeed, in the high-temperature regime $m/T \ll 1$, while for fermions one has the term $\ln\left[(\omega_0^F)^2+\omega^2\right] = \ln\left[T^2/\pi^2+|\vec{p}|^2+m^2\right] \simeq \ln\left[(\omega_0^F)^2+|\vec{p}|^2\right]$, which is independent of m, on the contrary, for bosons, one cannot neglect the mass m and one obtains $\ln\left[(\omega_0^B)^2+\omega^2\right] = \ln\left[|\vec{p}|^2+m^2\right]$.

As explained in [58], under the assumption that the high-temperature regime is valid, the Parwani[7] and Arnold-Espinosa resummation methods coincide (up to ϕ_b-independent terms) at one-loop order:

$$\begin{aligned}
V_{\text{CW}}(m^2(\phi_b)+\Pi, T) + V_{\text{high-}T}(m^2(\phi_b)+\Pi, T) \simeq\ & V_{\text{CW}}(m^2(\phi_b)) \\
&+ V_{\text{high-}T}(m^2(\phi_b), T) \\
&+ V_{\text{ring}}(m^2(\phi_b), T).
\end{aligned} \tag{4.69}$$

---

[6] This imaginary part can be safely dropped as the process of phase transition, which is what concerns us in the present thesis, is essentially impacted by the real part of the effective potential [53, 66].

[7] Note that when resumming daisy diagrams, one replaces the internal lines in Fig. 4.2 by dressed finite-temperature propagators, as in Fig. 4.6. Then, since $V_{\text{eff}}^{\beta,1}$ contains both V_{CW} and V_T, this explains why the thermal mass resummation $m^2(\phi_b) \to m^2(\phi_b) + \Pi_1$ applies to both of them.

However, adding V_{ring} consists in resumming daisy diagrams only for the zero-bosonic Matsubara mode in the main loop, thus making the mass shift $m^2(\phi_b) \to m^2(\phi_b) + \Pi_1$ only for the zero bosonic mode, which is considered as the only important (critically dominant) mode in the high-temperature regime as it leads to IR divergence without the regulator Π_1. Put another way, only shifting the mass for the zero bosonic mode implies that one is in the high-temperature regime, as otherwise there is no reason to prioritise this mode specifically. If instead of $V_{\text{high-}T}$ above one wants to use V_T (as in Arnold-Espinosa method (4.66)), to deal with situations outside of the high-temperature regime, then the justification of only considering the zero-mode as the most important one, by adding V_{ring}, is not valid anymore, as one is no longer in the high-temperature regime. Therefore, in the rest of this thesis, one will only consider the Parwani resummation method.[8]

An important remark is that in the high-temperature limit one can Taylor expand $[m^2(\phi_b) + \Pi_1]^{3/2} = \Pi_1^{3/2}[1 + m^2(\phi_b)/\Pi_1]^{3/2}$ in $V_{\text{ring}}(m^2(\phi_b), T)$ and obtain

$$V_{\text{ring}}(m^2(\phi_b), T) \simeq -\frac{T}{12\pi}\left(\Pi_1^{3/2} + \frac{3}{2}\Pi_1^{1/2} m^2(\phi_b) - m^2(\phi_b)^{3/2}\right), \quad (4.70)$$

where the cubic term $\frac{T}{12\pi} m^2(\phi_b)^{3/2}$ is exactly canceled by the cubic contribution $-\frac{T}{12\pi} m^2(\phi_b)^{3/2}$ from $V_{\text{high-}T} \sim \frac{T^4}{2\pi^4} J^B_{\text{high-}T}$ (see Eq. (4.44)). Then since *transverse* gauge bosons have $\Pi_1 = 0$, then $V_{\text{ring}}(m^2(\phi_b), T)$ vanishes and the cubic term from $V_{\text{high-}T}$ survives. Therefore, having a theory with scalars coupled to gauge bosons can help to generate a barrier in the effective potential and thus to trigger a first-order phase transition [68].

As a final note, let us mention that this traditionally used one-loop thermally corrected potential $V_{\text{eff}}(m^2(\phi_b), T)$, built throughout this section, suffers from several theoretical uncertainties that it is worth mentioning, as it can modify the prediction of the stochastic gravitational-wave background signal. While the $T = 0$ one-loop effective potential $V_0 + V_{\text{CW}}$, with V_0 containing running couplings, is essentially independent of the renormalisation scale μ, the one-loop thermally-corrected potential $V_0 + V_{\text{CW}} + V_T$ can only be μ-independent if one considers two-loop diagrams [69]. Moreover, ignoring the running of couplings can also impact the predicted GW signal [70]. Then, the effective potential is only gauge-independent at its extrema, while the field value that extremises it (like the VEV) are gauge-dependent. However a numerical minimisation to find the VEV provides a gauge-dependent value of the effective potential at this VEV [71, 72]. Nevertheless, there exist different approaches to obtain a gauge-independent effective potential [71, 73, 74]. Finally, the dependence on the subtraction scheme may induce discrepancies in the computed GW signal. A comparison between the two most used renormalisation schemes, namely the on-shell and $\overline{\text{MS}}$ scheme can be found in [75, 76]. Taking these theoretical uncertainties into account is beyond the scope of the present manuscript.

---

[8] In practice the numerical difference between these two methods is minor at one-loop level [58, 67].

Chapter 5

Cosmic phase transitions

In the Standard Model, the EW phase transition is a crossover (a smooth transition) and thus does not generate a stochastic gravitational-wave background. In this thesis, we are interested in BSM theories in which this cosmic phase transition becomes first-order. A first-order cosmic phase transition is essentially similar to what is happening in the case of a superheated fluid. This fluid is still in the liquid phase although its temperature is beyond its boiling point. It is therefore in a metastable state, because a large enough external perturbation would make the system going to a lower energy (stable) state, through nucleation and expansion of bubble of the new phase: the vapor phase. This phase transition could also happen spontaneously due to thermodynamic fluctuations as one increases the temperature. If the radius of the bubble is lower than the critical radius, then the outward pressure inside this bubble of the new phase is insufficient to overcome the inward pressure from the external environment; the bubble consequently shrinks and eventually disappears. On the other hand, the nucleation of bubbles with radius bigger than the critical one will lead to their expansion, thus converting the metastable superheated phase into the stable vapor phase.

The aim of this thesis is to study cosmic phase transitions in the early Universe (at the EW scale), therefore at a temperature such that thermal effects cannot be neglected. Let us see first how it works at zero temperature, after which the extension to non-zero temperatures is straightforward.

5.1 Quantum tunneling

This section closely follows Coleman's paper [77]. Let us consider a typical Lagrangian density

$$\mathcal{L} = \frac{1}{2}(\partial_\mu \phi)^2 - V(\phi) = \frac{1}{2}\left(\frac{\partial \phi}{\partial t}\right)^2 - \frac{1}{2}(\vec{\nabla}\phi)^2 - V(\phi), \tag{5.1}$$

whose potential $V(\phi)$ is depicted in the left panel of Fig. 5.1. This potential possesses two minima, one at the *false* vacuum ϕ_F and one at the *true* vacuum ϕ_T. The potential is shifted so that $V(\phi_F) = 0$. Moreover it possesses another zero at ϕ_M, as shown in Fig. 5.1. Although the false vacuum is classically stable, it will eventually decay by quantum tunneling, thus making it a metastable ground state. After the Wick rotation $t \to \tau \equiv it$,

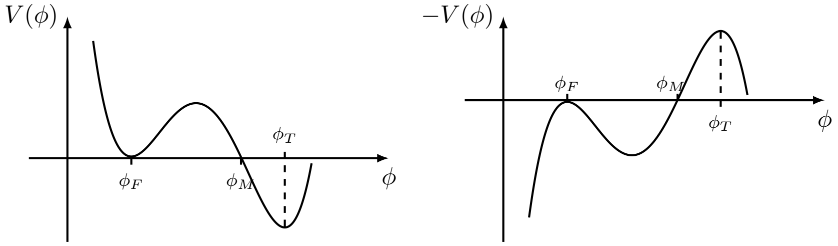

Figure 5.1: Left: Potential $V(\phi)$ with one (local) metastable minimum or false vacuum at ϕ_F and one (global) stable minimum or true vacuum at ϕ_T. At both ϕ_F and ϕ_M, the potential vanishes. Right: Inverted potential $-V(\phi)$.

one obtains the Euclidean Lagrangian density

$$\mathcal{L}_E = \frac{1}{2}\left(\frac{\partial\phi}{\partial\tau}\right)^2 + \frac{1}{2}\left(\vec{\nabla}\phi\right)^2 + V(\phi) \tag{5.2}$$

associated to the inverted potential $-V(\phi)$. The Euler-Lagrangian equations applied to $\mathcal{L}_E$ yield the following equation of motion:

$$\left(\frac{\partial^2}{\partial\tau^2} + \nabla^2\right)\phi = \frac{dV}{d\phi}. \tag{5.3}$$

The solution of this equation, which in addition respects the following boundary conditions

$$\lim_{\tau\to\pm\infty}\phi(\tau,\vec{x}) = \phi_F \quad \text{and} \quad \left.\frac{\partial\phi}{\partial\tau}\right|_{\tau=0} = 0, \tag{5.4}$$

is called the *bounce* $\phi(\tau,\vec{x})$. This name comes from the analogy with the motion of a particle bouncing off in the inverted potential (see below): the particle initially starts at ϕ_F at $\tau \to -\infty$, reaches a point where its velocity vanishes, and then bounces back to reach again ϕ_F at $\tau \to +\infty$.

The Euclidean action S_E is defined as

$$S_E \equiv \int d^4x_E \mathcal{L}_E = \int d\tau d^3x \left[\frac{1}{2}\left(\frac{\partial\phi}{\partial\tau}\right)^2 + \frac{1}{2}\left(\vec{\nabla}\phi\right)^2 + V(\phi)\right]. \tag{5.5}$$

The integrand $\mathcal{L}_E$ should vanish at boundaries to make S_E finite. This happens if, in addition to the conditions (5.4), the bounce also satisfies

$$\lim_{|\vec{x}|\to\pm\infty}\phi(\tau,\vec{x}) = \phi_F. \tag{5.6}$$

Indeed, since ϕ_F is a constant both in τ and $|\vec{x}|$ and $V(\phi_F) = 0$, then one obtains

$$\lim_{\tau,|\vec{x}|\to\pm\infty}\mathcal{L}_E(\phi) = \mathcal{L}_E(\phi_F) = 0. \tag{5.7}$$

In the following, we will show that if one supposes an $O(4)$-symmetric version of Eqs. (5.3)-(5.6), one can always find a ($O(4)$-symmetric[1]) solution, the bounce $\phi(\rho)$, with $\rho \equiv \sqrt{\tau^2 + |\vec{x}|^2}$. This solution is depicted in the panel (a) in Fig. 5.4.

---

[1] It has been proven in [78] that the $O(4)$-symmetric bounce yields the lowest Euclidean action; all other bounce solutions can thus be ignored.

If ϕ is invariant under four-dimensional rotation in the Euclidean space, one can rewrite the Euclidean action (5.5), using spherical coordinates, as

$$S_E = 2\pi^2 \int_0^\infty d\rho\ \rho^3 \left[\frac{1}{2} \left(\frac{d\phi}{d\rho} \right)^2 + V(\phi) \right], \tag{5.8}$$

with the solid angle $\int d\Omega_d = 2\pi^{d/2}/\Gamma(d/2) = 2\pi^2$ for $d = 4$. The Euler-Lagrange equation then yields

$$\frac{d^2\phi}{d\rho^2} + \frac{3}{\rho}\frac{d\phi}{d\rho} = \frac{dV}{d\phi}. \tag{5.9}$$

The boundary conditions (5.4) and (5.6) merge into

$$\lim_{\rho \to \pm\infty} \phi(\rho) = \phi_F, \tag{5.10}$$

and in order for the second term in Eq. (5.9) to not diverge at $\rho = 0$, one additionally requires

$$\left. \frac{d\phi}{d\rho} \right|_{\rho=0} = 0. \tag{5.11}$$

If in Eq. (5.9), one interprets ϕ as the position of a particle and ρ as the time coordinate, then it describes the motion of a particle in the potential $-V$ damped by a friction term decreasing with time. For a given initial position $\phi(0)$ where the particle is released with no initial velocity by Eq. (5.11), the particle should end its motion at ϕ_F after an infinite amount of time (see Eq. (5.10)) where it becomes at rest (ϕ_F being constant, its derivative vanishes).

If $\phi(0)$ is on the left of ϕ_M in the right panel of Fig. 5.1, then it does not have enough energy E to asymptotically reach ϕ_F; it *undershoots* ϕ_F. Taking the friction into account makes it even worse as it always reduces the energy:

$$\begin{aligned} \frac{dE}{d\rho} &\equiv \frac{d}{d\rho} \left[\frac{1}{2} \left(\frac{d\phi}{d\rho} \right)^2 - V \right] \\ &= \frac{d\phi}{d\rho}\frac{d^2\phi}{d\rho^2} - \frac{dV}{d\phi}\frac{d\phi}{d\rho} \\ &= -\frac{d\phi}{d\rho}\left(\frac{3}{\rho}\frac{d\phi}{d\rho} - \frac{dV}{d\rho} \right) - \frac{dV}{d\phi}\frac{d\phi}{d\rho} \\ &= -\frac{3}{\rho}\left(\frac{d\phi}{d\rho} \right)^2 \leq 0, \end{aligned} \tag{5.12}$$

where Eq. (5.9) has been used in the next-to-last line.

If on the other hand $\phi(0)$ is too close to ϕ_T in $-V$, then it will *overshoot* ϕ_F. It that case, since ϕ is close to ϕ_T, one can linearise Eq. (5.9) by Taylor expanding

$$\frac{dV}{d\phi} \simeq \left. \frac{dV}{d\phi} \right|_{\phi_T} + (\phi - \phi_T) \left. \frac{d^2V}{d\phi^2} \right|_{\phi_T}, \tag{5.13}$$

where the first term vanishes because of ϕ_T being an extremum of V. Using the fact that $d\phi_T/d\rho = 0$, Eq. (5.9) then becomes

$$\left(\frac{d^2}{d\rho^2} + \frac{3}{\rho}\frac{d}{d\rho} - \left.\frac{d^2V}{d\phi^2}\right|_{\phi_T}\right)(\phi - \phi_T) = 0$$

$$\Longleftrightarrow \quad \frac{d^2\varphi}{dr^2} + \frac{3}{r}\frac{d\varphi}{dr} - \varphi = 0 \tag{5.14}$$

$$\text{with} \quad \varphi \equiv (\phi - \phi_T), \quad r \equiv \mu\rho \quad \text{and} \quad \mu^2 \equiv \left.\frac{d^2V}{d\phi^2}\right|_{\phi_T}(\phi - \phi_T). \tag{5.15}$$

The solution of this differential equation is given in terms of the modified Bessel function of the first kind $I_1(r)$. By using then the initial condition (5.11) and φ at $r = 0$, one obtains the solution

$$\varphi(r) = \frac{2\varphi(0)}{r} I_1(r). \tag{5.16}$$

Therefore if $\varphi(0)$ is close to zero, then $\varphi(r)$ becomes close to zero as well, for any r. For a large enough r, the friction (going as r^{-1}) is then suppressed. In consequence, when the particle is released after a long "time" r, since its energy is larger than the one at ϕ_F and there is no friction anymore to diminish it, the particle necessarily overshoots ϕ_F.

By continuity, between these two opposite situations (undershooting and overshooting), one can always find an initial condition $\phi_M < \phi(0) < \phi_T$ so that the particle asymptotically reaches ϕ_F at rest, thereby one can always find an $O(4)$-spherical bounce satisfying the equation of motion.

There are two extreme cases for the bounce solution. The first one is when both minima of the potential are almost degenerate, then the difference between the value of the potential at these minima is small: $V(\phi_F) - V(\phi_T) = \epsilon \ll 1$. In the particle-motion analogy, the particle should wait very close to the true minimum ϕ_T ($\phi(0) \to \phi_T$) to not lose this small excess of energy ϵ by friction. It waits until $\rho = R$, when the friction term is suppressed enough so that the particle can asymptotically reach ϕ_F at rest. The typical bounce in this *thin-wall limit* is depicted in the left panel of Fig. 5.2. One can see in this figure that $\phi(\rho) \simeq \phi_T$ for $0 \leq \rho \leq R$. This bounce solution corresponds to the nucleation of a bubble of radius R. Its value at $\rho \to \pm\infty$ is ϕ_F as expected. A boundary, the bubble wall, separates these two phases. In the thin-wall limit, the width L of this wall is negligible compared to the radius R. Note that the only region where the gradient $d\phi/d\rho$ is non-zero is within this narrow bubble wall. In the opposite case, the thick-wall limit, the particle is dropped from rest already at $\rho = 0$ in order to lose enough energy by friction to asymptotically reach ϕ_F at rest. In that limit, one can see from the right panel of Fig. 5.2 that the bubble wall width is much larger than the radius ($L \gg R$).

The tunneling in these two limits is shown in Fig. (5.3). The left panel represents the case of thin-wall bubbles, where the bubble nucleates with a value close to ϕ_T inside it. The blue particle in the figure tunnels very close to the true vacuum and then classically rolls down via Eq. (5.9) towards it (indicated by the red arrow). The right panel represents the case of thick-wall bubbles, where the blue particle appears far from the true vacuum after tunneling, before classically rolling down towards it.

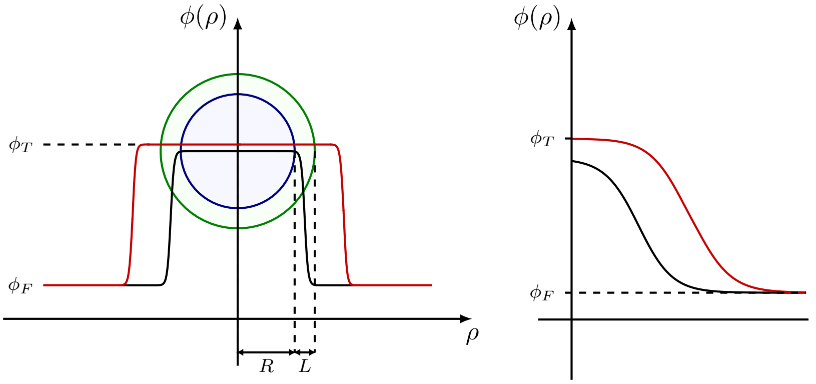

Figure 5.2: Left: Bounce in the thin-wall limit ($R \gg L$). The inside of the bubble corresponds to the true vacuum or (symmetry-)broken phase and is colored in blue, while beyond the bubble wall (colored in green) corresponds to the false vacuum or symmetric phase. The bubble wall width L larger than it should for the readability of the figure. Right: Bounce in the thick-wall limit ($R \ll L$), with $\phi(0) < \phi_T$. In both panels the black bounce is at the nucleation time, while the red one is when the true vacuum is reached after tunneling.

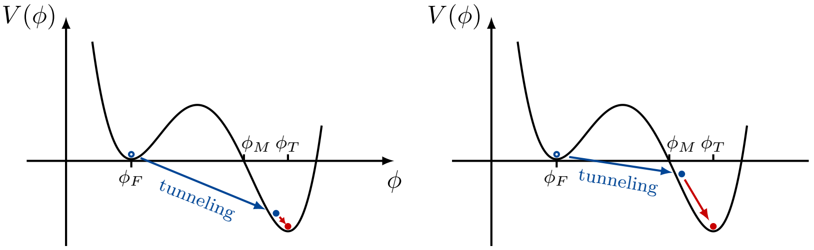

Figure 5.3: Left: Tunneling in the thin-wall limit. Right: Tunneling in the thick-wall limit. Bubble nucleates (filled blue dot) and classically rolls down (red arrow) to the true vacuum (red dot). In the case of a thin-wall limit, it nucleates close to the true vacuum ϕ_T, while it nucleates close to ϕ_M thick-wall limit. Note that in the case of a thin-wall limit, the drawing is exaggerated for the readability as both minima should normally be nearly degenerate. The red point corresponds to the red bounce configuration in Fig. 5.2. The filled blue dot correspond to $\phi(R)$ on the black bounce in Fig. 5.2 in the thin-wall limit and to $\phi(0)$ in the thick-wall limit.

The probability of the false-vacuum decay per unit time Γ is exponentially suppressed by the Euclidean action of the bounce: $\Gamma \sim e^{-}$ details of the how to compute the prefactor is not important here as in practice, one considers a simple approximation of this prefactor obtained by dimensional analysis. For completeness, one nevertheless provides the full form (to show how it is straightforward to obtain the equivalent expression for thermal tunneling in the next section) for the bubble nucleation rate per unit time (or decay rate of false vacuum) per unit volume in the semi-classical limit (thus in the limit of small $\hbar$) [79]:

$$\frac{\Gamma}{V}=\left(\frac{S_E}{2\pi\hbar}\right)^2\left(\frac{\det\left[-\Box_E+\left.\frac{d^2V}{d\phi^2}\right|_{\phi=0}\right]}{\det'\left[-\Box_E+\frac{d^2V}{d\phi^2}\right]}\right)^{1/2} e^{-S_E/\hbar}\left[1+\mathcal{O}(\hbar)\right], \quad (5.17)$$

with $\Box_E \equiv \partial^2_{\tau^2}+\nabla^2$, where $\det'$ means that one omits the zero eigenvalues of $-\Box_E+\frac{d^2V}{d\phi^2}$ and where a contribution $\sqrt{S_E/2\pi\hbar}$ arises from each of the four zero modes (these modes correspond to translational invariance of the bounce along each of the four axes in the Euclidean space).

Note that spatially translated bounces extremise the same Euclidean action, thus for the same Euclidean action S_E, one can obtain many bounces by translation [77]. In order to obtain the total width Γ, one then has to consider

$$\int d^3x\; e^{-S_E}=e^{-S_E}\int d^3x=Ve^{-S_E}, \quad (5.18)$$

which explains why the prefactor in Eq. (5.17) obtains a contribution from the three-dimensional volume V, hence the factor $1/V$ for the decay width Γ.

5.2 Thermal tunneling

As already mentioned in the beginning of Section 4.2, quantum field theory at finite temperature is equivalent to quantum field theory in an Euclidean space with periodicity (for bosons), along the time direction, of period $\beta \equiv 1/T$. Then, while at $T=0$, the solution of the equation of motion is the Euclidean $O(4)$ bounce, then at non-zero $T \ll R^{-1}$, with R the radius of the bubble, one obtains periodic $O(4)$-spherical bubble solutions. For $T \sim R^{-1}$, bubble solutions start to overlap and even more when $T \gg R^{-1}$. Finally in the limit $T \to \infty$, one obtains a cylinder of bubbles. In that case, each time slice, or spatial cross section, is a τ-independent $O(3)$ bubble solution. This evolution of bubble solutions with the temperature is depicted in Fig. 5.4 [80, 81].

For τ-independent bounces, the four-dimensional Euclidean action S_4 in Eq. (5.5) becomes

$$\begin{aligned} S_4 &= \int_0^{1/T} d\tau \int d^3x\left[\frac{1}{2}\left(\vec{\nabla}\phi_b\right)^2+V_{\text{eff}}(\phi_b,T)\right] \\ &= \frac{S_3}{T} \end{aligned} \quad (5.19)$$

with

$$\begin{aligned} S_3 &= \int d^3x\left[\frac{1}{2}\left(\vec{\nabla}\phi_b\right)^2+V_{\text{eff}}(\phi_b,T)\right] \\ &= 4\pi\int_0^\infty d\rho\;\rho^2\left[\frac{1}{2}\left(\frac{d\phi_b}{d\rho}\right)^2+V_{\text{eff}}(\phi_b,T)\right], \end{aligned} \quad (5.20)$$

the three-dimensional Euclidean action of the $O(3)$ bounce, where the last line results from the $O(3)$ symmetry and where this time ρ is defined as $\rho =$

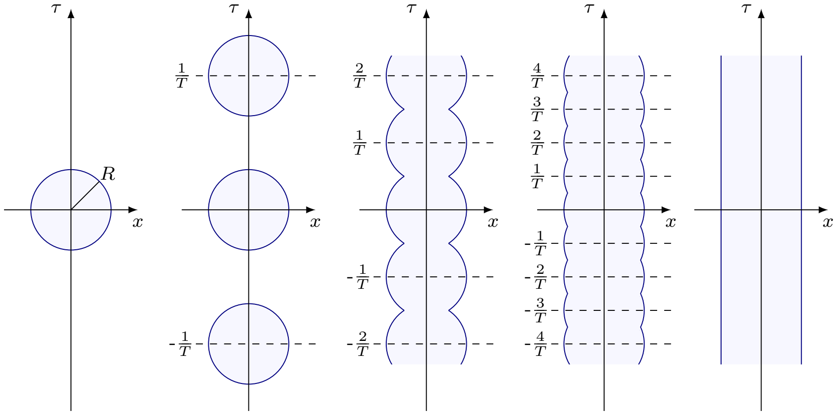

(a) (b) (c) (d) (e)

Figure 5.4: Bidimensional projection of the $O(4)$ bubble solution ϕ of parametric equation $\rho^2 = \tau^2 + |\vec{x}|^2$, for $\rho = R$, for different temperatures T: (a) $T = 0$; (b) $T \ll R^{-1}$; (c) $T \sim R^{-1}$; (d) $T \gg R^{-1}$; (e) $T \to \infty$. The light-blue region (inside the bubbles) corresponds to the true vacuum, while the region outside the bubbles corresponds to the false vacuum. The dark-blue boundary is the bubble wall separating the two phases. To make the picture clear, the bubbles have been drawn with a thin bubble wall compared to bubble radius R though this is not necessarily the case. Figure inspired by the one in [80].

$|\vec{x}|$. Note that in the above equations, thermal effects are taken into account by considering the thermally-corrected effective potential $V_{\text{eff}}(\phi_b, T)$ derived in the previous chapter,[2] where the bounce is the background field $\phi_b = \langle\phi\rangle$. Equivalently, when computing the decay rate of the false vacuum at zero temperature, one can use the result from the previous section (see Eq. (5.17)) by replacing $V(\phi)$ with the zero-temperature effective potential $V_{\text{eff}}(\phi_b, T = 0)$ to take quantum corrections into account.[3] The derived equation of motion is then simply

$$\frac{d^2\phi_b}{d\rho^2} + \frac{2}{\rho}\frac{d\phi_b}{d\rho} = \frac{dV_{\text{eff}}(\phi_b, T)}{d\phi_b}. \tag{5.21}$$

The final expression for the decay rate of the false vacuum per unit volume Γ/V is obtained from the expression at zero temperature in Eq. (5.17), by expressing the Euclidean action S_4 of the $O(4)$ bounce in terms of the Euclidean action S_3 of the $O(3)$ bounce and by omitting the time

---

[2] As an improvement, one-loop corrections to the kinetic term should also be considered [82, 83].

[3] Note, however, that, although this substitution is commonly done in the literature and in the present thesis, it leads to a double counting as one integrates over the fields twice: once to obtain the effective potential and once leading to the functional determinant in the expression of the false-vacuum decay rate in Eq. (5.17). Moreover this substitution implies promoting the constant background-field ϕ_b to a spacetime dependent field configuration to be able to describe the bounce [72]. This ultimately results in uncertainties in the prediction of the GW signal.

dependence τ [80,81]:

$$\begin{aligned}\frac{\Gamma}{V} &= A(T)\ e^{-S_3/T} \\ &= T\left(\frac{S_3}{2\pi T}\right)^{3/2}\left(\frac{\det\left[-\nabla^2+\frac{d^2V_{\text{eff}}}{d\phi_b^2}\Big|_{\phi_b=0}\right]}{\det'\left[-\nabla^2+\frac{d^2V_{\text{eff}}}{d\phi_b^2}\right]}\right)^{1/2} e^{-S_3/T},\end{aligned} \tag{5.22}$$

where the prefactor T arises from the periodicity of period $1/T$ along the time direction, where $\det'$ denotes the functional determinant omitting the zero eigenvalues of $-\nabla^2+\frac{d^2V_{\text{eff}}}{d\phi^2}$ and where this time a contribution $\sqrt{S_3/2\pi T}$ arises from each of the three zero modes, which corresponds to translational invariance of the bounce along each of the three spatial directions.

In practice, computing the functional determinant in the above equation is a complicated task. Nevertheless, as a good approximation, one can estimate the prefactor $A(T)$ by dimensional analysis. Since one has

$$\frac{d^2V_{\text{eff}}}{d\phi_b^2}\bigg|_{\phi_b=0} = \Pi_1^{\text{ren}} \sim T^2 \tag{5.23}$$

by Eq. (4.57), then one obtains the following expression for the ratio of functional determinants (being the product of an infinite number of eigenvalues):

$$\left(\frac{\det\left[-\nabla^2+\frac{d^2V_{\text{eff}}}{d\phi_b^2}\Big|_{\phi_b=0}\right]}{\det'\left[-\nabla^2+\frac{d^2V_{\text{eff}}}{d\phi_b^2}\right]}\right)^{1/2} \sim \lim_{n\to\infty}\left(\frac{T^{2n}}{T^{2(n-3)}}\right)^{1/2} = T^3, \tag{5.24}$$

thereby one can take $A(T)\sim T^4$ [81,84]. In practice, when computing the decay rate of the false vacuum per unit volume from thermal tunneling, one thus uses

$$\frac{\Gamma}{V} \simeq T^4 e^{-S_3/T}. \tag{5.25}$$

When studying the decay of the false vacuum, one then has to consider both the above $T\neq 0$ result and the $T=0$ result from Eq. (5.17) and take the maximum of these two quantities [85]:

$$\begin{aligned}\frac{\Gamma}{V} &\simeq \max\left[\frac{\Gamma_4}{V},\frac{\Gamma_3}{V}\right] \\ &\sim \max\left[R^{-4}\left(\frac{S_4}{2\pi}\right)^2 e^{-S_4}, T^4\left(\frac{S_3}{2\pi T}\right)^{3/2} e^{-S_3/T}\right] \\ &\sim \max\left[R^{-4}e^{-S_4}, T^4 e^{-S_3/T}\right],\end{aligned} \tag{5.26}$$

where in the case of quantum tunneling, R^{-4} arises by dimensional analysis of the ratio of the functional determinant present in Eq. (5.17), with this time the typical energy scale chosen to be R^{-1}, the inverse of the radius of the nucleating bubble, instead of the temperature T. In this thesis one assumes that at the EW scale temperature is large enough to always have

$\Gamma_3 > \Gamma_4$, thus allowing us to only focus on thermal tunneling when studying EW phase transitions. Note that the formula derived in this section relies on the assumption $T \gg R^{-1}$ as explicitly shown in Fig. 5.4, thus justifying that one has $\Gamma_3 > \Gamma_4$ given the last line in Eq. (5.26).

In the following, one considers the typical thermal evolution of the effective potential in order to define specific temperatures, important for the study of phase transitions. In the Standard Model, the EW phase transition is a crossover, which means that the order parameter, here the VEV, changes very smoothly from a zero (false vacuum) to a non-zero value (true vacuum). On the other hand, a first-order phase transition is characterised by an abrupt change of the order parameter, that is, the VEV discontinuously goes from a vanishing to a non-vanishing value. The intermediate case between these two type of phase transition is a second-order phase transition, as can be seen in the left panel of Fig. 5.5.

Let us now assume a BSM theory in which the EW phase transition is of the first order. Usually, the effective potential $V_{\text{eff}}(\phi_b, T)$ possesses only one minimum centered at the origin in the limit $T \to \infty$.[4] Then, as the temperature decreases, a new local minimum, the EW vacuum, appears but the one at the origin is still global. At the so-called critical temperature T_c, both this new minimum and the one at the origin, separated by a (thermally generated) barrier,[5] are degenerate. Below that temperature, this EW minimum is the newly global minimum of $V_{\text{eff}}(\phi_b, T)$ and it becomes theoretically possible to tunnel from the origin (which is now metastable) to the EW minimum. The phase transition is then characterised by the onset of bubble nucleation at the so-called nucleation temperature T_n (more precisely defined below). The thermal evolution of the effective potential is schematically given in the right panel of Fig. 5.5.

When several bubbles nucleate and expand in a Hubble volume, at some point, some of them will collide with each other, thus creating a cluster of connected bubbles. For a random distribution of bubbles, the critical probability for a random point to be in a bubble defines the percolation threshold. Beyond this critical probability, percolation occurs, which means that an infinitely large connected cluster of (overlapping) bubbles exists. Therefore in our case a path of bubbles is connecting the opposite sides of a box of Hubble volume [92]. It has been numerically shown that for three-dimensional overlapping spheres of equal size, percolation occurs when the probability for a random point to be in a sphere, or equivalently the fraction of space covered by spheres, is around 0.29 [93]. Defining $P(T)$ as the probability, at some temperature T, for a random point to be in the false vacuum, or equivalently not being in bubbles of true vacuum, then the percolation temperature T_p is defined such that $1 - P(T_p) \simeq 0.29$. The probability $P(T)$ is usually expressed as $P(T) = e^{-I(T)}$, where $I(T)$ corresponds to the mean number of bubbles whose centers are within a bubble radius of that random point and whose expression can be for in-

---

[4] Thermal effects usually restore the spontaneously broken symmetry. However, other scenarios do exist, such as the case of symmetry non-restoration [86, 87], where a symmetry, broken at low temperature, is not restored at high temperature or the case of inverse symmetry breaking [88], where a symmetry, not broken at low temperature, is broken at high temperature.

[5] Note that tunneling without a barrier in $V(\phi)$ can happen because what matters is actually to have a barrier in the functional $U[\phi(x)] \equiv \int d^3x[\frac{1}{2}(\vec{\nabla}\phi)^2 + V(\phi)]$ which, in addition to $V(\phi)$, also includes a gradient term [89, 90].

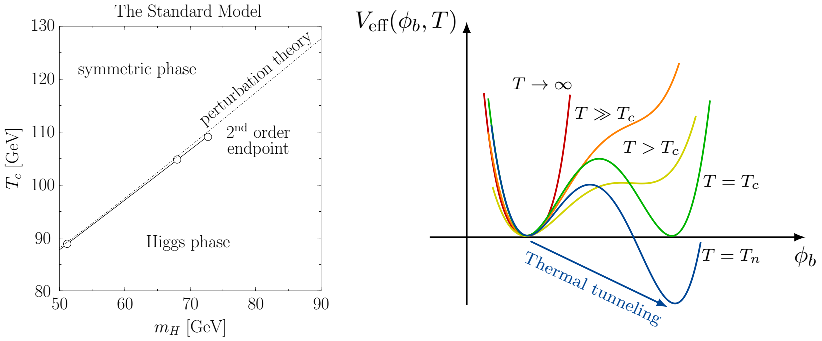

Figure 5.5: Left: In the Standard Model, the EW phase transition is a crossover as it can only be of first order for the Higgs mass satifying $m_H \lesssim 75$ GeV. Initially in the symmetric phase, if for a fixed m_H one goes down in the figure by decreasing the temperature, then if the oblique solid line ($T = T_c$) is crossed, one ends in the broken phase through a first-order phase transition. If, however, this line is not crossed, there is no phase transition, only a crossover. The end point of this solid line signals a second-order phase transition. The three empty points are the result of lattice simulations, while the solid line is a fit through them. This figure is taken from [91]. Right: Thermal evolution of the effective potential. Initially at $T \to \infty$ (red), the effective potential has one minimum. Then, as the temperature decreases, the shape of the effective potential evolves (orange) until a new minimum appears (yellow). At the critical temperature T_c, both minima become degenerate (green). Below that temperature, a thermal phase transition is possible. Finally the effective potential is shown in blue at the nucleation temperature T_n, after which the phase transition completes.

stance found in [94, 95]. Therefore at the percolation temperature, one has $P(T_p) \simeq 0.71$, thus implying $I(T_p) \simeq 0.34$, i.e. at $T = T_p$, 29% of the false vacuum has been converted into the true one. The percolation temperature is usually thought as the temperature at which the phase transition ends, because at percolation time, the phase transition quickly completes.[6] In this thesis, one considers fast phase transitions, therefore with moderate supercooling and without significant reheating; one can thus safely consider $T_n \simeq T_p$ [85, 96, 97], thereby making T_n a crucial parameter for the study of phase transitions in our case. Once the phase transition has ended, the Universe is in the EW minimum and the position of the latter still continues to evolve with temperature until it reaches its zero-temperature value $v \simeq 246$ GeV.

The nucleation temperature T_n is defined as the temperature at which $\frac{\Gamma}{V} H^{-4} \sim \mathcal{O}(1)$, i.e. one bubble of true vacuum nucleates per Hubble time per Hubble volume.[7] Thus, using Eq. (5.25) and $H^2 = 8\pi\rho_{\text{rad}}/(3M_{\text{Planck}}^2)$,

---

[6] Note that the percolation criterion $I(T_p) = 0.34$ is only a sufficient condition in a radiation-dominated Universe, which is commonly assumed. Models with vacuum-domination era requires a modification of the percolation criterion [85].

[7] For bubbles to convert the false vacuum into the true one, the decay rate of the false vacuum should compete with the Hubble expansion rate: $\Gamma \sim H$.

with ρ_{rad} given in Eq. (3.12), one obtains

$$\begin{aligned}
& T_n^4 \, e^{S_3/T_n} = H^4 \\
\Longleftrightarrow \quad & \frac{S_3}{T_n} = -2\ln H^2 + 4\ln T_n \\
\Longleftrightarrow \quad & \frac{S_3}{T_n} = -2\ln\left[\frac{\pi^3}{45 M_{\text{Planck}}^2}\right] - 2\ln g_* - 4\ln T_n \\
\Longleftrightarrow \quad & \frac{S_3}{T_n} \simeq 146 - 2\ln\left[\frac{g_*}{106.75}\right] - 4\ln\left[\frac{T_n}{100\ \text{GeV}}\right] . \qquad (5.27)
\end{aligned}$$

In the literature, it is common for a typical EW phase transition to simply consider the approximate condition $S_3/T_n \simeq 140$ for determining the nucleation temperature T_n.

To conclude, one can ensure that one effectively obtains a first-order phase transition in perturbative analysis, by satisfying the following criterion [9, 98]:

$$\frac{\Delta v}{T_n} \equiv \frac{\sqrt{\sum_i^N \left[v(\phi_2, T_n)_i - v(\phi_1, T_n)_i\right]^2}}{T_n} \geq 1, \qquad (5.28)$$

where the VEV in the false and true vacuum are respectively given by $v(\phi_1, T)$ and $v(\phi_2, T)$ and i indicates the component of the vector v in the N-dimensional field space. This is in addition a condition, coming originally from EW-baryogenesis studies, stating that a first-order phase transition is a strong one [99, 100].

Chapter 6

Stochastic gravitational-wave background

The previous chapter has treated the nucleation and expansion of a *single* vacuum bubble. The signal one expects to observe from a cosmic phase transition originates from the collision of *several* of these bubbles. This results into a stochastic gravitational-wave background that one hopes to detect via future space-based GW detectors. The *stochasticity* of this signal comes from the probabilistic nature of its source: the nucleation of true-vacuum bubbles. This implies that the metric perturbation h_{ij}^{TT} (defined in Section 6.2), responsible for this stochastic GW background, is a random variable and can only be studied statistically [101]. The signal from a stochastic GW background is not coming from a specific location in space but from all directions and results from unresolved events, therefore defining a *background*. The stochastic gravitational-wave background is assumed to be isotropic, although some small anisotropies can be present, similarly to the CMB [102]. Therefore, it essentially does not matter in which direction one is observing it.

In this chapter, we review the important quantities needed to compute the power spectrum of the stochastic GW background, explain how it is generated and show how to claim that such a signal is potentially detectable.

6.1 Key parameters

The bubbles of true vacuum evolve in the cosmic plasma, which can be described by thermodynamical quantities such as the free energy F and pressure p. They are both expressed in terms of the partition function Z_β, defined in Eq. (4.29), as [55, 56]

$$F = -T \ln Z_\beta \quad \text{and} \quad p = -\lim_{V\to\infty} \frac{\partial F}{\partial V} = -\lim_{V\to\infty} \frac{\partial (fV)}{\partial V} = -\lim_{V\to\infty} f, \tag{6.1}$$

with V a finite spatial volume and $f \equiv F/V$ the free energy density. Then it is shown in [56] that

$$\lim_{V\to\infty} f = \lim_{V\to\infty} \frac{F}{V} = V_{\text{eff}}(\phi_b, T), \tag{6.2}$$

therefore leading to

$$p = -V_{\text{eff}}(\phi_b, T). \tag{6.3}$$

The energy density ρ, enthalpy w and entropy density s are, respectively, defined in terms of the pressure p as [103]

$$\rho \equiv T\frac{\partial p}{\partial T} - p, \quad w \equiv T\frac{\partial p}{\partial T}, \quad s \equiv \frac{\partial p}{\partial T}, \tag{6.4}$$

thus implying $w = \rho + p = Ts$ and $\rho = Ts - p$.

In the following, one considers the bag model, which assumes a non-interacting (perfect/ideal) fluid of massless (relativistic) particles with a bag constant ϵ (independent of the temperature) [104–106] and where the pressure in the symmetric and broken phase are, respectively, given by [103, 106, 107]

$$p(T)_{\text{sym}} = \frac{1}{3}a_{\text{sym}}T^4 - \epsilon \quad \text{and} \quad p(T)_{\text{brok}} = \frac{1}{3}a_{\text{brok}}T^4, \tag{6.5}$$

$$\text{with} \;\; a = \frac{3}{4T}\frac{\partial p}{\partial T}. \tag{6.6}$$

From Eq. (6.4) one can then derive the following relations for the energy density:

$$\rho(T)_{\text{sym}} = a_{\text{sym}}T^4 + \epsilon \quad \text{and} \quad \rho(T)_{\text{brok}} = a_{\text{brok}}T^4, \tag{6.7}$$

$$w(T)_{\text{sym}} = \frac{4}{3}a_{\text{sym}}T^4 \quad \text{and} \quad w(T)_{\text{brok}} = \frac{4}{3}a_{\text{brok}}T^4. \tag{6.8}$$

Equations (6.5) and (6.7) are the equations of state in the bag model. In this model ϵ is given by the false-vacuum energy density, with $\epsilon = 0$ in the (equation of state of the) broken phase [103]. In the bag model the sound speed in the plasma, defined as $c_s^2 \equiv dp/d\rho$, takes the value:

$$\begin{aligned} p_{\text{sym}} &= \frac{\rho_{\text{sym}}}{3} - \frac{4}{3}\epsilon, \\ p_{\text{brok}} &= \frac{\rho_{\text{brok}}}{3} \\ \longrightarrow \left(\frac{dp}{d\rho}\right)_{\text{sym}} &= \left(\frac{dp}{d\rho}\right)_{\text{brok}} = \frac{1}{3}, \end{aligned} \tag{6.9}$$

implying that the sound speed in the plasma in both phases is the same and constant in the bag model: $c_s^2 = (c_s^{\text{sym}})^2 = (c_s^{\text{brok}})^2 = 1/3$. This is the value of the speed of sound for a relativistic plasma.

In the ultrarelativistic limit $T/m \gg 1$, the thermal part of the effective potential dominates and one only considers the first term in its high-temperature expansion (see Eqs. (4.55), (4.56)). Therefore the pressure $p = -V_{\text{eff}}(\phi_b, T)$ is given in that limit by

$$\begin{aligned} p &= -\frac{T^4}{2\pi^2}\left[\sum_B n_B \frac{-\pi^4}{45} + \sum_F n_F \frac{7\pi^4}{360}\right] \\ &= \frac{\pi^2 T^4}{90}\left[\sum_B n_B - \sum_F \frac{7}{8}n_F\right], \end{aligned} \tag{6.10}$$

where remember that n_F is negative. Therefore, given Eq. (6.6), one obtains

$$a = \frac{\pi^2}{30}\left[\sum_B n_B + \sum_F \frac{7}{8}|n_F|\right], \tag{6.11}$$

thus implying $a_{\rm sym} > a_{\rm brok}$ as in the broken phase one loses some relativistic degrees of freedom since particles obtain a mass m due to the Higgs mechanism, with $m > T$ for some of them. Note that one has $a = \frac{\pi^2}{30} g_*$, since one is at equilibrium ($T_i = T$), with g_* defined in Eq. (3.13). Therefore, Eq. (3.12) yields $\rho_{\rm rad} = aT^4$.

The cosmic plasma is characterised by its energy-momentum tensor $T_{\mu\nu}^{\rm plasma}$. For a perfect fluid, it is given by [24]

$$T_{\mu\nu}^{\rm plasma} = w u_\mu u_\nu - p g_{\mu\nu} \quad \text{with} \quad u_\mu = \gamma(1, \vec{v}) \quad \text{and} \quad \gamma \equiv \frac{1}{\sqrt{1-|\vec{v}|^2}}, \tag{6.12}$$

the four-velocity and the Lorentz factor, respectively, and where the trace of $T_{\mu\nu}^{\rm plasma}$ is

$$4\theta \equiv T_{\mu\nu}^{\rm plasma} g^{\mu\nu} = w - 4p = \rho - 3p = 4V_{\rm eff}(\phi_b, T) - T\frac{\partial V_{\rm eff}(\phi_b, T)}{\partial T}, \tag{6.13}$$

with θ the trace anomaly and where $p = -V_{\rm eff}(\phi_b, T)$ and Eq. (6.4) have been used in the last equality.

A general definition for the phase-transition strength α is given in terms of the trace-anomaly difference in both phases $\Delta\theta$, normalised to the enthalpy w to make it dimensionless [106]:

$$\begin{aligned}
\alpha(T_{\rm sym}) &\equiv \frac{4}{3}\frac{\Delta\theta(T_{\rm sym})}{w_{\rm sym}(T_{\rm sym})} \\
&\equiv \frac{\theta_{\rm sym}(T_{\rm sym}) - \theta_{\rm brok}(T_{\rm sym})}{\rho_{\rm rad}(T_{\rm sym})} \\
&= \frac{1}{\rho_{\rm rad}(T_{\rm sym})}\left[V_{\rm eff}(\phi_F, T_{\rm sym}) - \frac{T_{\rm sym}}{4}\left.\frac{\partial V_{\rm eff}}{\partial T}\right|_{\rm sym}\right. \\
&\qquad\qquad \left. - V_{\rm eff}(\phi_T, T_{\rm sym}) + \frac{T_{\rm sym}}{4}\left.\frac{\partial V_{\rm eff}}{\partial T}\right|_{\rm brok}\right] \\
&\equiv \frac{1}{\rho_{\rm rad}(T_{\rm sym})}\left[\Delta V_{\rm eff} - \frac{T}{4}\Delta\frac{\partial V_{\rm eff}}{\partial T}\right]_{T_{\rm sym}},
\end{aligned} \tag{6.14}$$

where the second line arises from the fact that $w = \rho + p = 4/3\rho_{\rm rad}$ for relativistic perfect fluid. Since Eqs. (6.5) and (6.7) lead to $\theta_{\rm sym} = \epsilon$ and $\theta_{\rm brok} = 0$, one then recovers the usual definition of α within the bag model [103, 107]:

$$\alpha_{\rm bag} = \frac{4}{3}\frac{\epsilon}{w_{\rm sym}(T_{\rm sym})} = \frac{\epsilon}{a_{\rm sym}T_{\rm sym}^4}, \tag{6.15}$$

where Eq. (6.8) has been used.

The dynamics of an expanding bubble is governed by the competition between the outward pressure $\Delta p = -\Delta V_{\rm eff} = V_{\rm eff}(\phi_T) - V_{\rm eff}(\phi_F) > 0$ and the friction from the interaction between the bubble wall and the plasma. By solving the hydrodynamic equations one can obtain different velocity profiles for the plasma depending on the bubble combustion mode [103]. In the case of deflagration, the bubble-wall velocity v_w (in the plasma rest frame, far way from the bubble) is subsonic ($v_w < c_s$) and is characterised by the plasma being at rest inside the bubble and a shock front ahead the bubble wall, while in detonation mode, the velocity is supersonic ($v_w > c_s$)

and is characterised by the plasma being at rest outside the bubble and rarefaction waves behind the bubble wall. A hybrid (or supersonic deflagration) mode, which is an intermediate solution, is also possible. In the following, we focus on detonation, for which one can take $T_{\rm sym} = T_n$ [103]. The computation of v_w is a complicated model-dependent task which is beyond the scope of the present manuscript. Here, we consider for, simplicity, a fixed optimistic value $v_w \to 1$.

The kinetic energy fraction of one bubble[1] corresponds to the fraction of the energy contained in the bubble that is converted into the kinetic energy of the plasma and is basically defined as the ratio between the kinetic energy of the plasma and the bag constant ϵ [109, 110]:

$$K = \frac{3}{\rho v_w^3}\int_0^{\xi_{\max}} d\xi\ \xi^2 \tau_{ii}^{\rm plasma} = \frac{3}{\rho v_w^3}\int_0^{\xi_{\max}} d\xi\ \xi^2 [w\gamma^2 v(\xi)^2] \tag{6.16}$$

$$\text{with}\ \ \tau_{ij}^{\rm plasma} = w u_i u_j, \tag{6.17}$$

while the efficiency factor for the conversion of the PT energy budget into the bulk kinetic energy of the plasma is given in the bag model by [103]

$$\kappa_v = \frac{3}{\epsilon v_w^3}\int_0^{\xi_{\max}} d\xi\ \xi^2 [w\gamma^2 v(\xi)^2], \tag{6.18}$$

where $w(\xi)$ and $v(\xi)$ are, respectively, the enthalpy and the velocity of the fluid. They both depend on the self-similar variable $\xi \equiv r/t$, where r is the distance from the center of the bubble and t the time since nucleation. The quantities K and κ_v are then related to each other via

$$\begin{aligned} K &= \kappa_v \frac{\epsilon}{\rho} \\ &= \kappa_v \frac{\epsilon}{a_{\rm sym} T_{\rm sym}^4 + \epsilon} \\ &= \frac{\kappa_v \alpha_{\rm bag}}{1+\alpha_{\rm bag}}. \end{aligned} \tag{6.19}$$

Therefore, the usual relation $K = \kappa_v \alpha/(1+\alpha)$ assumes the bag model to be valid. A fit of the function $\kappa_v(v_w, \alpha)$ is given in both small and large bubble-wall-velocity limit by [103]

$$\kappa_v \simeq \begin{cases} v_w^{6/5} \frac{6.9\alpha_{\rm bag}}{1.36 - 0.037\sqrt{\alpha_{\rm bag}} + \alpha_{\rm bag}} & v_w \ll c_s \\ \frac{\alpha_{\rm bag}}{0.73 + 0.083\sqrt{\alpha_{\rm bag}} + \alpha_{\rm bag}} & v_w \to 1 \end{cases}. \tag{6.20}$$

In practice, one uses α from Eq. (6.14) and the fit for κ in Eq. (6.20) to compute the GW power spectrum [108].

Considering that most of the time dependence of the false-vacuum decay rate per volume $\Gamma(t)/V = A(t)e^{-S_E(t)}$ is in the Euclidean action $S_E(t)$ [111], then its Taylor expansion around the time t_* at which the phase transition completes is given by

$$\frac{\Gamma(t)}{V} \simeq A(t_*)e^{-S_E(t_*)+(t-t_*)\beta} \tag{6.21}$$

---

[1] One assumes that the kinetic energy fraction for a single bubble is representative of the average over the entire plasma [108].

with [112]

$$\beta \equiv - \left.\frac{dS_E}{dt}\right|_{t_*} \simeq \left.\frac{d\ln(\Gamma(t)/V)}{dt}\right|_{t_*}, \tag{6.22}$$

where β^{-1} sets the timescale for the duration of the phase transition. This parameter should not be confused with $\beta \equiv 1/T$ used in Chapter 4. Assuming an isentropic expansion of the Universe ($sa^3 \sim g_{*s}T^3a^3$= constant), one obtains $dT/dt = -HT$, where $dg_{*s}/dt = 0$ has been considered as it does not vary significantly during the phase transition. Then, considering that the phase transition completes at T_*, the β parameter, with $S_E = S_3/T$, takes the form

$$\frac{\beta}{H_*} = T_* \left.\frac{d(S_3/T)}{dT}\right|_{T_*}, \tag{6.23}$$

where one normalised it to the Hubble parameter evaluated at T_*, $H_* \equiv H(T_*)$, to make it dimensionless.

The strength of the phase transition α and the normalised inverse time duration of the phase transition β/H_* are correlated in such a way that a strong PT (large α) is associated to a slow PT (small β/H_*) and vice versa. This can be seen from the fact that $\alpha \sim \Delta V_{\text{eff}}$ (see Eq. (6.14)), while $S_3/T \sim \beta/H_*$ via Eq. (6.23), with $S_3/T \sim 1/\sqrt{\Delta V_{\text{eff}}}$ [111]. This last relation can be found from the definition of S_3 in Eq. (5.20): $S_3 \sim R^3\Delta V_{\text{eff}}$, with R the initial bubble radius (at nucleation time). Comparing both terms in Eq. (5.20), one also obtains $(\phi/R)^2 \sim \Delta V_{\text{eff}}$, or equivalently $R \sim 1/\sqrt{\Delta V_{\text{eff}}}$, thereby implying $S_3 \sim R^3\Delta V_{\text{eff}} \sim 1/\sqrt{\Delta V_{\text{eff}}}$.

6.2 Gravitational-wave power spectrum

Let us briefly derive the expression for the GW energy density and define the GW power spectrum in terms of it. The following is based on [113]. In the weak-gravitational-field approximation, one can linearise gravity and write the metric as $g_{\mu\nu}(x) = \eta_{\mu\nu} + h_{\mu\nu}(x) + \mathcal{O}(h_{\mu\nu})^2$, where $\eta_{\mu\nu}$ is the Minkowski metric, while $h_{\mu\nu}$ is a metric perturbation with $|h_{\mu\nu}| \ll 1$. It can be shown that the quantity $\tilde{h}_{\mu\nu} \equiv h_{\mu\nu} - \frac{1}{2}\eta_{\mu\nu}h$, with $h \equiv \eta^{\mu\nu}h_{\mu\nu}$, satisfies the following wave equation in the Lorenz gauge ($\partial^\nu \tilde{h}_{\mu\nu} = 0$):

$$\Box\tilde{h}_{\mu\nu} = -16\pi G_N T_{\mu\nu}. \tag{6.24}$$

Note that $\tilde{h}_{\mu\nu}$ is a 4×4 real symmetric tensor, with thus 10 degrees of freedom and that the Lorenz gauge removes four of them. This gauge does not saturate the gauge freedom. One then considers the transverse-traceless (TT) gauge (in which $\tilde{h}_{\mu\nu} = h_{\mu\nu}$):

$$h_{\mu 0} = 0, \quad h^j{}_j = 0, \quad \partial_j h_{ij} = 0, \tag{6.25}$$

which further removes four degrees of freedom. Therefore in the end, one is left with $10 - 4 - 4 = 2$ degrees of freedom, the so-called $+$ and $\times$ modes, with amplitude h_+ and $h_\times$, respectively. When in the Lorenz gauge, the GWs in the TT gauge are obtained from the spatial part of the plane wave $h_{\mu\nu}$ by applying the TT-gauge projector $\Lambda_{ij,kl}$: $h_{ij}^{\text{TT}} = \Lambda_{ij,kl}h^{kl}$.

In the quadrupole approximation (one only keeps the leading term in the multipole expansion), the gravitational-wave mode h_{ij}^{TT} can be expressed as

$$h_{ij}^{\mathrm{TT}} \simeq \frac{4G_N}{r}\int d^3x T_{ij}^{\mathrm{TT}}(x, t-r) \tag{6.26}$$

$$= \frac{2G_N}{r}\ddot{Q}_{ij}(t-r), \tag{6.27}$$

with the retarded time $t-r$, $r = |\vec{x}|$, where T_{ij} is the shear-stress part of the matter energy-momentum tensor and where Q_{ij} is the quadrupole moment, which basically characterises any departure from spherical symmetry.

To study how GWs curve the background spacetime, one promotes the background metric $\eta_{\mu\nu}$ to a dynamical one: $\eta_{\mu\nu} \to \eta_{\mu\nu}(x)$. Then it is possible to rewrite the Einstein equations in such a way that $T^{\mu\nu}_{\mathrm{gw}}$, the energy-momentum tensor associated to the gravitational waves, is appearing on the right-hand side. It is expressed as

$$T^{\mu\nu}_{\mathrm{gw}} = \frac{1}{32\pi G_N}\langle \partial^\mu h^{\alpha\beta}\partial^\nu h_{\alpha\beta}\rangle, \tag{6.28}$$

where $\langle\ \rangle$ is the spatial average over several wavelengths [114]. One then obtains the GW energy density via

$$\rho_{\mathrm{gw}} = T^{00}_{\mathrm{gw}} = \frac{1}{32\pi G_N}\langle \dot{h}^{\alpha\beta}\dot{h}_{\alpha\beta}\rangle. \tag{6.29}$$

Since the energy momentum tensor of the gravitational field $T^{\mu\nu}_{\mathrm{gw}}$ only depends on the physical modes h_{ij}^{TT}, one can rewrite the above equation as

$$\rho_{\mathrm{gw}} = \frac{1}{32\pi G_N}\langle \dot{h}_{ij}^{\mathrm{TT}}\dot{h}_{ij}^{\mathrm{TT}}\rangle \tag{6.30}$$

$$= \frac{1}{16\pi G_N}\langle \dot{h}_+^2 + \dot{h}_\times^2\rangle. \tag{6.31}$$

One can finally write

$$\rho_{\mathrm{gw}} = \int d\ln f \frac{d\rho_{\mathrm{gw}}}{d\ln f} = \rho_{\mathrm{tot}}\int d\ln f\ \Omega_{\mathrm{GW}}(f), \tag{6.32}$$

where the GW power spectrum is defined as [107]

$$\Omega_{\mathrm{GW}}(f) \equiv \frac{1}{\rho_{\mathrm{tot}}}\frac{d\rho_{\mathrm{gw}}}{d\ln f}. \tag{6.33}$$

After the gravitational waves have been generated in the early Universe, they are only affected by the expansion of the Universe. To compute the GW spectrum today, one then needs to take this redshift into account. The isentropy of the Universe implies $sa^3 \sim g_{*s}T^3a^3 =$ constant and thus

$$\frac{a_*}{a_0} = \frac{T_0}{T_*}\left(\frac{g_{*s,0}}{g_*}\right)^{1/3}, \tag{6.34}$$

where the subscript $*$ means that the paramters are evaluated at the time of GW production and where one used the fact that $g_* = g_{*s}$ at the EW scale. The Hubble parameter at the time of GW generation H_*, redshifted to today, is given by

$$\begin{aligned} h_* = \frac{a_*}{a_0} H_* &= T_0 (g_{*s,0})^{1/3} \left(\frac{8\pi^3}{90 M_p^2} \right)^{1/2} g_*^{1/6} T_* \\ &\simeq 5.05 \times 10^{-32} g_*^{1/6} T_* \\ &\simeq 1.65 \times 10^{-5} \text{ Hz} \left(\frac{g_*}{100} \right)^{1/6} \frac{T_*}{100 \text{ GeV}}, \end{aligned} \tag{6.35}$$

where one used

$$H_*^2 = \frac{8\pi\rho}{3M_p^2} \simeq \frac{8\pi\rho_{\text{rad}}}{3M_p^2}, \tag{6.36}$$

$$T_0 \simeq 2.73\text{K} \xrightarrow{\times k_B = 1} 2.35 \times 10^{-13} \text{ GeV}, \tag{6.37}$$

$$1\text{GeV} \xrightarrow{\times 1/\hbar = 1} 1.52 \times 10^{24} \text{ Hz} \tag{6.38}$$

and where $g_{*s,0} \simeq 3.94$ is computed in Eq. (3.21), while ρ_{rad} is given in Eq. (3.12).

The peak frequency today f_0 is obtained by the redshift of the peak frequency at the time of GW generation f_*:

$$\begin{aligned} f_0 = \frac{a_*}{a_0} f_* &= \frac{a_*}{a_0} H_* \frac{f_*}{\beta} \frac{\beta}{H_*} \\ &\simeq 1.65 \times 10^{-5} \text{ Hz} \left(\frac{f_*}{\beta} \right) \left(\frac{\beta}{H_*} \right) \left(\frac{T_*}{100 \text{ GeV}} \right) \left(\frac{g_*}{100} \right)^{1/6}, \end{aligned} \tag{6.39}$$

while the redshift of the GW power spectrum is given by

$$\begin{aligned} &\rho_{\text{gw},0} = \rho_{\text{gw},*} \left(\frac{a_*}{a_0} \right)^4 \\ \Longleftrightarrow \Omega_{\text{GW},0} \equiv \frac{1}{\rho_c} \frac{d\rho_{\text{gw},0}}{d\ln f} &= \frac{\rho_*}{\rho_c} \frac{1}{\rho_*} \frac{d\rho_{\text{gw},*}}{d\ln f} \left(\frac{a_*}{a_0} \right)^4 \equiv \frac{\rho_*}{\rho_c} \Omega_{\text{GW},*} \left(\frac{a_*}{a_0} \right)^4. \end{aligned} \tag{6.40}$$

For $\rho_* \simeq \rho_{\text{rad}}$, one can thus express the present GW power spectrum as

$$h^2 \Omega_{\text{GW},0} \simeq 1.67 \times 10^{-5} \left(\frac{100}{g_*} \right)^{1/3} \Omega_{\text{GW},*}, \tag{6.41}$$

where one used

$$\begin{aligned} \left(\frac{a_*}{a_0} \right)^4 \frac{\rho_{\text{rad}}}{\rho_c} &= T_0^4 (g_{*s,0})^{4/3} \frac{\pi^2}{30 \times 100^{1/3}} \left(\frac{100}{g_*} \right)^{1/3} \frac{1}{\rho_c} \\ &\simeq 1.67 \times 10^{-5} h^{-2} \left(\frac{100}{g_*} \right)^{1/3} \end{aligned} \tag{6.42}$$

$$\begin{aligned} \text{with } \rho_c \equiv \frac{3M_p^2}{8\pi} H_0^2 &\equiv \frac{3M_p^2}{8\pi} \left[100 \; h \text{ km s}^{-1} \text{ Mpc}^{-1} \right]^2 \\ &\xrightarrow{\times \hbar^2 = 1} 8.10 \times 10^{-47} h^2 \text{ GeV}^4. \end{aligned} \tag{6.43}$$

Although its wall is accelerating, one single bubble of true vacuum, due to its spherical symmetry, cannot be responsible of the generation of gravitational waves, because its quadrupole (and higher-order multipole) moments vanish: $h_{ij}^{\mathrm{TT}} = 0$ via Eq. (6.27). The key ingredient for a stochastic GW background to be generated from a cosmic phase transition is the collisions between these bubbles. Indeed this will break the spherical symmetry of each of the collided scalar-field bubbles [107]. For bubbles evolving in a thermal plasma, additional sources of GW production come from the metric perturbation induced by the plasma: sound waves [8, 115] and magnetohydrodynamic (MHD) turbulences [116]. These three[2] contributions to the GW power spectrum will be reviewed below.

One usually has three scenarios for the expansion of a true-vacuum bubble [96]. If it expands within a plasma and that the friction from the bubble-plasma interaction can counterbalance the pressure leading to that expansion, then the bubble wall will reach a terminal velocity and does not accelerate indefinitely. If, however, the pressure is too large and/or the friction is not sufficient to compensate each other, this results in a runaway bubble wall, which eventually expands at the speed of light. Lastly the runaway scenario can also happen in vacuum, usually in case of strong supercooling.

The efficiency factor κ_ϕ for the conversion of the released PT energy budget into the kinetic and gradient energy of the bubble wall (outside the wall the derivative of the bounce vanishes), is responsible for the acceleration of the bubble. Another part κ_v of this energy budget is transmitted to the bulk motion of the plasma. The last part κ_{therm} is converted to thermal energy reheating the plasma; it is thus not a part generating the source of GW production [118]. As long as the condition

$$\Delta V_{\text{eff}} > \Delta P_{\text{LO}} + \gamma_w \Delta P_{\text{NLO}} \tag{6.44}$$

is satisfied,[3] the bubble wall keeps accelerating. This happens because the energy deposited in the plasma saturates and no longer changes the fluid profile. The excess energy is then transmitted to the bubble wall, thus accelerating the latter. The leading-order contribution to the friction, ΔP_{LO}, arises from $1 \to 1$ processes at the bubble wall and is given by [119]

$$\Delta P_{\text{LO}} \simeq \frac{T_*^2}{24} \left[\sum_B n_B \Delta m_B^2(\phi_b) - \frac{1}{2} \sum_F |n_F| \Delta m_F^2(\phi_b) \right] \tag{6.45}$$

with $\Delta m^2(\phi_b) \equiv m^2(\phi_T) - m^2(\phi_F)$ and where a fast enough wall is assumed.[4,5] As for the next-to-leading order contribution to the friction, $\gamma_w \Delta P_{\text{NLO}}$, it arises from $1 \to 2$ splitting processes (transition radiation)

---

[2] A new contribution, from feebly interacting particles, has been recently studied in [117]. This contribution is more appropriate for phase transitions in the dark sector and therefore does not pertain to our analysis.

[3] If one only considers the leading-order friction, this condition becomes $\Delta V_{\text{eff}} > \Delta P_{\text{LO}}$, as it was originally done in [119]. This leading-order condition has been recently improved in [120].

[4] The wall is sufficiently fast so that all particles from the symmetric phase enter the bubble, thereby no particles are reflected at the bubble wall and no particles from the broken phase escape the bubble.

[5] Note that another expression for the NLO term is derived in [121], and results in a dependence in $\gamma_w^2 T^4$, instead of $\gamma_w m_V T^3$. It consists of $1 \to N$ splitting processes at the bubble wall, including the $1 \to 2$ processes from [122]. However, as mentioned in [123], this alternative expression for the NLO friction seems inconsistent.

and is given by [122]

$$\gamma_w \Delta P_{\text{NLO}} \simeq \gamma_w T_*^3 \sum_{i \in V} g_i^2 n_i \Delta m_i(\phi_b), \tag{6.46}$$

where the dominant contribution comes from the emission of vector bosons V gaining mass during the PT and where γ_w and g_i are the Lorentz factor of the bubble wall and the gauge couplings associated to the gauge bosons V, respectively.

If the released PT energy is not sufficient to overcome the leading-order friction, the bubble wall reaches a terminal velocity and the released PT energy is essentially transmitted to the bulk motion of the plasma, thus leading to

$$\kappa_v + \kappa_{\text{therm}} = 1. \tag{6.47}$$

On the other hand, in the case $\Delta V_{\text{eff}} > \Delta P_{\text{LO}}$, the bubble will be in the runaway regime, unless $\gamma_w \Delta P_{\text{NLO}}$ (increasing with the bubble-wall velocity) is significant enough for the bubble wall to reach a terminal velocity. In this situation, one thus has

$$\kappa_\phi + \kappa_v + \kappa_{\text{therm}} = 1 \tag{6.48}$$

$$\text{with} \quad \kappa_v = \frac{\alpha_{\text{eff}}}{\alpha}\kappa_{\text{eff}}, \quad \kappa_{\text{therm}} = (1-\kappa_{\text{eff}})\frac{\alpha_{\text{eff}}}{\alpha}, \quad \alpha_{\text{eff}} = \alpha(1-\kappa_\phi). \tag{6.49}$$

where κ_{eff} is an effective κ_v: $\kappa_{\text{eff}} = \kappa_v(\alpha \to \alpha_{\text{eff}})$, with κ_v given in Eq. (6.20). As for κ_ϕ, defining R_{eq} as the radius at which the bubble wall stops accelerating and reaches a terminal velocity, it is expressed as [124]

$$\kappa_\phi = \begin{cases} 1 - \frac{\alpha_\infty}{\alpha} & \text{for} \quad R_* \leq R_{\text{eq}} \\ \frac{\gamma_{w,\text{eq}}}{\gamma_{w,*}}\left[1 - \frac{\alpha_\infty}{\alpha}\left(\frac{\gamma_{w,\text{eq}}}{\gamma_{w,*}}\right)^2\right] & \text{for} \quad R_* > R_{\text{eq}} \end{cases} \tag{6.50}$$

with R_* the average bubble radius at percolation time, $\gamma_{w,i} \equiv \gamma_w(R_i)$ and [96, 103]

$$\alpha_\infty = \frac{\Delta P_{\text{LO}}}{\rho_{\text{rad}}} \simeq \frac{T_*^2}{24\rho_{\text{rad}}}\left[\sum_B n_B \Delta m_B^2(\phi_b) - \frac{1}{2}\sum_F |n_F| \Delta m_F^2(\phi_b)\right]. \tag{6.51}$$

As mentioned earlier, one contribution to the GW power spectrum Ω_{GW} comes from the (bounce) scalar field or bubble collisions. This is usually computed using the so-called *envelope approximation* [107, 125–127] in which the energy is stored in a thin shell near the bubble wall and when a collision between bubbles occurs, the released energy quickly disperses, thus making the energy essentially stored in the uncollided part of the bubbles; one basically considers that only the energy-momentum tensor T_{ij}^{TT} of the envelope generates GWs. In this approximation, the collided part of the wall is neglected; only the shape or *envelope* of the resulting system of bubbles matters for the computation of GW generation [127]. This is depicted in Fig. 6.1. Other models aim to describe the GW power spectrum from the scalar field, such as the *bulk flow model*, which considers that the collided part continue to propagate [128, 129] or simulations from

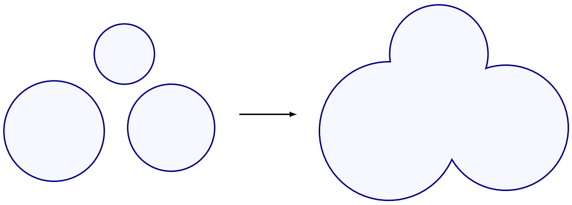

Figure 6.1: Envelope approximation. The collided parts of the bubble walls disappear, only leaving the envelope made by the uncollided parts.

lattice [130], which, in addition, take into account the oscillation of the scalar field around the true vacuum[6] [131].

The present bubble-collision contribution to the GW signal is obtained by the fit from numerical simulation of colliding bubbles in the envelope approximation and is given by [132]

$$h^2\Omega_{\mathrm{col},0}(f) = h^2\Omega^{\mathrm{peak}}_{\mathrm{col},0} S_{\mathrm{col}}(f) \tag{6.52}$$

with

$$h^2\Omega^{\mathrm{peak}}_{\mathrm{col},0} = 1.67\times 10^{-5}\left(\frac{100}{g_*}\right)^{1/3}\left(\frac{H_*}{\beta}\right)^2\left(\frac{\kappa_\phi\alpha}{1+\alpha}\right)^2\left(\frac{0.11v_w^3}{0.42+v_w^2}\right), \tag{6.53}$$

where one recognises the redshifting factor from Eq. (6.41) and where the spectral shape is given by

$$S_{\mathrm{col}}(f) = \frac{3.8\,(f/f_{\mathrm{col},0})^{2.8}}{1+2.8\,(f/f_{\mathrm{col},0})^{3.8}} \tag{6.54}$$

$$\text{with}\quad f_{\mathrm{col},0} = \frac{h_*}{H_*} f_{\mathrm{col},*} \simeq 1.65\times 10^{-5}\ \mathrm{Hz}\left(\frac{f_{\mathrm{col},*}}{\beta}\right)\left(\frac{\beta}{H_*}\right)\left(\frac{T_*}{100\ \mathrm{GeV}}\right)\left(\frac{g_*}{100}\right)^{1/6} \tag{6.55}$$

$$\text{and}\quad \frac{f_{\mathrm{col},*}}{\beta} = \frac{0.62}{1.8-0.1v_w+v_w^2}, \tag{6.56}$$

where $f_{\mathrm{col},*}$ is the peak frequency at the time of GW emission, thus the frequency at $h^2\Omega^{\mathrm{peak}}_{\mathrm{col},*}$ and where the present peak frequency $f_{\mathrm{col},0}$ is obtained via redshifting as in Eq. (6.39). Note that the damping of the GW signal for a large value of β/H_* (fast PT) arises from the fact that the bubble radius at percolation time is $R_* \sim \beta^{-1}$, as can be seen below in Eq. (6.60). Indeed, for constant H_*, high β/H_* means that bubbles collide with each other when being relatively small, thus creating *weaker* anisotropic stress than it would for the case of larger bubbles [133]. This results in a weaker GW peak signal. Moreover, these weak anisotropies are associated with small wavelengths and thus high frequencies; this explains why the peak frequency is larger for larger values of β/H_*. Equivalently, since a large β/H_* corresponds to a fast PT, this means that the bubble nucleation rate is large, thereby collisions of bubbles occur *more frequently* than in the

---

[6] This is a subdominant contribution to the GW power spectrum as long as the scalar field mass is inferior to the Planck mass [130].

case of a slow PT and thus shift the GW power spectrum towards higher frequencies [134].

As mentioned in the previous section, interactions between the expanding bubble and the surrounding plasma lead to compression waves ahead the bubble wall or rarefaction waves behind the bubble wall in the case of subsonic bubbles or supersonic bubbles, respectively. When the sound waves from different bubbles overlap, the induced shear stress generates gravitational waves. As these acoustic waves pass through one another, they continue to oscillate, thereby acting as a GW source for a Hubble time[7] [109], long after the completion of the phase transition for $\beta^{-1} \ll H^{-1}$, contrary to the GW source from bubble collision, which is a short-lasting process. This is the reason why there is an enhancement factor β/H_* for the sound-wave contribution compared to scalar-field one, as can be seen below.

The sound-wave contribution[8] to the present GW power spectrum is given by

$$h^2\Omega_{\rm sw,0}(f) = h^2\Omega^{\rm peak}_{\rm sw,0} S_{\rm sw}(f), \tag{6.57}$$

with [108, 136, 137]

$$h^2\Omega^{\rm peak}_{\rm sw,0} = h^2\ 3 \times 0.687 F_{\rm gw,0}\Gamma^2 \bar{U}_f^4 \frac{H_* R_*}{c_s}\tilde{\Omega}_{\rm gw}\Upsilon, \tag{6.58}$$

where the mean adiabatic index is $\Gamma \equiv \bar{w}/\bar{\rho} = 4/3$ for a relativistic fluid (since in that case $p = \rho/3$) and where the enthalpy-weighted root-mean-square of the fluid velocity $\bar{U}_f$ is expressed as [137]:

$$\bar{U}_f = \sqrt{\frac{K}{\Gamma}}, \quad K = \frac{\kappa_v \alpha}{1+\alpha}. \tag{6.59}$$

Note that we have corrected the formula in [108] by adding a factor 3 in Eq. (6.58). Note also that although this factor 3 is present in [136, 137], the factor $1/c_s$ considered in [108] is not present in [136, 137]. The mean bubble separation at percolation temperature R_* is defined as[9] [108]

$$R_* = \frac{(8\pi)^{1/3}\max\{c_s, v_w\}}{\beta} \tag{6.60}$$

with $c_s = 1/\sqrt{3}$ the speed of sound in the plasma in the bag model (see Eq. (6.9)). The parameter $\tilde{\Omega}_{\rm gw}$ quantifies the efficiency with which the shear stress from the overlapping of sound waves can generates GWs and is numerically found to be $\tilde{\Omega}_{\rm gw} \simeq 1.2 \times 10^{-2}$ [136, 137]. Finally, the factor $F_{\rm gw,0}$, needed to obtain the present value $h^2\Omega^{\rm peak}_{\rm sw,0}$, is defined as [108, 137]

$$F_{\rm gw,0} = \Omega_{\gamma,0}\left(\frac{g_{s*,0}}{g_{s*}}\right)^{4/3}\frac{g_*}{g_{*,0}}, \tag{6.61}$$

where $\Omega_{\gamma,0} \equiv \rho_{\gamma,0}/\rho_c$ is the present photon density parameter, with $\rho_{\gamma,0} = 0.26$ eV cm^{-3} [28]. The parameters g_{s*} and g_* are equal at the EW scale,

---

[7] Note that this lifetime corresponds to the one of the GW source, not to the lifetime of sound waves [109].

[8] An analytical *sound-shell model* is described in [110, 135].

[9] This definition is not valid for slow PTs, with $\beta/H_* \sim \mathcal{O}(1)$ [108]. Moreover R_* can also be seen as the average bubble radius at percolation [138]. Both definitions yield a length scale of the same order of magnitude.

while g_{s0} and g_0 are different since they are considered after the neutrino decoupling. Note that in [108, 136], they consider $g_{s0} = 3.91$ and only the photon contribution for $g_0(= 2)$, while we use $g_{s0} = 3.94$ obtained in Eq. (3.21) and $g_0 = 2 + N_{\rm eff}\ 7/8 \times 2 \times (4/11)^{4/3} = 3.38$. Using $\rho_c = 1.05 \times 10^{-5} h^2$ GeV cm^{-3} derived in Eq. (3.19), one can then compute $F_{\rm gw,0}$:

$$F_{\rm gw,0} = \frac{9.82 \times 10^{-6}}{h^2} \left(\frac{100}{g_*}\right)^{1/3}. \tag{6.62}$$

Putting it all together, one finally obtains

$$\begin{aligned} h^2\Omega_{\rm sw,0}^{\rm peak} &= h^2\ 3 \times 0.687 \frac{9.82 \times 10^{-6}}{h^2} \left(\frac{100}{g_*}\right)^{1/3} \left(\frac{\kappa_v \alpha}{1+\alpha}\right)^2 \\ &\quad \times \frac{H_*(8\pi)^{1/3} \max\{c_s, v_w\}}{\beta/\sqrt{3}} 1.2 \times 10^{-2}\ \Upsilon \\ &\simeq 1.23 \times 10^{-6} \left(\frac{H_*}{\beta}\right) \left(\frac{\kappa_v \alpha}{1+\alpha}\right)^2 \left(\frac{100}{g_*}\right)^{1/3} \max\{c_s, v_w\}\ \Upsilon, \end{aligned} \tag{6.63}$$

where, as mentioned earlier, $h^2\Omega_{\rm sw,0}^{\rm peak}$ is only proportional to a factor H_*/β, while $h^2\Omega_{\rm col,0}^{\rm peak}$ contains a factor $(H_*/\beta)^2$ because of an enhancement β/H_* in $h^2\Omega_{\rm sw,0}^{\rm peak}$ translating the fact that sound waves source GW production a long time after the end of the phase transition. The quantity Υ corresponds to the suppression factor due to the fact that after a time $\tau_{\rm sw}$, the onset of turbulence prevents sound waves to source the GW production. In a radiation-dominated Universe Υ is given by [124, 139]

$$\Upsilon = 1 - \frac{1}{\sqrt{2\tau_{\rm sw} H_* + 1}} \quad \text{with} \quad \tau_{\rm sw} \equiv \min\left[H_*^{-1}, \frac{R_*}{\bar{U}_f}\right], \tag{6.64}$$

where $\tau_{\rm sw} \leq H_*^{-1}$ is the lifetime of the sound-wave GW source and where one has $\Upsilon \simeq \tau_{\rm sw} H_*$ when $\tau_{\rm sw} H_* \ll 1$. Finally, the spectral shape is given by [136]

$$S_{\rm sw}(f) = \left(\frac{f}{f_{\rm sw,0}}\right)^3 \left(\frac{7}{4 + 3\left(f/f_{\rm sw,0}\right)^2}\right)^{7/2} \tag{6.65}$$

$$\begin{aligned} \text{with} \quad f_{\rm sw,0} &= \frac{h_*}{H_*} f_{\rm sw,*} \\ &\simeq 26 \times 10^{-6} \text{Hz} \left(\frac{1}{H_* R_*}\right) \left(\frac{z_{\rm peak}}{10}\right) \left(\frac{T_*}{100\ \text{GeV}}\right) \left(\frac{g_*}{100}\right)^{1/6} \end{aligned} \tag{6.66}$$

$$\text{and} \quad z_{\rm peak} = (kR_*)_{\rm peak} = 2\pi f_{\rm sw,*} \frac{(8\pi)^{1/3} v_w}{\beta} \Longleftrightarrow f_{\rm sw,*} \simeq 0.54 \frac{\beta}{v_w} \frac{z_{\rm peak}}{10}, \tag{6.67}$$

where $z_{\rm peak}$ is the peak angular frequency in units of the mean bubble separation and is generally close to 10, and $f_{\rm sw,0}$ is the sound-wave peak frequency today.

A perturbation of a fluid with a large Reynolds number leads to turbulence. In our case, the Reynolds number of the fully ionised plasma is around 10^{13} at the EW scale, therefore the stirring of the fluid caused by bubble collisions leads to MHD turbulence [116]. The shear stress induced by the chaotic motion of the fluid and by the magnetic field generate gravitational waves. From simulations it is believed that only a fraction $\kappa_{\text{turb}} = \varepsilon\kappa_v$, with $\varepsilon = 0.05 - 0.1$ [96], of the bulk motion is converted into vorticity. Extra contributions from the fact that, after a time τ_{sw}, shocks begin to form in the fully ionised plasma, thus turning the acoustic-wave contribution into turbulent contribution should in principle increase ε [85].

The MHD-turbulence contribution is given by [96, 116, 118]

$$h^2\Omega_{\text{turb},0}(f) = h^2\Omega^{\text{peak}}_{\text{turb},0} S_{\text{turb}}(f), \tag{6.68}$$

with

$$\begin{aligned} h^2\Omega^{\text{peak}}_{\text{turb},0} = 3.35 \times 10^{-4} \left(\frac{H_*}{\beta}\right) \left(\frac{\kappa_{\text{turb}}\alpha}{1+\alpha}\right)^{3/2} \left(\frac{100}{g_*}\right)^{1/3} v_w \\ \times \left[\frac{1}{2^{11/3}\left(1 + 8\pi f_{\text{turb},0}/h_*\right)}\right] \end{aligned} \tag{6.69}$$

and the spectral shape

$$S_{\text{turb}}(f) = \frac{\left(f/f_{\text{turb},0}\right)^3}{\left[1 + \left(f/f_{\text{turb},0}\right)\right]^{11/3}} \left[\frac{2^{11/3}\left(1 + 8\pi f_{\text{turb},0}/h_*\right)}{1 + 8\pi f/h_*}\right] \tag{6.70}$$

$$\begin{aligned} \text{with} \quad f_{\text{turb},0} &= \frac{h_*}{H_*} f_{\text{turb},*} \\ &\simeq 2.89 \times 10^{-5}\ \text{Hz} \frac{1}{v_w} \left(\frac{\beta}{H_*}\right) \left(\frac{T_*}{100\ \text{GeV}}\right) \left(\frac{g_*}{100}\right)^{1/6} \end{aligned} \tag{6.71}$$

$$\text{and} \quad f_{\text{turb},*} \simeq 3.5 \frac{\beta}{2v_w}, \tag{6.72}$$

where the numerator between the last brackets in the expression of $S_{\text{turb}}(f)$ is added to make $f_{\text{turb},0}$ the present MHD-turbulence peak frequency, that is to have $S_{\text{turb}}(f_{\text{turb},0}) = 1$ (this explains the presence of the inverse of this factor in $h^2\Omega^{\text{peak}}_{\text{turb},0}$ to cancel it). Similarly to the sound-wave contribution $h^2\Omega^{\text{peak}}_{\text{sw},0}$, the MHD-turbulence contribution $h^2\Omega^{\text{peak}}_{\text{turb},0}$ is enhanced by a factor of β/H_*. Moreover, the explicit dependence of $S_{\text{turb}}(f)$ in h_* indicates that turbulence sources the anisotropic stress for several Hubble times [96]. Note that the contribution to the GW signal from MHD turbulence is not well understood and is still an area of active research [96, 108].

Finally, the total contribution to the stochastic gravitational-wave background is thus obtained by summing the contribution from bubble collision, overlapping of sound waves and MHD turbulence. The resulting GW power spectrum from a first-order phase transition in the early Universe is thus, at least approximately, a linear superposition of the three aforementioned contributions:

$$h^2\Omega_{\text{GW},0} \simeq h^2\Omega_{\text{col},0} + h^2\Omega_{\text{sw},0} + h^2\Omega_{\text{turb},0}. \tag{6.73}$$

To conclude, let us see how the GW signal $h^2\Omega_{\text{GW},0}$ behaves when one changes the key parameters $\alpha, \beta/H_*$ and T_n. Increasing α increases the peak of the GW power spectrum $h^2\Omega^{\text{peak}}_{\text{GW},0}$ and thus shifts the GW signal upward in a plot $h^2\Omega_{\rm GW}(f)$ vs. f. Increasing β/H_* both increases the peak frequency $f_{\rm peak,0}$ and decreases $h^2\Omega^{\rm peak}_{\rm GW,0}$, therefore the GW signal is shifted towards the down-right direction. Finally, for a constant β/H_*, the impact of an increasing T_n is simply to increase $f_{\rm peak,0}$ and thus to shift the GW signal rightward. However, if one considers the dependency of H_* in T_n ($H_* \sim T_n^2$), then $h^2\Omega^{\rm peak}_{\rm GW,0}$ increases, while $f_{\rm peak,0}$ decreases with T_n, thus shifting the GW signal towards the up-left direction for rising T_n [133]. These behaviours are depicted in Fig. 6.2.

6.3 Space-based gravitational-wave detectors

The advantage of performing observations in outer space is that it avoids seismic noise which limits stochastic GW background searches below ~ 1 Hz [140]. Space-based laser interferometers such as the Laser Interferometer Space Antenna (LISA) [10], the Decihertz Interferometer Gravitational-Wave Observatory (DECIGO) [141], the Big Bang Observer (BBO) [142], Taiji [143] and TianQin [144] are relevant for the detection of a stochastic GW background from an EW FOPT.[10] Indeed, as it has been explicitly shown in the previous section, the present GW signal from a FOPT peaks at a frequency $f_{\rm peak} \sim 10^{-5}\beta/H_*(T_n/100~{\rm GeV})$ Hz. For a typical fast FOPT at the EW scale ($T_n \sim 100$ GeV), one obtains $\beta/H_* \sim 100$, thus resulting in a peak frequency in the millihertz. This justifies the use of GW detectors such as LISA, whose probed frequency range is around the millihertz. In this section, we focus on LISA, DECIGO and BBO.

Using a single detector to probe a stochastic GW background is not efficient as the GW signal is weaker than the detector noise. To overcome this issue, one usually cross-correlate the output of two or more detectors with independent noises, as for instance shown in [154]. Actually, techniques have been developed to be able to detect such a signal with one detector via auto-correlation of outputs [155–158]. LISA consists of three spacecrafts forming altogether an equilateral triangle and will perform auto-correlation measurements, while DECIGO and BBO consist of two sets of triangle configuration put together like the star of David and will perform cross-correlation measurements [118]. The stochastic GW background can be detected by LISA, DECIGO or BBO working for a period $t_{\rm obs}$ if the signal-to-noise ratio (SNR) ρ is above some threshold value $\rho_{\rm thrs}$ [68, 159]:

$$\rho^2 = n_{\rm det}\frac{t_{\rm obs}}{\rm s}\int_{f_{\rm min}}^{f_{\rm max}}\frac{df}{\rm Hz}\left(\frac{h^2\Omega_{\rm GW,0}(f)}{h^2\Omega_{\rm n,eff}(f)}\right)^2 \geq \rho^2_{\rm thrs}, \tag{6.74}$$

where the range $[f_{\rm min},\ f_{\rm max}]$ corresponds to the bandwidth of the detectors, $h^2\Omega_{\rm n,eff}(f)$ is the effective noise energy density and where $n_{\rm det}$ is the number of detectors. In the case of LISA $n_{\rm det} = 1$ (auto-correlation), while $n_{\rm det} = 2$ (cross-correlation from two networks of detectors) for BBO or DECIGO.

Assuming that the stochastic GW background signal follows a single power law with spectral index b in the frequency range $[f_{\rm min},\ f_{\rm max}]$ probed

---

[10] Note that inflation [145, 146], cosmic strings [147–149] or primordial black holes [150, 151] can also be responsible for a cosmological stochastic GW background. A stochastic GW background from astrophysical origin can be generated by compact binary systems such as binary black hole [152] for instance. Other sources can be found in this review [153].

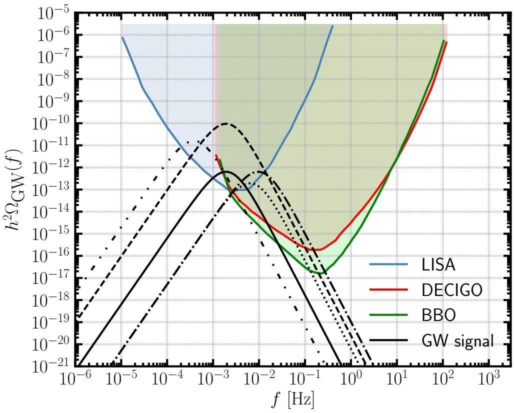

Figure 6.2: PLI sensitivity curves $h^2\Omega_{\rm PLI}(f)$ for LISA, BBO and DECIGO, with $t_{\rm obs} = 4$ yr and $\rho_{\rm thrs} = 10$. The black curve corresponds to a typical GW power spectrum from an EW FOPT. The black dashed curved is obtained by increasing the PT strength α. The black dotted curve is obtained by increasing β/H_*, the inverse time PT duration normalised to the Hubble parameter. The black dashed-dotted curve is obtained by increasing the nucleation temperature T_n, while keeping β/H_* constant. If, however, one considers the dependence $H_* \sim T_n^2$, then increasing T_n leads to the black dashed-double-dotted curve.

by the GW detectors, one can then express $h^2\Omega_{\rm GW}$ as [159]

$$h^2\Omega_{\rm GW,0} = h^2\Omega_b(f_{\rm ref})\left(\frac{f}{f_{\rm ref}}\right)^b, \tag{6.75}$$

where $f_{\rm ref}$ is some arbitrarily chosen reference frequency, whose specific value is not important as will be seen below. Then Eq. (6.74) can be rewritten as

$$h^2\Omega_b(f_{\rm ref}) \geq h^2\Omega_b^{\rm thrs}(f_{\rm ref}) \equiv \frac{\rho_{\rm thrs}}{\sqrt{n_{\rm det}\frac{t_{\rm obs}}{\rm s}}}\left[\int_{f_{\rm min}}^{f_{\rm max}}\frac{df}{\rm Hz}\left(\frac{(f/f_{\rm ref})^b}{h^2\Omega_{\rm n,eff}(f)}\right)^2\right]^{-1/2}. \tag{6.76}$$

One then defines the power-law integrated (PLI) sensitivity curves as [68, 159]

$$h^2\Omega_{\rm PLI}(f) \equiv \max_b\left[h^2\Omega_b^{\rm thrs}(f_{\rm ref})\left(\frac{f}{f_{\rm ref}}\right)^b\right], \tag{6.77}$$

where one can see that, given the expression of $\Omega_b^{\rm thrs}$ in Eq. (6.76), $\Omega_{\rm PLI}(f)$ is independent of $f_{\rm ref}$. The PLI sensitivity curves for LISA, BBO and DECIGO, with $\rho_{\rm thrs} = 10$ and $t_{\rm obs} = 4$ yr, are depicted in Fig. 6.2 [160]. Note that in reality the GW signal follows a broken power law. Therefore, the PLI sensitivity curves should be considered more as a qualitative visualisation tool rather than a rigorous way to claim that one obtains $\rho > \rho_{\rm thrs}$ for the GW signal [118].

In a more recent approach [118,161], the SNR in Eq. (6.74) is rewritten as

$$\frac{\rho^2}{t_{\mathrm{obs/yr}}} = \sum_{i,j} c_{ij} \left(\frac{h^2\Omega^{\mathrm{peak}}_{i/j}}{h^2\Omega^{i/j}_{\mathrm{PIS}}} \right)^2 \tag{6.78}$$

$$\text{with} \quad h^2\Omega^{\mathrm{peak}}_{i/j} \equiv \left(h^2\Omega^{\mathrm{peak}}_{i,0} h^2\Omega^{\mathrm{peak}}_{j,0} \right)^{1/2} \tag{6.79}$$

$$\text{and} \quad h^2\Omega^{i/j}_{\mathrm{PIS}} \equiv \left[(2-\delta_{ij}) n_{\mathrm{det}} 1\ \mathrm{yr} \int_{f_{\mathrm{min}}}^{f_{\mathrm{max}}} df \frac{S_i(f)S_j(f)}{(h^2\Omega_{\mathrm{n,eff}}(f))^2} \right]^{-1/2} \tag{6.80}$$

with $i, j \in \{\mathrm{col, sw, turb}\}$, $c_{ij} = 1\ (1/2)$ for $i = j$ $(i \neq j)$ and where PIS stands for peak-integrated sensitivity. In this approach, instead of assuming the GW signal to follow a single power law ($S_i = (f/f_{\mathrm{ref}})^p$), one considers the spectral shape given in Eqs. (6.54), (6.65), (6.70). Obviously, the PIS curves should be updated for any new results about the spectral shapes S_i. For more details about PIS curves, see [118, 161].

Chapter 7

Summary

The discovery of gravitational waves in 2015 spectacularly confirmed the robustness of General Relativity. It opened a new channel to investigate dark matter, an unknown matter made of exotic particles, which constitutes 85% of the matter content in the Universe. Possible first-order cosmic phase transitions happening in the early Universe may have left a gravitational-wave imprint that could be detected today. Our current theory, the Standard Model of particle physics, does not predict such a phase transition, but a smooth crossover that does not generate such signals. For models of dark matter which have a first-order phase transition instead, searching for the gravitational-wave signal is a new way to probe dark matter. In this thesis we studied different dark matter models, predicting a gravitational-wave signal that could be detected via future space-based gravitational-wave detectors such as LISA, DECIGO or BBO. Detecting such a signal could elucidate the nature of dark matter.

In the first publication [162], we studied the most general model of pseudo-Goldstone dark-matter arising from the complex-singlet extension of the Standard Model. In this model, the new global $U(1)$ symmetry is explicitly broken down to a CP-like symmetry stabilising dark matter. Models involving pseudo-Goldstone bosons are interesting in this regard since they have interaction proportional to momentum. Thereby, in the limit of vanishing momentum transfer, the direct-detection cross section is suppressed at tree-level, thus evading the stringent direct-detection constraints for WIMPs. In the most general model, however, this suppression will only occur in some regions of the parameter space. We found that the combination of cubic couplings which yields these blind spots does not provide a strong enough gravitational-wave signal to be detected. Nevertheless, the model predicts a detectable gravitational-wave signal in some regions of the parameter space.

In the second publication [163], we considered the inert doublet model (IDM), one of the best motivated minimal dark-matter models, in which the phase transition can occur in several steps, thus potentially generating a singular multiple-peak gravitational-wave signal. In addition to the usual one-, two- and three-step phase-transition patterns, we found a new type of two-step phase transitions where the intermediate phase is characterised by non-vanishing vacuum expectation values for both the Standard-Model Higgs and the dark-matter candidate. Unfortunately this new phase transition pattern and the three-step phase transition cannot lead to a strong enough gravitational-wave signal, while satisfying direct-detection constraints. In the end, the gravitational-wave signal is found to be mainly dominated by single-step phase transitions, which are the only ones that satisfy the dark-matter abundance constraint from the Planck mission.

Finally, in the third publication [164], we studied phase transitions and gravitational waves in the two-Higgs doublet model (2HDM), supplemented with a light pseudoscalar field, allowing a coupling between the pseudoscalar particles and a fermionic dark-matter candidate. The presence of this light pseudoscalar allows to explain for instance the CDF W-boson mass measurement [165]. We found that the gravitational-wave signal in this 2HD+a model is such that it can be potentially detected by future gravitational-wave detectors. Furthermore, by considering the 2HDM limit, we put in evidence the impact of this new light pseudoscalar field, showing that the parameter space giving rise to a detectable gravitational-wave signal is very different from the one in the 2HD+a model.

Altogether, we showed that a stochastic gravitational-wave background signal from a first-order phase transition in the early Universe is a potentially important channel to study dark matter, complementary to usual dark-matter signals such as its direct detection.

Peatükk 8

Kokkuvõte (in Estonian)

Gravitatsioonilainete avastamine aastal 2015 oli silmapaistvaks kinnituseks üldrelatiivsusteooria õigsusele. See andis uue võimaluse vaadelda tumeainet, mis on eksootilistest osakestest koosnev tundmatu aine, mis moodustab 85% terve universumi ainest. On võimalik, et varajases universumis toimunud esimest järku kosmilised faasisiirded jätsid endast maha gravitatsioonilainete tausta, mida tänapäeval saab detekteerida. Meie praegune teooria, osakestefüüsika standardmudel, ennustab teistsugust faasisiiret, sujuvat üleminekut, milles gravitatsioonilainete signaale ei teki. Tumeaine mudelite jaoks, kus faasisiire on esimest järku, on gravitatsioonilainete signaali otsimine uus võimalus tumeaine uurimiseks. Käesolevas töös “Faasisiirded ja gravitatsioonilained tumeaine mudelites” me uurisime erinevaid tumeaine mudeleid, ennustades gravitatsioonilainete signaale, mida oleks võimalik avastada tuleviku kosmoses asuvate gravitatsioonilainete detektoritega nagu LISA, DECIGO või BBO. Sellise signaali avastamine võib aidata välja selgitada tumeaine olemust.

Esimeses artiklis [162] me uurisime üldiseimat pseudo-Goldstone tumeaine mudelit, mille saame, kui lisame standardmudelile kompleksse singleti. Selles mudelis on uus globaalne $U(1)$ otseselt rikutud tumeainet stabiliseerivaks CP-sarnaseks sümmeetriaks. Mudelid, milles esinevad pseudo-Goldstone'id, on huvitavad, kuna nende osakeste vastastikmõju tugevus teiste osakestega on võrdeline üle kantud impulsiga. Seetõttu on piiril, kus see impulss on null, otsese detekteerimise ristlõige puutasemel alla surutud, mis aitab vältida rasketele nõrgalt interakteeruvatele osakestele (WIMP) kehtivaid otsese detekteerimise piiranguid. Kuid kõige üldisemas mudelis esineb see allasurumine ainult mõnes parameetrite ruumi piirkonnas. Me leidsime, et potentsiaali kuupliikmete kordajate kombinatsioonid, mis selliseid “pimetähne” annavad, ei võimalda avastamiseks piisavalt tugeva gravitatsioonilainete signaali tekkimist. Sellest hoolimata ennustab mudel avastavat gravitatsioonilainete signaali mõnes parameetrite ruumi piirkonnas.

Teises artiklis [163] uurisime inertse dubleti mudelit, üht paremini motiveeritud minimaalset tumeaine mudelit, milles faasisiire võib toimuda mitmes etapis, mistõttu gravitatsioonilainete signaalil võib mõeldavalt olla mitu tippu. Lisaks tavalistele ühe-, kahe- ja kolmeastmelistele faasisiirete tüüpidele leidsime uut tüüpi kaheastmelise faasisiirde, kus vahepealses faasis on nii standardmudeli Higgsi bosoni kui tumeaine kandidaadi vaakumi keskväärtused nullist erinevad. Kahjuks ei anna ei see uus faasisiirde tüüp ega ka kolmeastmeline faasisiire piisavalt tugevat gravitatsioonilainete signaali, kui lisaks arvesse võtta otsese detekteerimise piiranguid. Leidsime, et gravitatsioonilainete signaali domineerivad peamiselt üheastmelised faasisiirded, mis ainsana rahuldavad Plancki satelliidi mõõdetud tumeaine tihedust.

Lõpuks uurisime kolmandas artiklis [164] faasisiirdeid ja gravitatsioonilaineid kahe Higgsi dubleti mudelis (2HDM), millele on lisatud kerge pseudoskalaarne väli. Selle kerge pseudoskalaari abil on võimalik näiteks selgitada CDF-i W-bosoni massi mõõtmise tulemust [165]. Me leidsime, et ka selle 2HD+a mudeli gravitatsioonilainete signaali on põhimõtteliselt võimalik avastada tuleviku gravitatsioonilainete detektorites. Peale selle uurisime mudeli 2HDM piirjuhtu ning näitasime, et kui kerget pseudoskalaari mängus ei ole, on mudeli parameetrite ruum, milles esineb avastatav gravitatsioonilainete signaal, väga erinev 2HD+a mudeli omast.

Kokkuvõttes näitasime, et varajases universumis esimest järku faasisiirdes tekkiv stohhastiline gravitatsioonilainete signaal on potentsiaalselt oluline võimalus tumeaine uurimiseks, mis täiendab tavalisi tumeaine signaale nagu otsene detekteerimine.

Bibliography

[1] Georges Aad et al. Observation of a new particle in the search for the Standard Model Higgs boson with the ATLAS detector at the LHC. *Phys. Lett. B*, 716:1–29, 2012.

[2] Serguei Chatrchyan et al. Observation of a New Boson at a Mass of 125 GeV with the CMS Experiment at the LHC. *Phys. Lett. B*, 716:30–61, 2012.

[3] Y. Fukuda et al. Evidence for oscillation of atmospheric neutrinos. *Phys. Rev. Lett.*, 81:1562–1567, 1998.

[4] N. Aghanim et al. Planck 2018 results. VI. Cosmological parameters. *Astron. Astrophys.*, 641:A6, 2020. [Erratum: Astron.Astrophys. 652, C4 (2021)].

[5] B. P. Abbott et al. Observation of Gravitational Waves from a Binary Black Hole Merger. *Phys. Rev. Lett.*, 116(6):061102, 2016.

[6] B. P. Abbott et al. GW151226: Observation of Gravitational Waves from a 22-Solar-Mass Binary Black Hole Coalescence. *Phys. Rev. Lett.*, 116(24):241103, 2016.

[7] Edward Witten. Cosmic Separation of Phases. *Phys. Rev. D*, 30:272–285, 1984.

[8] C. J. Hogan. Gravitational radiation from cosmological phase transitions. *Mon. Not. Roy. Astron. Soc.*, 218:629–636, 1986.

[9] K. Kajantie, M. Laine, K. Rummukainen, and Mikhail E. Shaposhnikov. Is there a hot electroweak phase transition at $m_H \gtrsim m_W$? *Phys. Rev. Lett.*, 77:2887–2890, 1996.

[10] Pau Amaro-Seoane et al. Laser Interferometer Space Antenna. 2 2017.

[11] Matthew D. Schwartz. *Quantum Field Theory and the Standard Model*. Cambridge University Press, 3 2014.

[12] Franz Mandl and Graham Shaw. *QUANTUM FIELD THEORY*. 1985.

[13] Yu-Pan Zeng, Xiang Xiao, and Wei Wang. Constraints on Pseudo-Nambu-Goldstone dark matter from direct detection experiment and neutron star reheating temperature. *Phys. Lett. B*, 824:136822, 2022.

[14] Michael E. Peskin and Daniel V. Schroeder. *An Introduction to quantum field theory*. Addison-Wesley, Reading, USA, 1995.

[15] F. Zwicky. Die Rotverschiebung von extragalaktischen Nebeln. *Helv. Phys. Acta*, 6:110–127, 1933.

[16] V. C. Rubin, N. Thonnard, and W. K. Ford, Jr. Rotational properties of 21 SC galaxies with a large range of luminosities and radii, from NGC 4605 /R = 4kpc/ to UGC 2885 /R = 122 kpc/. *Astrophys. J.*, 238:471, 1980.

[17] Douglas Clowe, Marusa Bradac, Anthony H. Gonzalez, Maxim Markevitch, Scott W. Randall, Christine Jones, and Dennis Zaritsky. A direct empirical proof of the existence of dark matter. *Astrophys. J. Lett.*, 648:L109–L113, 2006.

[18] A. Arbey and F. Mahmoudi. Dark matter and the early Universe: a review. *Prog. Part. Nucl. Phys.*, 119:103865, 2021.

[19] Stefano Profumo. *An Introduction to Particle Dark Matter.* World Scientific, 2017.

[20] Lars Bergström. Nonbaryonic dark matter: Observational evidence and detection methods. *Rept. Prog. Phys.*, 63:793, 2000.

[21] David H. Weinberg, Rupert A. C. Croft, Lars Hernquist, Neal Katz, and Max Pettinini. Closing in on omega(0): The Amplitude of mass fluctuations from galaxy clusters and the Lyman alpha forest. *Astrophys. J.*, 522:563, 1999.

[22] John M. O'Meara, David Tytler, David Kirkman, Nao Suzuki, Jason X. Prochaska, Dan Lubin, and Arthur M. Wolfe. The Deuterium to hydrogen abundance ratio towards a fourth QSO: HS 0105 + 1619. *Astrophys. J.*, 552:718–730, 2001.

[23] Edward W. Kolb and Michael S. Turner. The Early Universe. *Nature*, 294:521, 1981.

[24] Steven Weinberg. *Gravitation and Cosmology: Principles and Applications of the General Theory of Relativity.* John Wiley and Sons, New York, 1972.

[25] Paolo Gondolo and Graciela Gelmini. Cosmic abundances of stable particles: Improved analysis. *Nucl. Phys. B*, 360:145–179, 1991.

[26] Kensuke Akita and Masahide Yamaguchi. A Review of Neutrino Decoupling from the Early Universe to the Current Universe. *Universe*, 8(11):552, 2022.

[27] G. Mangano, G. Miele, S. Pastor, and M. Peloso. A Precision calculation of the effective number of cosmological neutrinos. *Phys. Lett. B*, 534:8–16, 2002.

[28] M. Mulders and C. Duhr, editors. *Proceedings, 2018 European School of High-Energy Physics (ESHEP 2018): Maratea, Italy, June 20 – July 3 2018*, volume 6/2019 of *CERN Yellow Reports: School Proceedings*, Geneva, 2019. CERN.

[29] Jonathan L. Feng. Supersymmetry and cosmology. *eConf*, C0307282:L11, 2003.

[30] Jonathan L. Feng and Jason Kumar. The WIMPless Miracle: Dark-Matter Particles without Weak-Scale Masses or Weak Interactions. *Phys. Rev. Lett.*, 101:231301, 2008.

[31] Kim Griest and Marc Kamionkowski. Unitarity Limits on the Mass and Radius of Dark Matter Particles. *Phys. Rev. Lett.*, 64:615, 1990.

[32] Benjamin W. Lee and Steven Weinberg. Cosmological Lower Bound on Heavy Neutrino Masses. *Phys. Rev. Lett.*, 39:165–168, 1977.

[33] Peter J. Mohr, Barry N. Taylor, and David B. Newell. CODATA recommended values of the fundamental physical constants: 2010. *Reviews of Modern Physics*, 84(4):1527–1605, nov 2012.

[34] Kim Griest and David Seckel. Three exceptions in the calculation of relic abundances. *Phys. Rev. D*, 43:3191–3203, 1991.

[35] Mark W. Goodman and Edward Witten. Detectability of Certain Dark Matter Candidates. *Phys. Rev. D*, 31:3059, 1985.

[36] G. Barello, Spencer Chang, and Christopher A. Newby. A Model Independent Approach to Inelastic Dark Matter Scattering. *Phys. Rev. D*, 90(9):094027, 2014.

[37] Martin Bauer and Tilman Plehn. *Yet Another Introduction to Dark Matter: The Particle Physics Approach*, volume 959 of *Lecture Notes in Physics*. Springer, 2019.

[38] Paolo Gondolo. Phenomenological introduction to direct dark matter detection. In *31st Rencontres de Moriond: Dark Matter and Cosmology, Quantum Measurements and Experimental Gravitation*, pages 41–51, 1996.

[39] Richard W. Schnee. Introduction to dark matter experiments. In *Theoretical Advanced Study Institute in Elementary Particle Physics: Physics of the Large and the Small*, pages 775–829, 2011.

[40] Andriy Kurylov and Marc Kamionkowski. Generalized analysis of weakly interacting massive particle searches. *Phys. Rev. D*, 69:063503, 2004.

[41] Leszek Roszkowski, Enrico Maria Sessolo, and Sebastian Trojanowski. WIMP dark matter candidates and searches—current status and future prospects. *Rept. Prog. Phys.*, 81(6):066201, 2018.

[42] Teresa Marrodán Undagoitia and Ludwig Rauch. Dark matter direct-detection experiments. *J. Phys. G*, 43(1):013001, 2016.

[43] Marc Schumann. Direct Detection of WIMP Dark Matter: Concepts and Status. *J. Phys. G*, 46(10):103003, 2019.

[44] Keith R. Dienes, Jason Kumar, Brooks Thomas, and David Yaylali. Overcoming Velocity Suppression in Dark-Matter Direct-Detection Experiments. *Phys. Rev. D*, 90(1):015012, 2014.

[45] E. Aprile et al. Dark Matter Search Results from a One Ton-Year Exposure of XENON1T. *Phys. Rev. Lett.*, 121(11):111302, 2018.

[46] Yue Meng et al. Dark Matter Search Results from the PandaX-4T Commissioning Run. *Phys. Rev. Lett.*, 127(26):261802, 2021.

[47] J. Aalbers et al. First Dark Matter Search Results from the LUX-ZEPLIN (LZ) Experiment. 7 2022.

[48] E. Aprile et al. First Dark Matter Search with Nuclear Recoils from the XENONnT Experiment. 3 2023.

[49] Laura Baudis. WIMP Dark Matter Direct-Detection Searches in Noble Gases. *Phys. Dark Univ.*, 4:50–59, 2014.

[50] Sidney R. Coleman and Erick J. Weinberg. Radiative Corrections as the Origin of Spontaneous Symmetry Breaking. *Phys. Rev. D*, 7:1888–1910, 1973.

[51] Mariano Quiros. Finite temperature field theory and phase transitions. In *ICTP Summer School in High-Energy Physics and Cosmology*, pages 187–259, 1 1999.

[52] Glauber Carvalho Dorsch. *The electroweak phase transition in two-Higgs-doublet models and implications for LHC searches.* PhD thesis, Sussex U., 2016.

[53] Cedric Delaunay, Christophe Grojean, and James D. Wells. Dynamics of Non-renormalizable Electroweak Symmetry Breaking. *JHEP*, 04:029, 2008.

[54] P. Basler, M. Krause, M. Muhlleitner, J. Wittbrodt, and A. Wlotzka. Strong First Order Electroweak Phase Transition in the CP-Conserving 2HDM Revisited. *JHEP*, 02:121, 2017.

[55] J. I. Kapusta and Charles Gale. *Finite-temperature field theory: Principles and applications.* Cambridge Monographs on Mathematical Physics. Cambridge University Press, 2011.

[56] Mikko Laine and Aleksi Vuorinen. *Basics of Thermal Field Theory*, volume 925. Springer, 2016.

[57] L. Dolan and R. Jackiw. Symmetry Behavior at Finite Temperature. *Phys. Rev. D*, 9:3320–3341, 1974.

[58] David Curtin, Patrick Meade, and Harikrishnan Ramani. Thermal Resummation and Phase Transitions. *Eur. Phys. J. C*, 78(9):787, 2018.

[59] M. E. Carrington. The Effective potential at finite temperature in the Standard Model. *Phys. Rev. D*, 45:2933–2944, 1992.

[60] Rajesh R. Parwani. Resummation in a hot scalar field theory. *Phys. Rev. D*, 45:4695, 1992. [Erratum: Phys.Rev.D 48, 5965 (1993)].

[61] Francesco Sannino and Jussi Virkajärvi. First Order Electroweak Phase Transition from (Non)Conformal Extensions of the Standard Model. *Phys. Rev. D*, 92(4):045015, 2015.

[62] J. R. Espinosa, M. Quiros, and F. Zwirner. On the nature of the electroweak phase transition. *Phys. Lett. B*, 314:206–216, 1993.

[63] Eibun Senaha. Symmetry Restoration and Breaking at Finite Temperature: An Introductory Review. *Symmetry*, 12(5):733, 2020.

[64] A. Rebhan. Thermal gauge field theories. *Lect. Notes Phys.*, 583:161–208, 2002.

[65] Jean-Paul Blaizot, Edmond Iancu, and Rajesh R. Parwani. On the screening of static electromagnetic fields in hot QED plasmas. *Phys. Rev. D*, 52:2543–2562, 1995.

[66] Erick J. Weinberg and Ai-qun Wu. UNDERSTANDING COMPLEX PERTURBATIVE EFFECTIVE POTENTIALS. *Phys. Rev. D*, 36:2474, 1987.

[67] James M. Cline and Pierre-Anthony Lemieux. Electroweak phase transition in two Higgs doublet models. *Phys. Rev. D*, 55:3873–3881, 1997.

[68] Moritz Breitbach, Joachim Kopp, Eric Madge, Toby Opferkuch, and Pedro Schwaller. Dark, Cold, and Noisy: Constraining Secluded Hidden Sectors with Gravitational Waves. *JCAP*, 07:007, 2019.

[69] Oliver Gould and Tuomas V. I. Tenkanen. On the perturbative expansion at high temperature and implications for cosmological phase transitions. *JHEP*, 06:069, 2021.

[70] Rong-Gen Cai, Misao Sasaki, and Shao-Jiang Wang. The gravitational waves from the first-order phase transition with a dimension-six operator. *JCAP*, 08:004, 2017.

[71] Andreas Ekstedt and Johan Löfgren. A Critical Look at the Electroweak Phase Transition. *JHEP*, 12:136, 2020.

[72] Djuna Croon, Oliver Gould, Philipp Schicho, Tuomas V. I. Tenkanen, and Graham White. Theoretical uncertainties for cosmological first-order phase transitions. *JHEP*, 04:055, 2021.

[73] M. Laine. Gauge dependence of the high temperature two loop effective potential for the Higgs field. *Phys. Rev. D*, 51:4525–4532, 1995.

[74] Hiren H. Patel and Michael J. Ramsey-Musolf. Baryon Washout, Electroweak Phase Transition, and Perturbation Theory. *JHEP*, 07:029, 2011.

[75] Cheng-Wei Chiang, Yen-Ting Li, and Eibun Senaha. Revisiting electroweak phase transition in the standard model with a real singlet scalar. *Phys. Lett. B*, 789:154–159, 2019.

[76] Peter Athron, Csaba Balazs, Andrew Fowlie, Lachlan Morris, Graham White, and Yang Zhang. How arbitrary are perturbative calculations of the electroweak phase transition? *JHEP*, 01:050, 2023.

[77] Sidney R. Coleman. The Fate of the False Vacuum. 1. Semiclassical Theory. *Phys. Rev. D*, 15:2929–2936, 1977. [Erratum: Phys.Rev.D 16, 1248 (1977)].

[78] Sidney R. Coleman, V. Glaser, and Andre Martin. Action Minima Among Solutions to a Class of Euclidean Scalar Field Equations. *Commun. Math. Phys.*, 58:211–221, 1978.

[79] Curtis G. Callan, Jr. and Sidney R. Coleman. The Fate of the False Vacuum. 2. First Quantum Corrections. *Phys. Rev. D*, 16:1762–1768, 1977.

[80] Andrei D. Linde. Fate of the False Vacuum at Finite Temperature: Theory and Applications. *Phys. Lett. B*, 100:37–40, 1981.

[81] Andrei D. Linde. Decay of the False Vacuum at Finite Temperature. *Nucl. Phys. B*, 216:421, 1983. [Erratum: Nucl.Phys.B 223, 544 (1983)].

[82] D. Bodeker, W. Buchmuller, Z. Fodor, and T. Helbig. Aspects of the cosmological electroweak phase transition. *Nucl. Phys. B*, 423:171–196, 1994.

[83] Luigi Delle Rose, Carlo Marzo, and Alfredo Urbano. On the fate of the Standard Model at finite temperature. *JHEP*, 05:050, 2016.

[84] Greg W. Anderson and Lawrence J. Hall. The Electroweak phase transition and baryogenesis. *Phys. Rev. D*, 45:2685–2698, 1992.

[85] John Ellis, Marek Lewicki, and José Miguel No. On the Maximal Strength of a First-Order Electroweak Phase Transition and its Gravitational Wave Signal. *JCAP*, 04:003, 2019.

[86] Rabindra N. Mohapatra and Goran Senjanovic. Soft CP Violation at High Temperature. *Phys. Rev. Lett.*, 42:1651, 1979.

[87] Rabindra N. Mohapatra and Goran Senjanovic. Broken Symmetries at High Temperature. *Phys. Rev. D*, 20:3390–3398, 1979.

[88] Steven Weinberg. Gauge and Global Symmetries at High Temperature. *Phys. Rev. D*, 9:3357–3378, 1974.

[89] Ki-Myeong Lee and Erick J. Weinberg. TUNNELING WITHOUT BARRIERS. *Nucl. Phys. B*, 267:181–202, 1986.

[90] Anders Andreassen, David Farhi, William Frost, and Matthew D. Schwartz. Precision decay rate calculations in quantum field theory. *Phys. Rev. D*, 95(8):085011, 2017.

[91] M. Laine and K. Rummukainen. What's new with the electroweak phase transition? *Nucl. Phys. B Proc. Suppl.*, 73:180–185, 1999.

[92] Leonardo Leitao, Ariel Megevand, and Alejandro D. Sanchez. Gravitational waves from the electroweak phase transition. *JCAP*, 10:024, 2012.

[93] Vinod K.S. Shante and Scott Kirkpatrick. An introduction to percolation theory. *Advances in Physics*, 20(85):325–357, 1971.

[94] Alan H. Guth and Erick J. Weinberg. Cosmological Consequences of a First Order Phase Transition in the SU(5) Grand Unified Model. *Phys. Rev. D*, 23:876, 1981.

[95] John Ellis, Marek Lewicki, and Ville Vaskonen. Updated predictions for gravitational waves produced in a strongly supercooled phase transition. *JCAP*, 11:020, 2020.

[96] Chiara Caprini et al. Science with the space-based interferometer eLISA. II: Gravitational waves from cosmological phase transitions. *JCAP*, 04:001, 2016.

[97] Xiao Wang, Fa Peng Huang, and Xinmin Zhang. Phase transition dynamics and gravitational wave spectra of strong first-order phase transition in supercooled universe. *JCAP*, 05:045, 2020.

[98] Thomas Biekötter, Sven Heinemeyer, José Miguel No, María Olalla Olea-Romacho, and Georg Weiglein. The trap in the early Universe: impact on the interplay between gravitational waves and LHC physics in the 2HDM. *JCAP*, 03:031, 2023.

[99] James M. Cline. Baryogenesis. In *Les Houches Summer School - Session 86: Particle Physics and Cosmology: The Fabric of Spacetime*, 9 2006.

[100] David E. Morrissey and Michael J. Ramsey-Musolf. Electroweak baryogenesis. *New J. Phys.*, 14:125003, 2012.

[101] Pierre Auclair et al. Cosmology with the Laser Interferometer Space Antenna. 4 2022.

[102] Michael Geller, Anson Hook, Raman Sundrum, and Yuhsin Tsai. Primordial Anisotropies in the Gravitational Wave Background from Cosmological Phase Transitions. *Phys. Rev. Lett.*, 121(20):201303, 2018.

[103] Jose R. Espinosa, Thomas Konstandin, Jose M. No, and Geraldine Servant. Energy Budget of Cosmological First-order Phase Transitions. *JCAP*, 06:028, 2010.

[104] Marcus Bluhm. Qcd equation of state of hot deconfined matter at finite baryon density. a quasiparticle perspective. Dec 2008.

[105] Sz. Horvat, Volodymyr K. Magas, Daniel D. Strottman, and Laszlo P. Csernai. Entropy development in ideal relativistic fluid dynamics with the Bag Model equation of state. *Phys. Lett. B*, 692:277–280, 2010.

[106] Felix Giese, Thomas Konstandin, and Jorinde van de Vis. Model-independent energy budget of cosmological first-order phase transitions—A sound argument to go beyond the bag model. *JCAP*, 07(07):057, 2020.

[107] Marc Kamionkowski, Arthur Kosowsky, and Michael S. Turner. Gravitational radiation from first order phase transitions. *Phys. Rev. D*, 49:2837–2851, 1994.

[108] Chiara Caprini et al. Detecting gravitational waves from cosmological phase transitions with LISA: an update. *JCAP*, 03:024, 2020.

[109] Mark Hindmarsh, Stephan J. Huber, Kari Rummukainen, and David J. Weir. Numerical simulations of acoustically generated gravitational waves at a first order phase transition. *Phys. Rev. D*, 92(12):123009, 2015.

[110] Mark Hindmarsh and Mulham Hijazi. Gravitational waves from first order cosmological phase transitions in the Sound Shell Model. *JCAP*, 12:062, 2019.

[111] Christophe Grojean and Geraldine Servant. Gravitational Waves from Phase Transitions at the Electroweak Scale and Beyond. *Phys. Rev. D*, 75:043507, 2007.

[112] Michael S. Turner, Erick J. Weinberg, and Lawrence M. Widrow. Bubble nucleation in first order inflation and other cosmological phase transitions. *Phys. Rev. D*, 46:2384–2403, 1992.

[113] Michele Maggiore. *Gravitational Waves. Vol. 1: Theory and Experiments*. Oxford University Press, 2007.

[114] Michele Maggiore. Gravitational wave experiments and early universe cosmology. *Phys. Rept.*, 331:283–367, 2000.

[115] Mark Hindmarsh, Stephan J. Huber, Kari Rummukainen, and David J. Weir. Gravitational waves from the sound of a first order phase transition. *Phys. Rev. Lett.*, 112:041301, 2014.

[116] Chiara Caprini, Ruth Durrer, and Geraldine Servant. The stochastic gravitational wave background from turbulence and magnetic fields generated by a first-order phase transition. *JCAP*, 12:024, 2009.

[117] Ryusuke Jinno, Bibhushan Shakya, and Jorinde van de Vis. Gravitational Waves from Feebly Interacting Particles in a First Order Phase Transition. 11 2022.

[118] Kai Schmitz. New Sensitivity Curves for Gravitational-Wave Signals from Cosmological Phase Transitions. *JHEP*, 01:097, 2021.

[119] Dietrich Bodeker and Guy D. Moore. Can electroweak bubble walls run away? *JCAP*, 05:009, 2009.

[120] Marek Lewicki, Ville Vaskonen, and Hardi Veermäe. Bubble dynamics in fluids with N-body simulations. *Phys. Rev. D*, 106(10):103501, 2022.

[121] Stefan Höche, Jonathan Kozaczuk, Andrew J. Long, Jessica Turner, and Yikun Wang. Towards an all-orders calculation of the electroweak bubble wall velocity. *JCAP*, 03:009, 2021.

[122] Dietrich Bodeker and Guy D. Moore. Electroweak Bubble Wall Speed Limit. *JCAP*, 05:025, 2017.

[123] Aleksandr Azatov and Miguel Vanvlasselaer. Bubble wall velocity: heavy physics effects. *JCAP*, 01:058, 2021.

[124] John Ellis, Marek Lewicki, José Miguel No, and Ville Vaskonen. Gravitational wave energy budget in strongly supercooled phase transitions. *JCAP*, 06:024, 2019.

[125] Arthur Kosowsky, Michael S. Turner, and Richard Watkins. Gravitational radiation from colliding vacuum bubbles. *Phys. Rev. D*, 45:4514–4535, 1992.

[126] Arthur Kosowsky, Michael S. Turner, and Richard Watkins. Gravitational waves from first order cosmological phase transitions. *Phys. Rev. Lett.*, 69:2026–2029, 1992.

[127] Arthur Kosowsky and Michael S. Turner. Gravitational radiation from colliding vacuum bubbles: envelope approximation to many bubble collisions. *Phys. Rev. D*, 47:4372–4391, 1993.

[128] Ryusuke Jinno and Masahiro Takimoto. Gravitational waves from bubble dynamics: Beyond the Envelope. *JCAP*, 01:060, 2019.

[129] Thomas Konstandin. Gravitational radiation from a bulk flow model. *JCAP*, 03:047, 2018.

[130] Daniel Cutting, Mark Hindmarsh, and David J. Weir. Gravitational waves from vacuum first-order phase transitions: from the envelope to the lattice. *Phys. Rev. D*, 97(12):123513, 2018.

[131] Hillary L. Child and John T. Giblin, Jr. Gravitational Radiation from First-Order Phase Transitions. *JCAP*, 10:001, 2012.

[132] Stephan J. Huber and Thomas Konstandin. Gravitational Wave Production by Collisions: More Bubbles. *JCAP*, 09:022, 2008.

[133] Moritz Breitbach. Gravitational Waves from Cosmological Phase Transitions. Master's thesis, Mainz U., 2018.

[134] Fatih Ertas, Felix Kahlhoefer, and Carlo Tasillo. Turn up the volume: listening to phase transitions in hot dark sectors. *JCAP*, 02(02):014, 2022.

[135] Mark Hindmarsh. Sound shell model for acoustic gravitational wave production at a first-order phase transition in the early Universe. *Phys. Rev. Lett.*, 120(7):071301, 2018.

[136] Mark Hindmarsh, Stephan J. Huber, Kari Rummukainen, and David J. Weir. Shape of the acoustic gravitational wave power spectrum from a first order phase transition. *Phys. Rev. D*, 96(10):103520, 2017. [Erratum: Phys.Rev.D 101, 089902 (2020)].

[137] Kai Schmitz. LISA Sensitivity to Gravitational Waves from Sound Waves. *Symmetry*, 12(9):1477, 2020.

[138] Marek Lewicki, Oriol Pujolàs, and Ville Vaskonen. Escape from supercooling with or without bubbles: gravitational wave signatures. *Eur. Phys. J. C*, 81(9):857, 2021.

[139] Huai-Ke Guo, Kuver Sinha, Daniel Vagie, and Graham White. Phase Transitions in an Expanding Universe: Stochastic Gravitational Waves in Standard and Non-Standard Histories. *JCAP*, 01:001, 2021.

[140] Chiara Caprini and Daniel G. Figueroa. Cosmological Backgrounds of Gravitational Waves. *Class. Quant. Grav.*, 35(16):163001, 2018.

[141] Seiji Kawamura et al. The Japanese space gravitational wave antenna: DECIGO. *Class. Quant. Grav.*, 28:094011, 2011.

[142] Vincent Corbin and Neil J. Cornish. Detecting the cosmic gravitational wave background with the big bang observer. *Class. Quant. Grav.*, 23:2435–2446, 2006.

[143] Wen-Rui Hu and Yue-Liang Wu. The Taiji Program in Space for gravitational wave physics and the nature of gravity. *Natl. Sci. Rev.*, 4(5):685–686, 2017.

[144] Jun Luo et al. TianQin: a space-borne gravitational wave detector. *Class. Quant. Grav.*, 33(3):035010, 2016.

[145] M. C. Guzzetti, N. Bartolo, M. Liguori, and S. Matarrese. Gravitational waves from inflation. *Riv. Nuovo Cim.*, 39(9):399–495, 2016.

[146] Nicola Bartolo et al. Science with the space-based interferometer LISA. IV: Probing inflation with gravitational waves. *JCAP*, 12:026, 2016.

[147] Matthew R. DePies and Craig J. Hogan. Stochastic Gravitational Wave Background from Light Cosmic Strings. *Phys. Rev. D*, 75:125006, 2007.

[148] Yann Gouttenoire, Géraldine Servant, and Peera Simakachorn. BSM with Cosmic Strings: Heavy, up to EeV mass, Unstable Particles. *JCAP*, 07:016, 2020.

[149] Wilfried Buchmuller, Valerie Domcke, and Kai Schmitz. Stochastic gravitational-wave background from metastable cosmic strings. *JCAP*, 12(12):006, 2021.

[150] Sebastien Clesse, Juan García-Bellido, and Stefano Orani. Detecting the Stochastic Gravitational Wave Background from Primordial Black Hole Formation. 12 2018.

[151] Juan García-Bellido, Santiago Jaraba, and Sachiko Kuroyanagi. The stochastic gravitational wave background from close hyperbolic encounters of primordial black holes in dense clusters. *Phys. Dark Univ.*, 36:101009, 2022.

[152] Stanislav Babak, Chiara Caprini, Daniel G. Figueroa, Nikolaos Karnesis, Paolo Marcoccia, Germano Nardini, Mauro Pieroni, Angelo Ricciardone, Alberto Sesana, and Jesús Torrado. Stochastic gravitational wave background from stellar origin binary black holes in LISA. 4 2023.

[153] Arianna I. Renzini, Boris Goncharov, Alexander C. Jenkins, and Pat M. Meyers. Stochastic Gravitational-Wave Backgrounds: Current Detection Efforts and Future Prospects. *Galaxies*, 10(1):34, 2022.

[154] Nelson Christensen. Stochastic Gravitational Wave Backgrounds. *Rept. Prog. Phys.*, 82(1):016903, 2019.

[155] Massimo Tinto, J. W. Armstrong, and F. B. Estabrook. Discriminating a gravitational wave background from instrumental noise in the LISA detector. *Phys. Rev. D*, 63:021101, 2001.

[156] Craig J. Hogan and Peter L. Bender. Estimating stochastic gravitational wave backgrounds with Sagnac calibration. *Phys. Rev. D*, 64:062002, 2001.

[157] Matthew R. Adams and Neil J. Cornish. Discriminating between a Stochastic Gravitational Wave Background and Instrument Noise. *Phys. Rev. D*, 82:022002, 2010.

[158] Matthew R. Adams and Neil J. Cornish. Detecting a Stochastic Gravitational Wave Background in the presence of a Galactic Foreground and Instrument Noise. *Phys. Rev. D*, 89(2):022001, 2014.

[159] Eric Thrane and Joseph D. Romano. Sensitivity curves for searches for gravitational-wave backgrounds. *Phys. Rev. D*, 88(12):124032, 2013.

[160] Aleksandr Azatov, Daniele Barducci, and Francesco Sgarlata. Gravitational traces of broken gauge symmetries. *JCAP*, 07:027, 2020.

[161] Tommi Alanne, Thomas Hugle, Moritz Platscher, and Kai Schmitz. A fresh look at the gravitational-wave signal from cosmological phase transitions. *JHEP*, 03:004, 2020.

[162] Tommi Alanne, Nico Benincasa, Matti Heikinheimo, Kristjan Kannike, Venus Keus, Niko Koivunen, and Kimmo Tuominen. Pseudo-Goldstone dark matter: gravitational waves and direct-detection blind spots. *JHEP*, 10:080, 2020.

[163] Nico Benincasa, Luigi Delle Rose, Kristjan Kannike, and Luca Marzola. Multi-step phase transitions and gravitational waves in the inert doublet model. *JCAP*, 12:025, 2022.

[164] Giorgio Arcadi, Nico Benincasa, Abdelhak Djouadi, and Kristjan Kannike. Two-Higgs-doublet-plus-pseudoscalar model: Collider, dark matter, and gravitational wave signals. *Phys. Rev. D*, 108(5):055010, 2023.

[165] T. Aaltonen et al. High-precision measurement of the W boson mass with the CDF II detector. *Science*, 376(6589):170–176, 2022.

Publications

Curriculum Vitae

Name:	Nico Benincasa
Date and place of birth:	December 20, 1994, Anderlecht, Belgium
Citizenship:	Belgian
Address:	National Institute of Chemical Physics and Biophysics, Rävala 10, Tallinn 10143, Estonia
E-mail:	nico.benincasa@kbfi.ee/ nico.alexis.benincasa@ut.ee

Education

2019-2023	Doctoral student in physics (theoretical physics), National Institute of Chemical Physics and Biophysics and University of Tartu
2015-2017	MSc in space sciences, University of Liège
2012-2015	BSc in physics, University of Liège
2006-2012	Secondary education, Athénée Royal Paul Brusson, Belgium

Elulookirjeldus

Nimi:	Nico Benincasa
Sünniaeg ja koht:	20. detsember, 1994, Anderlecht, Belgia
Kodakondsus:	Belgia
Aadress:	Keemilise ja Bioloogilise Füüsika Instituut, Rävala 10, Tallinn 10143, Eesti
E-post:	nico.benincasa@kbfi.ee/ nico.alexis.benincasa@ut.ee

Haridus

2019-2023	Füüsikadoktorant (teoreetiline füüsika), Keemilise ja Bioloogilise Füüsika Instituut ja Tartu Ülikool
2015-2017	MSc kosmoseteadustes, Liège'i ülikool
2012-2015	BSc füüsikas, Liège'i ülikool
2006-2012	Gümnaasium, Athénée Royal Paul Brusson, Belgia

DISSERTATIONES PHYSICAE UNIVERSITATIS TARTUENSIS

1. **Andrus Ausmees.** XUV-induced electron emission and electron-phonon interaction in alkali halides. Tartu, 1991.
2. **Heiki Sõnajalg.** Shaping and recalling of light pulses by optical elements based on spectral hole burning. Tartu, 1991.
3. **Sergei Savihhin.** Ultrafast dynamics of F-centers and bound excitons from picosecond spectroscopy data. Tartu, 1991.
4. **Ergo Nõmmiste.** Leelishalogeniidide röntgenelektronemissioon kiiritamisel footonitega energiaga 70–140 eV. Tartu, 1991.
5. **Margus Rätsep.** Spectral gratings and their relaxation in some low-temperature impurity-doped glasses and crystals. Tartu, 1991.
6. **Tõnu Pullerits.** Primary energy transfer in photosynthesis. Model calculations. Tartu, 1991.
7. **Olev Saks.** Attoampri diapasoonis voolude mõõtmise füüsikalised alused. Tartu, 1991.
8. **Andres Virro.** AlGaAsSb/GaSb heterostructure injection lasers. Tartu, 1991.
9. **Hans Korge.** Investigation of negative point discharge in pure nitrogen at atmospheric pressure. Tartu, 1992.
10. **Jüri Maksimov.** Nonlinear generation of laser VUV radiation for high-resolution spectroscopy. Tartu, 1992.
11. **Mark Aizengendler.** Photostimulated transformation of aggregate defects and spectral hole burning in a neutron-irradiated sapphire. Tartu, 1992.
12. **Hele Siimon.** Atomic layer molecular beam epitaxy of A^2B^6 compounds described on the basis of kinetic equations model. Tartu, 1992.
13. **Tõnu Reinot.** The kinetics of polariton luminescence, energy transfer and relaxation in anthracene. Tartu, 1992.
14. **Toomas Rõõm.** Paramagnetic H^{2-} and F^+ centers in CaO crystals: spectra, relaxation and recombination luminescence. Tallinn, 1993.
15. **Erko Jalviste.** Laser spectroscopy of some jet-cooled organic molecules. Tartu, 1993.
16. **Alvo Aabloo.** Studies of crystalline celluloses using potential energy calculations. Tartu, 1994.
17. **Peeter Paris.** Initiation of corona pulses. Tartu, 1994.
18. **Павел Рубин.** Локальные дефектные состояния в CuO_2 плоскостях высокотемпературных сверхпроводников. Тарту, 1994.
19. **Olavi Ollikainen.** Applications of persistent spectral hole burning in ultrafast optical neural networks, time-resolved spectroscopy and holographic interferometry. Tartu, 1996.
20. **Ülo Mets.** Methodological aspects of fluorescence correlation spectroscopy. Tartu, 1996.
21. **Mikhail Danilkin.** Interaction of intrinsic and impurity defects in CaS:Eu luminophors. Tartu, 1997.

22. **Ирина Кудрявцева.** Создание и стабилизация дефектов в кристаллах KBr, KCl, RbCl при облучении ВУФ-радиацией. Тарту, 1997.
23. **Andres Osvet.** Photochromic properties of radiation-induced defects in diamond. Tartu, 1998.
24. **Jüri Örd.** Classical and quantum aspects of geodesic multiplication. Tartu, 1998.
25. **Priit Sarv.** High resolution solid-state NMR studies of zeolites. Tartu, 1998.
26. **Сергей Долгов.** Электронные возбуждения и дефектообразование в некоторых оксидах металлов. Тарту, 1998.
27. **Kaupo Kukli.** Atomic layer deposition of artificially structured dielectric materials. Tartu, 1999.
28. **Ivo Heinmaa.** Nuclear resonance studies of local structure in $RBa_2Cu_3O_{6+x}$ compounds. Tartu, 1999.
29. **Aleksander Shelkan.** Hole states in CuO_2 planes of high temperature superconducting materials. Tartu, 1999.
30. **Dmitri Nevedrov.** Nonlinear effects in quantum lattices. Tartu, 1999.
31. **Rein Ruus.** Collapse of 3d (4f) orbitals in 2p (3d) excited configurations and its effect on the x-ray and electron spectra. Tartu, 1999.
32. **Valter Zazubovich.** Local relaxation in incommensurate and glassy solids studied by Spectral Hole Burning. Tartu, 1999.
33. **Indrek Reimand.** Picosecond dynamics of optical excitations in GaAs and other excitonic systems. Tartu, 2000.
34. **Vladimir Babin.** Spectroscopy of exciton states in some halide macro- and nanocrystals. Tartu, 2001.
35. **Toomas Plank.** Positive corona at combined DC and AC voltage. Tartu, 2001.
36. **Kristjan Leiger.** Pressure-induced effects in inhomogeneous spectra of doped solids. Tartu, 2002.
37. **Helle Kaasik.** Nonperturbative theory of multiphonon vibrational relaxation and nonradiative transitions. Tartu, 2002.
38. **Tõnu Laas.** Propagation of waves in curved spacetimes. Tartu, 2002.
39. **Rünno Lõhmus.** Application of novel hybrid methods in SPM studies of nanostructural materials. Tartu, 2002.
40. **Kaido Reivelt.** Optical implementation of propagation-invariant pulsed free-space wave fields. Tartu, 2003.
41. **Heiki Kasemägi.** The effect of nanoparticle additives on lithium-ion mobility in a polymer electrolyte. Tartu, 2003.
42. **Villu Repän.** Low current mode of negative corona. Tartu, 2004.
43. **Алексей Котлов.** Оксианионные диэлектрические кристаллы: зонная структура и электронные возбуждения. Tartu, 2004.
44. **Jaak Talts.** Continuous non-invasive blood pressure measurement: comparative and methodological studies of the differential servo-oscillometric method. Tartu, 2004.
45. **Margus Saal.** Studies of pre-big bang and braneworld cosmology. Tartu, 2004.

46. **Eduard Gerškevitš.** Dose to bone marrow and leukaemia risk in external beam radiotherapy of prostate cancer. Tartu, 2005.
47. **Sergey Shchemelyov.** Sum-frequency generation and multiphoton ionization in xenon under excitation by conical laser beams. Tartu, 2006.
48. **Valter Kiisk.** Optical investigation of metal-oxide thin films. Tartu, 2006.
49. **Jaan Aarik.** Atomic layer deposition of titanium, zirconium and hafnium dioxides: growth mechanisms and properties of thin films. Tartu, 2007.
50. **Astrid Rekker.** Colored-noise-controlled anomalous transport and phase transitions in complex systems. Tartu, 2007.
51. **Andres Punning.** Electromechanical characterization of ionic polymer-metal composite sensing actuators. Tartu, 2007.
52. **Indrek Jõgi.** Conduction mechanisms in thin atomic layer deposited films containing TiO_2. Tartu, 2007.
53. **Aleksei Krasnikov.** Luminescence and defects creation processes in lead tungstate crystals. Tartu, 2007.
54. **Küllike Rägo.** Superconducting properties of MgB_2 in a scenario with intra- and interband pairing channels. Tartu, 2008.
55. **Els Heinsalu.** Normal and anomalously slow diffusion under external fields. Tartu, 2008.
56. **Kuno Kooser.** Soft x-ray induced radiative and nonradiative core-hole decay processes in thin films and solids. Tartu, 2008.
57. **Vadim Boltrushko.** Theory of vibronic transitions with strong nonlinear vibronic interaction in solids. Tartu, 2008.
58. **Andi Hektor.** Neutrino Physics beyond the Standard Model. Tartu, 2008.
59. **Raavo Josepson.** Photoinduced field-assisted electron emission into gases. Tartu, 2008.
60. **Martti Pärs.** Study of spontaneous and photoinduced processes in molecular solids using high-resolution optical spectroscopy. Tartu, 2008.
61. **Kristjan Kannike.** Implications of neutrino masses. Tartu, 2008.
62. **Vigen Issahhanjan.** Hole and interstitial centres in radiation-resistant MgO single crystals. Tartu, 2008.
63. **Veera Krasnenko.** Computational modeling of fluorescent proteins. Tartu, 2008.
64. **Mait Müntel.** Detection of doubly charged higgs boson in the CMS detector. Tartu, 2008.
65. **Kalle Kepler.** Optimisation of patient doses and image quality in diagnostic radiology. Tartu, 2009.
66. **Jüri Raud.** Study of negative glow and positive column regions of capillary HF discharge. Tartu, 2009.
67. **Sven Lange.** Spectroscopic and phase-stabilisation properties of pure and rare-earth ions activated ZrO_2 and HfO_2. Tartu, 2010.
68. **Aarne Kasikov.** Optical characterization of inhomogeneous thin films. Tartu, 2010.
69. **Heli Valtna-Lukner.** Superluminally propagating localized optical pulses. Tartu, 2010.

70. **Artjom Vargunin.** Stochastic and deterministic features of ordering in the systems with a phase transition. Tartu, 2010.
71. **Hannes Liivat.** Probing new physics in e+e− annihilations into heavy particles via spin orientation effects. Tartu, 2010.
72. **Tanel Mullari.** On the second order relativistic deviation equation and its applications. Tartu, 2010.
73. **Aleksandr Lissovski.** Pulsed high-pressure discharge in argon: spectroscopic diagnostics, modeling and development. Tartu, 2010.
74. **Aile Tamm.** Atomic layer deposition of high-permittivity insulators from cyclopentadienyl-based precursors. Tartu, 2010.
75. **Janek Uin.** Electrical separation for generating standard aerosols in a wide particle size range. Tartu, 2011.
76. **Svetlana Ganina.** Hajusandmetega ülesanded kui üks võimalus füüsikaõppe efektiivsuse tõstmiseks. Tartu, 2011
77. **Joel Kuusk.** Measurement of top-of-canopy spectral reflectance of forests for developing vegetation radiative transfer models. Tartu, 2011.
78. **Raul Rammula**. Atomic layer deposition of HfO_2 – nucleation, growth and structure development of thin films. Tartu, 2011.
79. **Сергей Наконечный.** Исследование электронно-дырочных и интерстициал-вакансионных процессов в монокристаллах MgO и LiF методами термоактивационной спектроскопии. Тарту, 2011.
80. **Niina Voropajeva.** Elementary excitations near the boundary of a strongly correlated crystal. Tartu, 2011.
81. **Martin Timusk.** Development and characterization of hybrid electro-optical materials. Tartu, 2012, 106 p.
82. **Merle Lust.** Assessment of dose components to Estonian population. Tartu, 2012, 84 p.
83. **Karl Kruusamäe.** Deformation-dependent electrode impedance of ionic electromechanically active polymers. Tartu, 2012, 128 p.
84. **Liis Rebane.** Measurement of the $W \to \tau\nu$ cross section and a search for a doubly charged Higgs boson decaying to τ-leptons with the CMS detector. Tartu, 2012, 156 p.
85. **Jevgeni Šablonin.** Processes of structural defect creation in pure and doped MgO and NaCl single crystals under condition of low or super high density of electronic excitations. Tartu, 2013, 145 p.
86. **Riho Vendt**. Combined method for establishment and dissemination of the international temperature scale. Tartu, 2013, 108 p.
87. **Peeter Piksarv.** Spatiotemporal characterization of diffractive and non-diffractive light pulses. Tartu, 2013, 156 p.
88. **Anna Šugai.** Creation of structural defects under superhigh-dense irradiation of wide-gap metal oxides. Tartu, 2013, 108 p.
89. **Ivar Kuusik.** Soft X-ray spectroscopy of insulators. Tartu, 2013, 113 p.
90. **Viktor Vabson**. Measurement uncertainty in Estonian Standard Laboratory for Mass. Tartu, 2013, 134 p.

91. **Kaupo Voormansik.** X-band synthetic aperture radar applications for environmental monitoring. Tartu, 2014, 117 p.
92. **Deivid Pugal.** hp-FEM model of IPMC deformation. Tartu, 2014, 143 p.
93. **Siim Pikker.** Modification in the emission and spectral shape of photostable fluorophores by nanometallic structures. Tartu, 2014, 98 p.
94. **Mihkel Pajusalu**. Localized Photosynthetic Excitons. Tartu, 2014, 183 p.
95. **Taavi Vaikjärv.** Consideration of non-adiabaticity of the Pseudo-Jahn-Teller effect: contribution of phonons. Tartu, 2014, 129 p.
96. **Martin Vilbaste.** Uncertainty sources and analysis methods in realizing SI units of air humidity in Estonia. Tartu, 2014, 111 p.
97. **Mihkel Rähn.** Experimental nanophotonics: single-photon sources- and nanofiber-related studies. Tartu, 2015, 107 p.
98. **Raul Laasner.** Excited state dynamics under high excitation densities in tungstates. Tartu, 2015, 125 p.
99. **Andris Slavinskis.** EST Cube-1 attitude determination. Tartu, 2015, 104 p.
100. **Karlis Zalite**. Radar Remote Sensing for Monitoring Forest Floods and Agricultural Grasslands. Tartu, 2016, 124 p.
101. **Kaarel Piip.** Development of LIBS for *in-situ* study of ITER relevant materials. Tartu, 2016, 93 p.
102. **Kadri Isakar.** ^{210}Pb in Estonian air: long term study of activity concentrations and origin of radioactive lead. Tartu, 2016, 107 p.
103. **Artur Tamm.** High entropy alloys: study of structural properties and irradiation response. Tartu, 2016, 115 p.
104. **Rasmus Talviste.** Atmospheric-pressure He plasma jet: effect of dielectric tube diameter. Tartu, 2016, 107 p.
105. **Andres Tiko.** Measurement of single top quark properties with the CMS detector. Tartu, 2016, 161 p.
106. **Aire Olesk.** Hemiboreal Forest Mapping with Interferometric Synthetic Aperture Radar. Tartu, 2016, 121 p.
107. **Fred Valk.** Nitrogen emission spectrum as a measure of electric field strength in low-temperature gas discharges. Tartu, 2016, 149 p.
108. **Manoop Chenchiliyan.** Nano-structural Constraints for the Picosecond Excitation Energy Migration and Trapping in Photosynthetic Membranes of Bacteria. Tartu, 2016, 115p.
109. **Lauri Kaldamäe.** Fermion mass and spin polarisation effects in top quark pair production and the decay of the higgs boson. Tartu, 2017, 104 p.
110. **Marek Oja.** Investigation of nano-size α- and transition alumina by means of VUV and cathodoluminescence spectroscopy. Tartu, 2017, 89 p.
111. **Viktoriia Levushkina.** Energy transfer processes in the solid solutions of complex oxides. Tartu, 2017, 101 p.
112. **Mikk Antsov.** Tribomechanical properties of individual 1D nanostructures: experimental measurements supported by finite element method simulations. Tartu, 2017, 101 p.
113. **Hardi Veermäe.** Dark matter with long range vector-mediated interactions. Tartu, 2017, 137 p.

114. **Aris Auzans.** Development of computational model for nuclear energy systems analysis: natural resources optimisation and radiological impact minimization. Tartu, 2018, 138 p.
115. **Aleksandr Gurev**. Coherent fluctuating nephelometry application in laboratory practice. Tartu, 2018, 150 p.
116. **Ardi Loot**. Enhanced spontaneous parametric downconversion in plasmonic and dielectric structures. Tartu, 2018, 164 p.
117. **Andreas Valdmann.** Generation and characterization of accelerating light pulses. Tartu, 2019, 85 p.
118. **Mikk Vahtrus.** Structure-dependent mechanical properties of individual one-dimensional metal-oxide nanostructures. Tartu, 2019, 110 p.
119. **Ott Vilson.** Transformation properties and invariants in scalar-tensor theories of gravity. Tartu, 2019, 183 p.
120. **Indrek Sünter.** Design and characterisation of subsystems and software for ESTCube-1 nanosatellite. Tartu, 2019, 195 p.
121. **Marko Eltermann**. Analysis of samarium doped TiO_2 optical and multiresponse oxygen sensing capabilities. Tartu, 2019, 113 p.
122. **Kalev Erme**. The effect of catalysts in plasma oxidation of nitrogen oxides. Tartu, 2019, 114 p.
123. **Sergey Koshkarev.** A phenomenological feasibility study of the possible impact of the intrinsic heavy quark (charm) mechanism on the production of doubly heavy mesons and baryons. Tartu, 2020, 134 p.
124. **Kristi Uudeberg.** Optical Water Type Guided Approach to Estimate Water Quality in Inland and Coastal Waters. Tartu, 2020, 222 p.
125. **Daniel Blixt.** Hamiltonian analysis of covariant teleparallel theories of gravity. Tartu, 2021, 142 p.
126. **Ulbossyn Ualikhanova.** Gravity theories based on torsion: theoretical and observational constraints. Tartu, 2021, 154 p.
127. **Iaroslav Iakubivskyi**. Nanospacecraft for Technology Demonstration and Science Missions. Tartu, 2021, 177 p.
128. **Heido Trofimov.** Polluted clouds at air pollution hot spots help to better understand anthropogenic impacts on Earth’s climate. Tartu, 2022, 96 p.
129. **Ott Rebane.** *In situ* non-contact sensing of microbiological contamination by fluorescence spectroscopy. Tartu, 2022, 157 p.
130. **Juhan Saaring.** Ultrafast Relaxation Processes in Ternary Hexafluorides Studied under Synchrotron Radiation Excitation. Tartu, 2022, 106 p.
131. **Ahmet Ilker Topuz.** Quantitative and qualitative investigations for muon scattering tomography via GEANT4 simulations: A computational study. Tartu, 2023, 163 p.